INTERNATIONAL JOURNAL OF
IJCOE
COASTAL, OFFSHORE & ENVIRONMENTAL ENGINEERING

Volume 7 | Issue 3 | Aug 2022

www.ijcoe.org

International Journal of Coastal, Offshore and Environmental Engineering (IJCOE)

Vol. 7, Issue. 3, Aug 2022

Since 2015

International Journal of Coastal, Offshore & Environmental Engineering

ISSN: 2980-8731 (online)

IJCOE
Editor-in-Chief: Prof. Hamid S.Bahai

International Journal of Coastal, Offshore & Environmental Engineering
Since 2015
ISSN: 2980-8721 (online)

In The Name of God

Message from the Editor-in-Chief

The IJCOE journal office was established in 2015,and its first issue was published in 2016. TheIJCOE covers a wide range of research in thefields of oceanography & ocean technology, aswell as marine industries & marine engineering.The editorial board of IJCOE consists of nearly130 of the greatest scientists and researchersfrom over 30 countries worldwide, and thejournal's review board comprises 1,000 membersfrom all five continents. The membership andapplication process for joining the editorial andreview boards of this journal is ongoing. IJCOE isa research-academic quarterly journal that haspublication and distribution permissions fromthe Press Organization and permission topublish scientific-research articles from theMinistry of Science, Research, and Technology(MSRT) with an "A" rating. It also holds a "Q1"rating from the ISC institute with an impactfactor (IF) of approximately 0.43 and isconsidered a "core journal" (prestigious andoutstanding journal). IJCOE is an open-accessjournal and allows the download and receipt ofaccepted articles in full text for free. It respectsand adheres to copyright and COPE regulations.The journal's office operates 24/7, providingservices to researchers. In addition to publishinga regular quarterly journal, IJCOE has 16 specialissues on specific topics in preparation. It alsoprovides conditions for publishing specializedbooks, references, and handbooks. Moreover, itis ready to cooperate with the secretariats ofreputable international conferences to publishtheir selected and outstanding articles. IJCOEevaluates, appraises, and publishes books,articles, and the scientific achievements andfindings of esteemed researchers and scientistsworldwide who are innovating and conductingin-depth research in the "important and strategicfield of the maritime technology & Oceanengineering." It welcomes any form of jointcooperation with universities, research institutes,and related research centers at the national,regional, and international levels, and extends ahand for collaboration.

Classification of Editorial Board in IJCOE

Editor-in-Chief

Director-in-Chief

Deputy Editor

Executive Managers

English Text Editor

Technical Editor

International Editorial Board

National Editorial Board

Editorial Board Associate

Editorial Board Assistant

Guest Editorial Board

Advisory Board

Administrative Coordinator

Honorary Board Member

Methodology Advisor

Author Benefits

- Open Access
- Rapid Publication
- Thorough Peer-Review
- No Copyright Constraints
- Coverage by Leading Indexing Services
- Discounts On Article Processing Charges (APC)
- No Space Constraints, No restriction on the maximum length of the papers, number of figures or colors

INTERNATIONAL JOURNAL OF IJCOE COASTAL, OFFSHORE & ENVIRONMENTAL ENGINEERING

Aims of IJCOE

Hydrodynamics

Marine equipment

Structural mechanics

Ocean environmental predictions

Stochastic calculations Experimental

Automatic Control of Marine Systems

Scope of IJCOE

Marine Hazards

Ocean Acoustics

Naval Architecture

Ocean Engineering

Coastal Engineering

Marine Meteorology

Marine Earth Sciences

Underwater Technology

Marine Renewable Energy

Polar & Arctic Engineering

Marine Renewable Energy

Marine Geography & Geodesy

Marine Environmental Engineering

Automatic Control of Marine Systems

Hydro Physics & Physical Oceanography

Type of papers

- Case Studies
- Book Reviews
- Review Article
- Letters to the Editor
- Methodology Papers
- Editorials and Commentaries
- Response or Rejoinder Papers
- Perspective or Opinion Papers
- Conceptual or Theoretical Papers
- Meta-Analysis and Systematic Reviews
- Short Communications or Brief Reports
- Research Articles (Original Research Papers)

Scientific Research Journal

Ministry of Science, Research And Technology (MSRT)

Jurnal Ranking 2023: A

Ministry Of Science, Research And Technology (ISC)

Citation Impact 2022: 0.429

Quartile 2022 : Q1

Core Collection

IJCOE is a Member of

Cantact Us

Office 1 | Research Institute of Meteorology and Atmospheric Science

Address | Tehran, Shahid Kharrazi Highway, Pajoohesh Blvd, Research Institute of Meteorology and Atmospheric Science, Sand and Dust Storm International Research Center (SDS-IRC), No. 13, 1st floor.

Phone | +982144787652

Postal code | 13611-14977

website | www.rimac.ac.ir

Office 2 | Iranian National Institute for Oceanography and Atmospheric Science

Address | Tehran, Dr. Fatemi Gharbi St., Shahid Etemadzade St., No. 3, third floor.

Phone | +982166944873

Postal code | 13389 – 14118

website | www.inio.ac.ir

Email | Info@ijcoe.org

Website | www.ijcoe.org

Follow Us

www.ijcoe.org

INTERNATIONAL JOURNAL OF IJCOE COASTAL, OFFSHORE & ENVIRONMENTAL ENGINEERING

Volume & Issue:

Volume 7, Issue 3, August 2022

Number of Articles: 6

Content

INTERNATIONAL JOURNAL OF
OFFSHORE & ENVIRONMENTAL ENGINEERING IJCOE Vol.7/No. 3/Summer 2022 (1-9)

Available online at: www. Ijcoe.org

The study of chlorophyll concentration behavior over southern coasts of Iran with an emphasis on the cold season of the year

Saviz Sehat Kashani[1*], Mehdi Rahnama[2], Noushin Khoddam[3], Sara Attarchi[4]

[1] Atmospheric Science and Meteorological Research Center (ASMERC), Tehran, Iran; s-sahat@irimo.ir*
[2]Atmospheric Science and Meteorological Research Center (ASMERC), Tehran, Iran; m-rahnama@irimo.ir
[3]Atmospheric Science and Meteorological Research Center (ASMERC), Tehran, Iran; nushin_khoddam@alumni.ut.ac.ir
[4]Department of Remote Sensing and GIS, Faculty of Geography, University of Tehran, Tehran, Iran; satarchi@ut.ac.ir

ARTICLE INFO

Article History:
Received: 23 Jul. 2022
Accepted: 27 Aug. 2022

Keywords:
Chlorophyll
SST
AOD
Persian Gulf
Oman Sea
Sand and Dust

ABSTRACT

The concentration of chlorophyll in marine environments indicates the quantity of photosynthetic plankton (phytoplankton), found in marine ecosystems. Phytoplankton populations are affected by weather conditions such as Sea Surface Temperature and Winds. They are also influenced by Aerosol Optical Depth(AOD), which can show the existence of dust. Moreover, there are seasonal variations and the correlation between these factors varies according to the depths. Despite the decrease in temperature and an increase in pressure on land areas during winter, which is accompanied by a decrease in strong winds, the formation of atmospheric fronts and strong winds caused the transfer of dust from susceptible springs in Saudi Arabia and the UAE and dust was transferred to it from the southern coast of the Persian Gulf. Investigating the long-term relationship between SST changes and the AOD with chlorophyll concentration on the Persian Gulf coasts as well as the Oman Sea, using daily MODIS products in the period of 2003 to 2020 demonstrates a strong correlation in coastal areas with the lowest depth. trend of SST and AOD on the both Seas is similar, along with the lowest values during the winter, while the seasonal trend show, the highest values of chlorophyll concentrations, in winter. Besides examining long-term chlorophyll concentration behavior over the Sea of Oman and the Persian Gulf, an emphasis was applied to the cold season of the year on February 17-22, 2018 for understanding the relationships between chlorophyll, AOD, and SST, showing the possibility of time delay in the correlation between sea surface temperature and optical depth of aerosols with chlorophyll concentration.

1. Introduction

The concentration of chlorophyll in marine ecosystems is an indication of the quantity of plankton in those ecosystems and affects its dynamics. Chlorophyll concentrations are not constant and are affected by seasonal variations, precipitation, water flow, and water surface temperature [1]. Numerous studies have been conducted in this area and the extent of these effects has been demonstrated to vary across ecosystems [1-4]. Chlorophyll concentration can also be affected by changes in salinity that occur due to the evaporation of seawater[5].An increase in wind speed over the Persian Gulf increases the rate of evaporation, which can cause changes in the salinity and hence the concentration of chlorophyll [6]. Aerosols in the atmosphere are a rich source of nutrients that increase the production of marine environments and their carbon sequence, which affects the concentration of carbon dioxide and ultimately the climate [2]. Paytan et al. 2009 demonstrated that the growth response of phytoplankton to aerosols varies according to the specific composition of aerosols and the phytoplankton species [2]. Aerosols contain a variety of natural and synthetic compounds, including mineral dust, sea salt crystals, bacteria, and other microscopic particles. Aerosols add nitrogen and phosphorous compounds to water; however, not all aerosols enhance phytoplankton growth [2]. In another study, Galissai et al. (2014) investigated the possibility of dust storms affecting the growth of phytoplankton in the

Mediterranean Sea [1]. This study was important because the surface of the Mediterranean Sea lacks essentially the nutrients necessary for the growth of plankton, but its proximity to the world's largest and most active desert has led to the influx of minerals. This study revealed that the advent of aerosol accounts for around one to ten percent (on average 5%) of chlorophyll variability in the Mediterranean [1]. This highlights the importance of investigating the impact of dust events on chlorophyll concentrations in marine environments. In order to monitor phytoplankton on synoptic scales, remote sensing is the available technique that can provide data on chlorophyll-a (chl-a) as an indicator of phytoplankton abundance [7]. Globally, West Asia is widely recognized as one of the most affected parts by airborne dust. Taking a closer look, we can designate Khuzestan as one of the dust hotspots. Khuzestan is an Iranian province located in the southwest of the country, bordering Iraq and the Persian Gulf. Dust storms have become a major environmental concern in this oil- and gas-rich province during the last decades [8]. Zarasvandi et al. (2011) estimated a mean dust storm frequency of 47 days per year, rising at a rate of two days per year [8]. They also pointed out that the major dust sources affecting Khuzestan are dry lakebeds, alluvial deposits, and deserts in neighboring countries to the west. In particular, the Mesopotamian marshes are suffering rapid land degradation, caused by natural and human-induced factors, and might vanish soon in the future, thus expanding the source area [9]. On the other hand, local dust sources are also important. They are associated with a desert climate and poor, often salty, river flows that leave bare soils exposed to erosion. 9 percent of Khuzestan plain, equivalent to 349254 hectares, are dust-generating sources [10]. Based on land use type and area, the identified zones include destroyed range, rainfed agriculture lands, bare lands, wetlands, dried ponds, and irrigated agriculture lands, respectively.

An episode that occurred in February 2018 is described to illustrate the severity of dust storms in the Khuzestan Province of Iran. On the morning of Sunday, February 18, 2018, frontal-type dust was activated in Kuwait and Iraq, affecting the Khuzestan province of Iran.

The concentration of dust in Abadan and Khorramshahr was about 66 times beyond the permitted limit, and the horizontal visibility in these cities decreased to about 100 meters, which resulted in the cancellation of 2 flights of the Abadan International Airport on February 18, 2018. The schools of the Mahshahr, Shadegan, Abadan, and Khorramshahr cities were closed down due to the occurrence of dust phenomena in the afternoon. on addition, the storm at a speed of 50 km/h on the Sunday morning (February 18, 2018), caused local rising dust in some parts of the province, including Ahvaz, Abadan, Omidieh, and Izeh, while horizontal visibility in Ahwaz reduced to 500 m (Islamic Republic News Agency). On Feb.19th, 2018, the recorded dust concentrations of this dust event reported by more than 983 ug/m3, leading to the closing of all schools of 11 cities of Khuzestan (ISNA News Agency).

In this study, dust storm event analysis in Khuzestan province along with the long-term average chlorophyll concentration between 2003 and 2020 in the Oman Sea and the Persian Gulf has been investigated. Also, the relationship between chlorophyll concentration, Sea Surface Temperature (SST), and Aerosol Optical Depth (AOD) has been studied. Where after, examining a sand and dust event on February 19, 2018, the behavior of chlorophyll by changing SST and AOD is investigated. The most important innovation of the research is to consider the time delay in the correlation between chlorophyll concentration with SST and AOD in the long term. The relationship between this correlation and water depth in different parts of the Oman Sea as well as the Persian Gulf has also been interpreted. Additionally, the study of the effect of a large dust event in the region on changes in chlorophyll concentration, SST, and AOD at the time of occurrence and the following days is another innovation of this study.

2. Data and methodology

The data studied in this research were extracted from the GIOVANNI site. The daily average data (8 days) including Sea Surface Temperature (SST), Aerosol Optical Depth (AOD), and chlorophyll concentration from the MODIS instrument on board of AQUA satellite for the period of 2003-2020 has been extracted. Moreover, the MODIS instrument images from the Worldview site, daily images of chlorophyll concentration, AOD, and SST for the period February 17 to February 22 have been obtained.

First of all, by considering the long-term average of the target quantities over the period of 2003 to 2020, trend in long-time changes as well as the correlation patterns between these quantities was analyzed. Afterward, by investigating a sand and dust event on February 19, 2018, the behavior of chlorophyll by changing SST and AOD is investigated.

3. Area of Study

In this paper, the water bodies of the Persian Gulf, the Sea of Oman, and Khuzestan province were studied and presented in Figure 1.

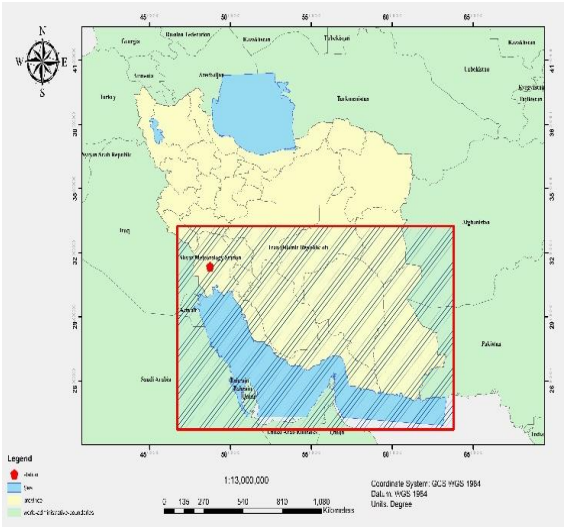

Figure 1. Study area

4. Results and Discussion

4.1. Climatic analysis of the study area

Figure 2 shows the long-term average pattern of meteorological quantities near the ground, including average sea level pressure, 2-meter altitude temperature, sea surface temperature, and wind in the period 2003-2020 is presented separately for the study area. In the spring, low-pressure thermal centers gradually form in the southeastern regions of Iran and the high-pressure center in the highlands of Afghanistan, which corresponds to the maximum and minimum temperature centers in these areas. The low heat pressure tongues are drawn to the central regions of Iran, which are accompanied by ridges in the Zagros highlands. Therefore, pressure gradients are created in the west of Afghanistan and cause north winds in these areas. In the northern and western parts of the Persian Gulf, no significant compressive changes are observed in spring and relatively calm winds prevail. In addition, the sea surface temperature is lower than in its southern and eastern regions. The surface water temperature in the Oman Sea is higher than in the Persian Gulf. Southwest and west winds are forming on the Oman Sea at the beginning of the monsoon season. In summer, with increasing temperature, low-pressure thermal centers are formed in ’s southern and southeastern regions. Simultaneously with that, the high-pressure center on the mountains of Afghanistan is strengthened and with the strengthening of pressure gradients in the border area of Iran and Afghanistan, strong north winds prevail, which, by activating dust springs in these areas, transfer significant amounts of dust to the south. The heat low-pressure tongues extend from the south of Iran to the southwest and west of Iran and enter Iraq, forming relatively strong gradient pressure patterns. As a result, the northwest winds are strengthened and, in these areas, it also strengthens the dust springs, which results in the transfer of dust to the Persian Gulf, especially in its northern and western parts. The Sea Surface Temperature (SST) in the Persian Gulf is higher than in the Oman Sea due to the faster response of water temperature in shallow areas than in deeper areas, which is due to the specific heat capacity of water. Strong southwesterly winds due to the Indian monsoon prevail in the Oman Sea. In autumn, with the decrease in temperature, the average values of sea-level increase in most areas, which weakens the gradient pressure patterns and, consequently, weakens the strong winds. Also, with the monsoon retreat of India, the currents prevailing in the Oman Sea are weakened and the western orbital winds prevail in this region. The formation of atmospheric fronts can be accompanied by strong winds and cause the transfer of dust from susceptible springs in Saudi Arabia and the UAE and the dust is transferred from the southern shores of the Persian Gulf to it. SST in this season in the northern and western parts of the Persian Gulf has decreased more than in other marine areas, which as mentioned is due to the shallower depth of the Persian Gulf than the Oman Sea, due to the heat capacity of water, it has a faster response to lower air temperature than deeper areas.

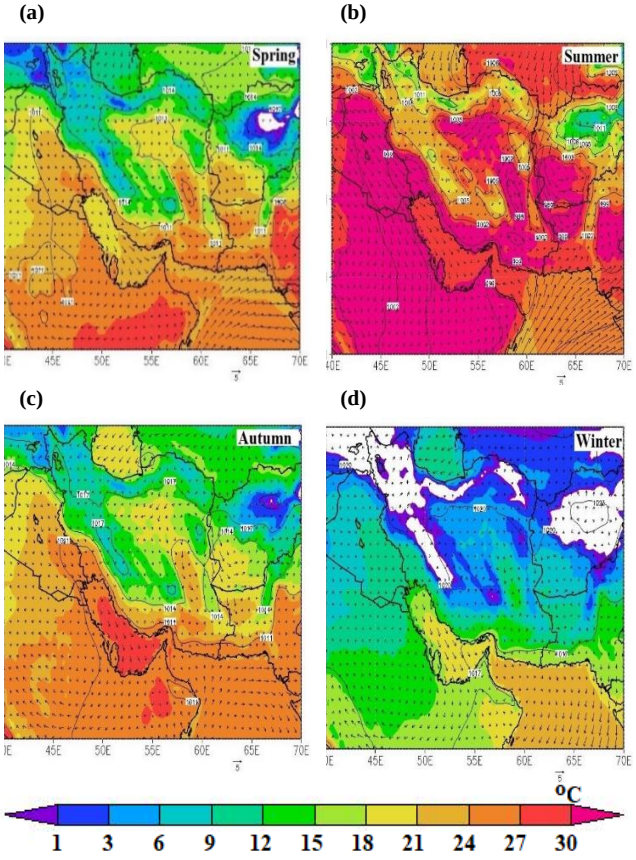

Figure 2. Long-term average pattern of mean sea level pressure (colored contours),2m Temperature and sea surface temperature (shaded regions), and wind at 10m height during a) Spring, b) Summer, c) Autumn and d) Winter (2003-2020)

Figure 3 presents the seasonal model of the long-term average of meteorological quantities including geopotential height, temperature, and wind speed for the period 2003-2020 in the study area and at a pressure level of 850 hPa. As can be seen, in the spring in the southwestern regions of Afghanistan, a low-lying

center was established, which is accompanied by the penetration of a ridge from the northeast of Iran on the border between Iran and Afghanistan. This causes a gradient pressure pattern and the formation of north winds in these areas and strengthens the earth's surface patterns. In addition, low-geopotential height centers are observed in the southern regions of Iran due to higher temperatures, while in the higher and colder regions, high-geopotential height centers are located. In summer, with the rise in temperature on land resulting from the movement of the tropical convergence belt, the formation of low-lying centers in the southern half of Iran, western Afghanistan, and the Saudi desert is observable. Also, a geopotential trough has been stretched to the southwest and west of Iran. These patterns enhance the gradient pressure patterns and thus increase the intensity of the winds, which is in harmony with the earth's surface and can activate the dust sources and facilitate the process of emission and transfer of dust. With the beginning of the decreasing trend of temperature in autumn, low-geopotential height centers have weakened, which results in the weakening of gradient pressure and strong winds. This pattern continues in winter and with the cold weather from the northern latitudes and the relatively calm atmosphere (on average) in most areas, emissions and dust transfer also decrease.

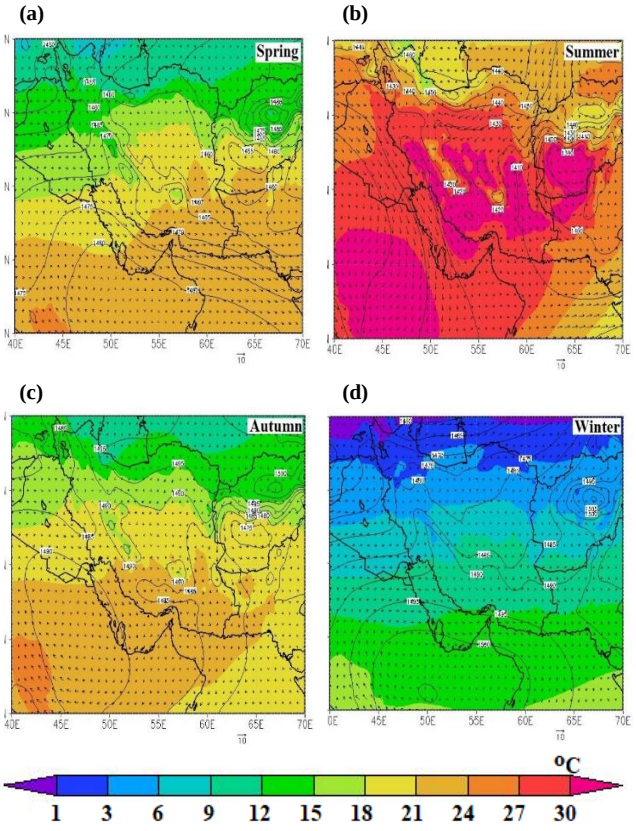

Figure 3. Long-term average pattern of geopotential height (black contours), temperature (shaded regions,) and wind at 850 hPa during a) Spring, b) Summer, c) Autumn and d) Winter (2003-2020).

4.2. Khuzestan province dust event analysis

Figure 4 shows the true color of the Terra satellite and dust RGB of the MSG on February 19, 2018. Because of the cloudiness in the western and northwestern regions of Iran as well as the center of Iraq since this dust event is considered a frontal dust formation type, the extent of the dust mass is not well recognizable, while significant dust concentration in Khuzestan province is observable.

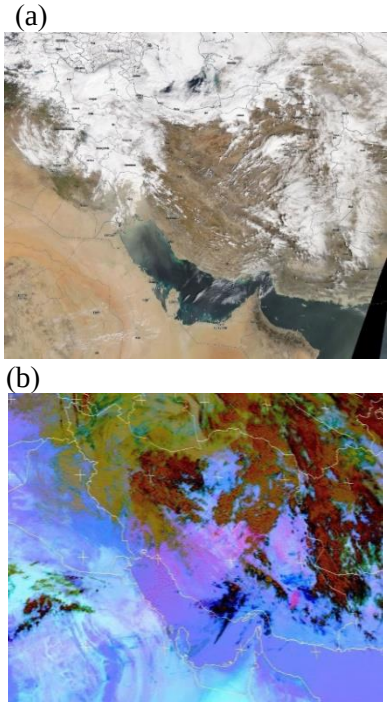

Figure 4. a) The true color of the Terra satellite and b) the dust RGB of the MSG on February 19, 2018.

The Aerosol Optical Depth (AOD) product of the MODIS generated by the combination of dark target and deep blue algorithms is shown in Figure 5. Due to the cloud masses in large parts of the region, AOD is not composed homogenously, but the maximum AOD is seen in Kuwait, northeastern Saudi Arabia, the Persian Gulf, and Khuzestan province in southwestern Iran.

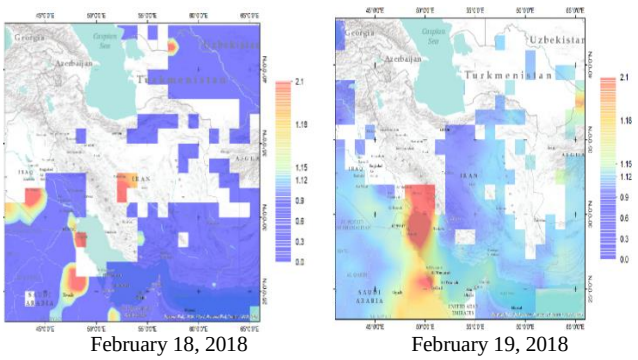

Figure 5. The aerosol optical depth (AOD) product of the MODIS that generated by the combination of dark target and deep blue algorithms for February 18-19, 2018.

The horizontal visibility values of the Meteorological Aerodrome Report (METARs) of Ahwaz city were shown in Figure 6. Horizontal visibility decreased around 09 UTC on February 18 but constantly increased until the first hours of February 19th. Afterward horizontal visibility was reduced to reach its lowest level on February 19th, 2018. Again, mid-February 20th, the horizontal visibility shows gradual improvement.

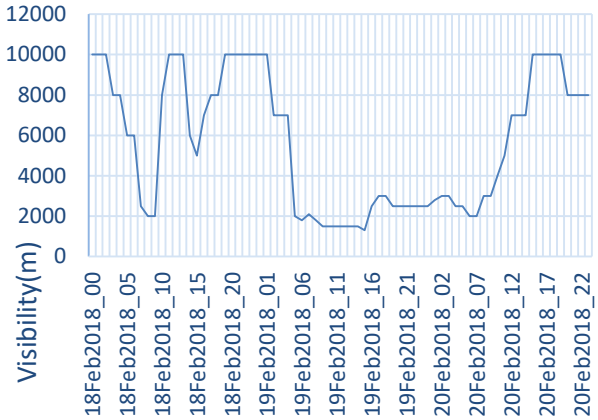

Figure 6. The horizontal visibility values of the METeorological Aerodrome Report (METARs) of Ahwaz city for February 18-19, 2018.

To better evaluate the output of the model, the values of the PM10 concentration output of the model are shown in Figure 7 with the PM10 concentration data of the air pollution monitoring station in Ahvaz. The maximum observed PM10 concentration is 983 ug/m3 on 17 UTC of the 19th. Feb.2018. The comparison demonstrates that the model overestimated the amounts of PM concentration from 12-24 UTC on the day Feb.18th. and 20th.

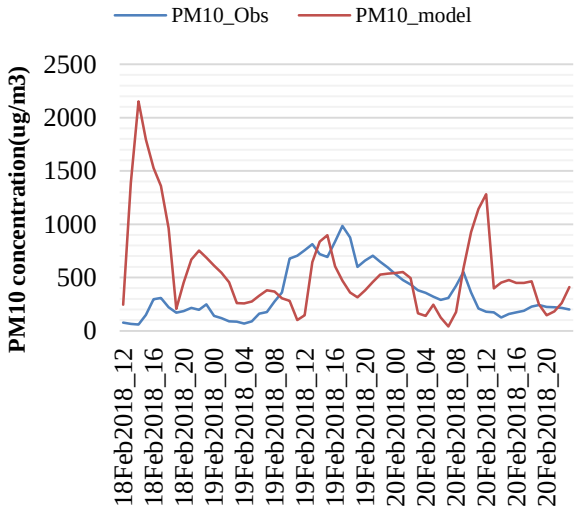

Figure 7. The values of PM10 concentration output of the model and the PM10 concentration data of the air pollution monitoring station in Ahwaz for February 18-20, 2018

4.3. Examining the trend of the long-term average

In this section, the trend of long-term monthly and seasonal changes in SST, AOD, and chlorophyll concentrations for the two regions of the Oman Sea and the Persian Gulf have been studied simultaneously. The graph of the average seasonal changes of the target quantities for 2003 to 2020 in the Oman Sea is presented in Figure 8. As can be seen, in the Oman Sea region, changes in SST and AOD have a similar trend; While changes in chlorophyll concentration were reversed. The highest values of chlorophyll concentration were measured in winter and the lowest in summer. however, the highest/lowest values of SST and AOD were observed in summer/winter respectively. This study has also been done for the Persian Gulf region, the results of which were presented below (Figure 8). The trend of seasonal changes in SST and AOD is to some extent similar, with the highest SST and AOD values in summer and the lowest in winter. In summer, due to the synoptic patterns, conditions were created for the occurrence of sand and dust events in Iraq and the western half of Iran, and due to the flow of northwesterly winds, significant amounts of sand and dust break in to the Persian Gulf. The trend of changes in chlorophyll concentration was observed in contrast to SST and AOD and its highest/lowest amount occurred in winter/summer respectively

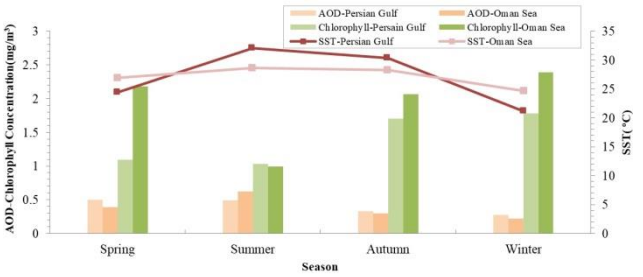

Figure 8. Trend of changes in the long-term average (2003-2020) of the seasonal quantities of AOD, SST, and chlorophyll concentrations in the Oman Sea region .

By examining the trend of monthly changes in the target's quantities in Figure 9, we found that, the highest values of chlorophyll concentration in the Oman Sea occur in March and February, which is associated with the lowest values of SST. while, the lowest values of were found in July, which is in line with the highest SST. The highest value of AOD quantity also occured in July, which coincides with the activity of monsoon flows, which can increase dust events in the southeastern parts of Iran and west of Pakistan and also cause the transfer of sand and dust to the Oman Sea. The pattern of the trend of long-term monthly changes in the quantities in question for the Persian Gulf is also presented in Figure 9. As the figure clearly shows, the highest SST values were obtained in July, August, and September, by more than 30 degrees Celsius. The highest AOD values were also observed

in May and July. during July, due to the formation of western currents from Iraq, dust was directed to the western half of Iran, and this caused AOD values in the Persian Gulf to decrease. The trend of changes in the long-term monthly average of chlorophyll concentration also showed that although the highest values were recorded in the cold months of the year from December to February, the lowest values were found in the warm months of the year from May to July.

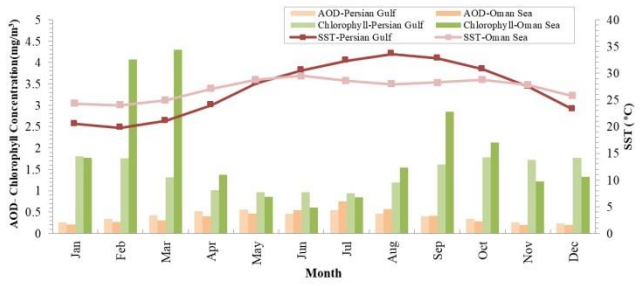

Figure 9. Trend of changes in the long-term average (2003-2003) of the monthly AOD, SST, and chlorophyll concentrations in the Oman Sea region

4.3. Calculating the correlation coefficient between SST, AOD, and chlorophyll concentration

In the continuation of this study, the correlation coefficient between the studied quantities has been calculated. As observed in the previous section, the trend of changes in SST, AOD, and chlorophyll concentration fluctuates seasonally and it seems that changes in temperature and salinity in seawater can affect the change in chlorophyll concentration. The scatter plot and correlation pattern between AOD and chlorophyll concentration as well as SST and chlorophyll concentration for the Northwest, North, and south of Persian Gulf and also Oman Sea is shown separately in Figure 10 (a to h). The correlation is not statistically significant, except in coastal areas where there is a relatively good correlation between the quantities. The highest level of correlation was observed in the southern regions of the Persian Gulf (Fig. 10 e and f), which has less depth than other regions. In this region, chlorophyll concentration increases as the SST increases. Furthermore, according to scatter plots, chlorophyll concentrations increase with AOD rises in all regions.

(a)

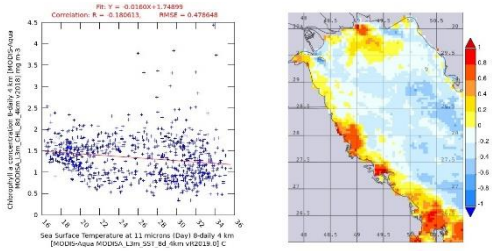

(b)

(c)

(d)

(e)

(f)

(g)

(h)

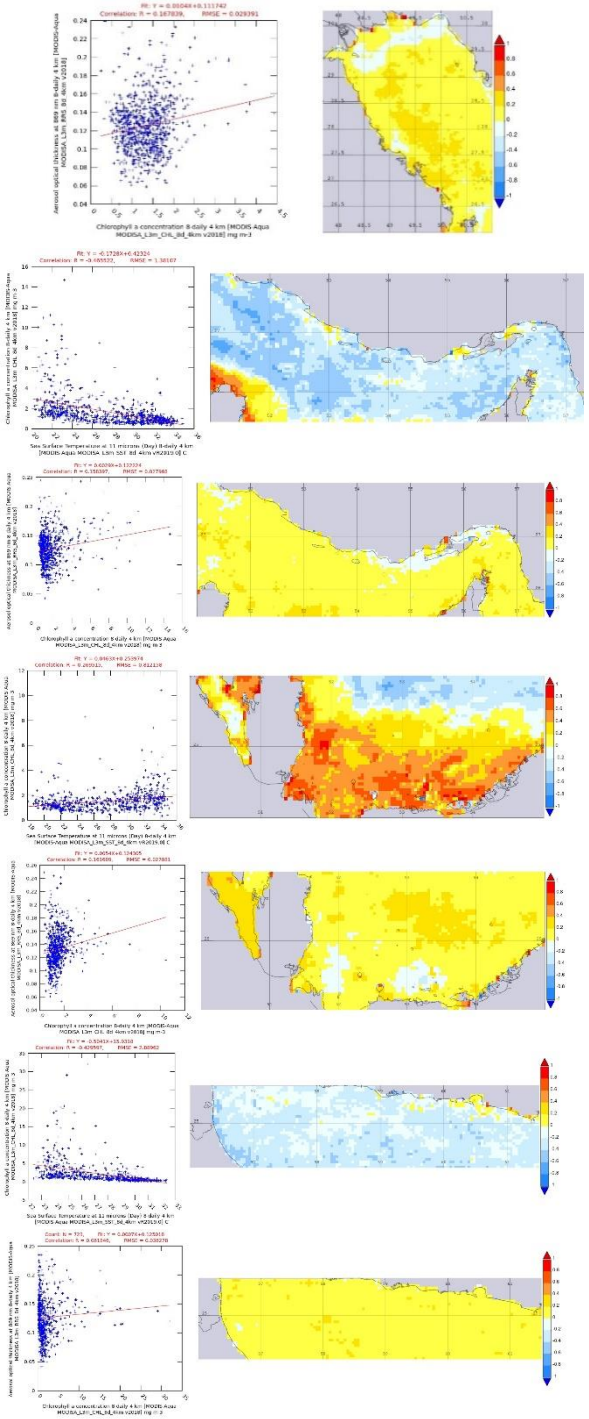

Figure 10. Scatter plot and Correlation pattern between a) chlorophyll concentration and SST and b) chlorophyll concentration and AOD in the study area .

By studying the trend of long-term changes, it seems that there is a possibility of a correlation with a time delay between SST and AOD and chlorophyll concentration. In the continuation of this study, the relationship between chlorophyll concentration and changes in AOD and SST during the occurrence of a dust event is investigated.

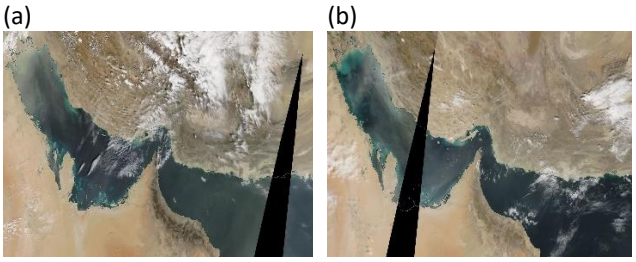

Figure 11. True-color image of MODIS-Terra for February a) 19 and b) 20, 2018.

According to Figure 11, on February 18-20, 2018, there was a severe pressure gradient in the central and southern parts of Iraq due to the the presence of a low system in the west and northwest of Iraq accompanied by the penetration of a ridge from the south and southwest of Iran to the western borders of country. So, the northwesterly strengthen in this area, which causes to activate the dust sources. This weather pattern caused large amounts of dust to be emitted to the southwestern Iran and the Persian Gulf from February 18 to 20.

The study of changes in the pattern of chlorophyll concentration, SST, and AOD, which are presented in Figure 12 to Figure 14, also demonstrates that, with the onset of dust storms, the amount of AOD gradually increased and from February 21, a decreasing trend of AOD in the Persian Gulf was occurred; However, owing to the increase in clouds on this day, the satellite image was not well visible. The pattern of sea surface temperature showed that at the same time with the occurrence of dust, especially on February 19 and 20, the temperature has decreased because of the reduction of radiation entering the water surface due to the presence of dust particles. After that, the temperature gradually increased with the end of the dust event on February 22. Additionally, the pattern of changes in chlorophyll concentration revealed that the chlorophyll concentration increased from February 18 and reached its maximum on February 19, then decreased after the end of the dust event.

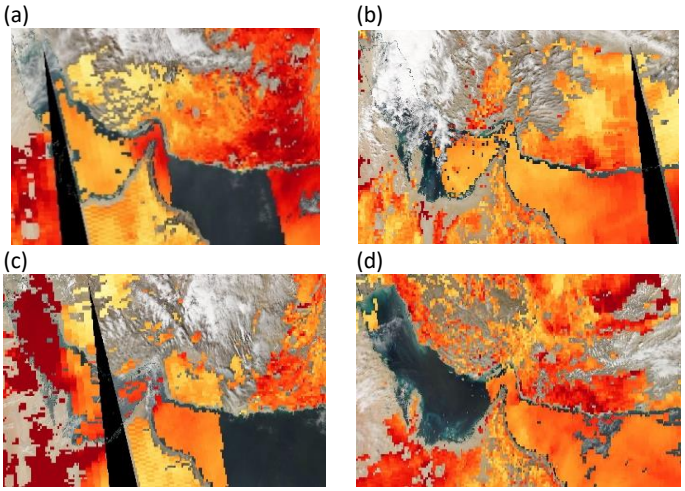

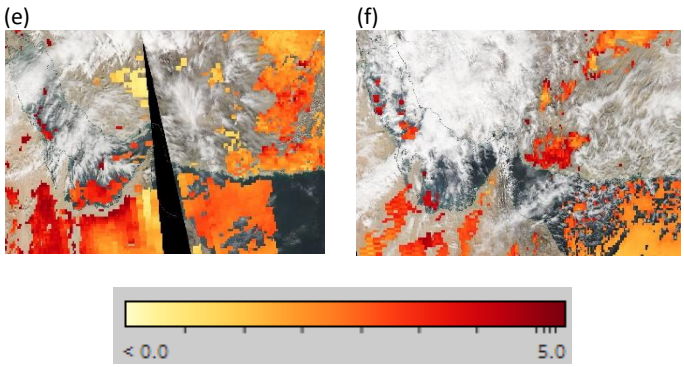

Figure 12. AOD change pattern of Aqua satellite MODIS instrument product (product of DB and DT algorithm) for February a)17, b) 18, c) 19, d) 20, e)21 and f) 22, 2018 at 00:00 UTC .

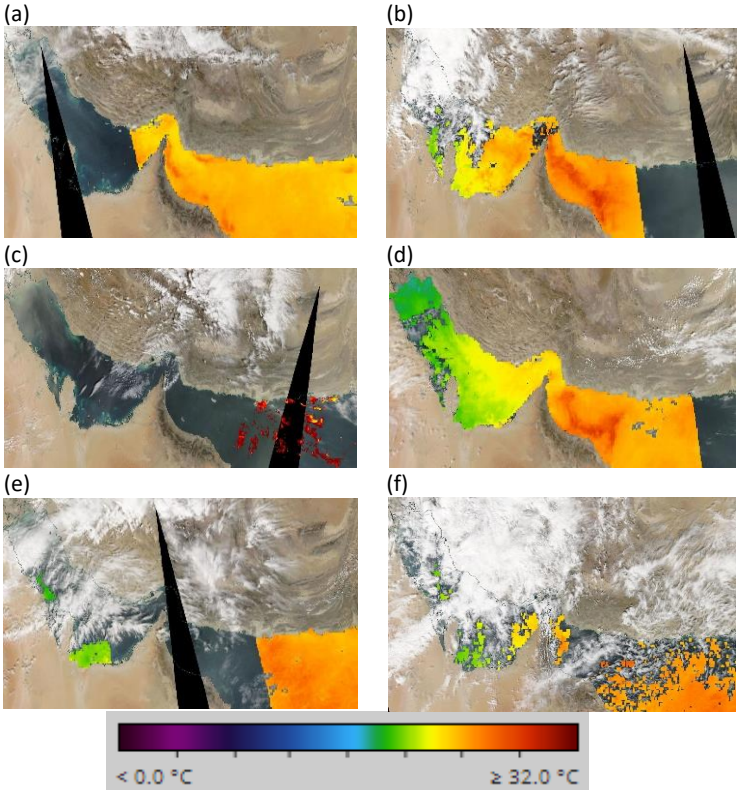

Figure 13. SST change pattern of Aqua satellite MODIS instrument product for February a)17, b) 18, c) 19, d) 20, e)21 and f) 22, 2018 at 00:00 UTC.

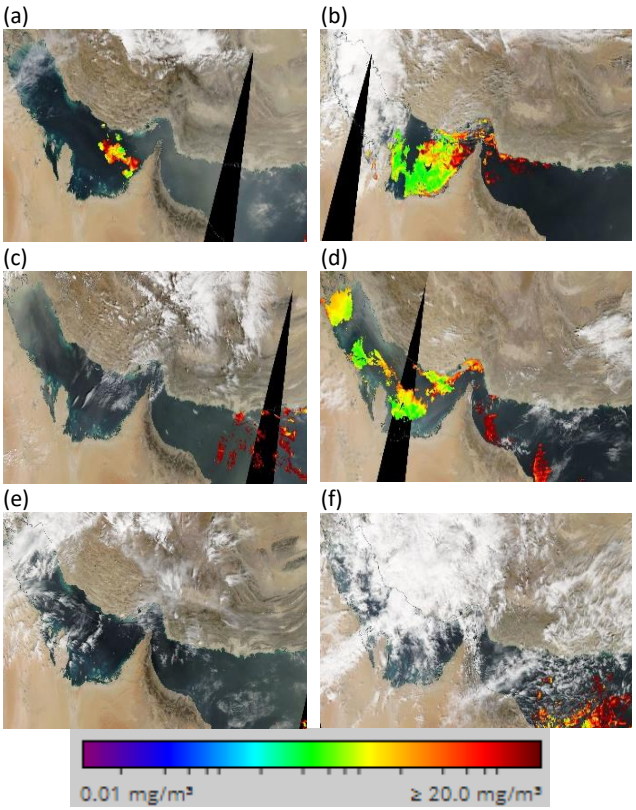

Figure 14. Chlorophyll concentration of the Aqua satellite MODIS instrument product for February a)17, b) 18, c) 19, d)20, e)21, and f) 22, 2018 at 00:00 UTC

5. Conclusions

In this study, the long-term average chlorophyll concentration and its relationship with changes in sea surface temperature and optical depth of aerosols, along with their spatial distribution over the Oman Sea and the Persian Gulf using daily average data (8 days) including SST, AOD, and chlorophyll concentration from MODIS instrument on board of the AQUA satellite were investigated monthly from 2003 to 2020. The results indicated that the seasonal changes in SST and AOD are somewhat similar; the highest/lowest SST and AOD values were found in summer/winter respectively. In summer, due to the synoptic patterns, conditions were created for the occurrence of dust events in Iraq and the western half of Iran, and due to the flow of northwesterly winds, significant amounts of dust enter the Persian Gulf. The trend of changes in chlorophyll concentration is observed in contrast to SST and AOD, and its highest amount occurred in winter and its lowest in summer. In the Oman Sea region, changes in sea surface temperature and optical depth of aerosols have a similar trend; While changes in chlorophyll concentration are reversed. The highest values of chlorophyll concentration were measured in winter and the lowest in summer. however, the highest values of SST and AOD were observed in summer, the lowest were found in winter. Meanwhile, the lowest values of chlorophyll concentration were seen in July, which was in line with the highest SST. The highest quantity of AOD also occurred in July, which coincides with the activity of monsoon flows, which can increase sand and dust events in the southeastern regions of Iran and west of Pakistan and cause the transfer of sand and dust to the Oman Sea.

The trend of changes in SST, AOD, and chlorophyll concentration fluctuates seasonally and it seems that changes in temperature and salinity in seawater can affect the change in chlorophyll concentration. The correlation between AOD and chlorophyll concentration as well as SST and chlorophyll concentration for the Persian Gulf and the Sea of Oman was statistically relatively good in the coastal areas between the quantities. The highest level of correlation was observed in the southern regions of the Persian Gulf, which has less depth than other regions. By studying the trend of long-term changes, it seems that there is a possibility of a correlation with a time delay between SST and AOD and chlorophyll concentration, which is well shown in the case study of dust occurrence in the cold season of the year in February 19, 2018.

6. References

[1] Gallisai, R., Peters, F., Volpe, G., Basart, S. and Baldasano, J.M., (2014), Saharan dust deposition may affect phytoplankton growth in the Mediterranean Sea at ecological time scales, PloS one, 9(10).

[2] Paytan, A., Mackey, K.R., Chen, Y., Lima, I.D., Doney, S.C., Mahowald, N., Labiosa, R. and Post, A.F., (2009), Toxicity of atmospheric aerosols on marine phytoplankton, Proceedings of the National Academy of Sciences, 106(12), pp.4601-4605.

[3] Tan, S.C., Shi, G.Y., Shi, J.H., Gao, H.W. and Yao, X., (2011), Correlation of Asian dust with chlorophyll and primary productivity in the coastal seas of China during the period from 1998 to 2008, Journal of Geophysical Research: Biogeosciences, 116(G2).

[4] Deng, Z.Q., Han, Y.X., Bai, H.Z. and Zhao, T.L., (2008), Effect of dust aerosol production in China mainland on marine primary productivity, China Environmental Science, 28, pp.872-876.

[5] Al-Taee, I.A.A., (2018), Salinity effect chlorophyll significantly. Plant Archive, 18(1), 723-726.

[6] Mahpeykar, O., & Khalilabadi, M. R. (2021). Numerical modelling the effect of wind on Water Level and Evaporation Rate in the Persian Gulf. International Journal of Coastal and Offshore Engineering, *6*(1), 47-53.

[7] Moradi, M. (2022). Inter-comparison of single-sensor and merged multi-sensor ocean color chlorophyll-a products in the shallow turbid waters - case study: Persian Gulf. *International Journal of Coastal and Offshore Engineering*, *7*(2), 1-10.

[8] Zarasvandi, A., Carranza, E. J. M., Moore, F., & Rastmanesh, F., (2011), Spatio-temporal occurrences and mineralogical–geochemical

characteristics of airborne dust in Khuzestan Province (southwestern Iran), Journal of geochemical exploration, 111(3), 138-151.

[9] Cao, H., Liu, J., Wang, G., Yang, G., & Luo, L., (2015), Identification of sand and dust storm source areas in Iran, Journal of Arid Land, 7(5), 567-578.

[10] Peyman Heidarian, A. Azhdari1; M. Jodaki, J. Darvishi Khatooni, R. Shahbazi., (2017), Identifying interior sources of dust storms using remote sensing, GIS and geology (case study: Khuzestan province), scientific Quarterly Journal GEOSCIENCES, 6(27), Issue 105, Page 33-46, DOI:10.22071/GSJ.2017.53928

INTERNATIONAL JOURNAL OF
COASTAL, OFFSHORE & ENVIRONMENTAL ENGINEERING IJCOE Vol.7/No. 3/Summer 2022 (10-19)

Available online at: www. Ijcoe.org

A New Look at the Vertical Shear of the Geostrophic Wind Part I: Dense Wind

Mohammad Taghi Zamanian

Member of Iranian Society of Marine Science and Technology (ISMST); zamanianmohammadtaghi@gmail.com

ARTICLE INFO

Article History:
Received: 23 Oct. 2022
Accepted: 16 Jan. 2023

Keywords:
Barotropic medium
Horizontal variation of density
Baroclinic medium
Thermal wind
Dense wind

ABSTRACT

From one point of view; we can divide atmosphere into two mediums. Barotropic medium, that in this medium, density doesn't change in horizontal direction and isobaric surfaces are parallel to each other in vertical direction. This medium can be motionless, but if in this medium, motion would be taken place, geostrophic wind doesn't change with respect to height.
On the other hand, the baroclinic medium has horizontal gradient of density, and causes various horizontal gradient of pressure with respect to height and implies various horizontal velocity at different levels of the atmosphere. Therefore; geostrophic wind varies with respect to height in this medium.
The horizontal gradient of density not only would produce by horizontal gradient of temperature, but also by horizontal gradient of humidity or combination of both. If horizontal gradient of density would be by both horizontal gradient of temperature and horizontal gradient of humidity – as in natural air, not in dry air – in the case; we name vectorial difference of geostrophic wind with respect to height; *dense wind*.
The purpose of this paper is introduction of three versions of dense wind in natural medium of air, not dry air. Basic axis of first version of dense wind is founded by density, second by virtual temperature and third one by thickness of atmospheric layer. Formulae related to each version is derived and every one of them, represents effects of one type of variation of geostrophic wind with respect to height. First version exhibits advection of light or dense air, second represents virtual temperature advection and third one demonstrates advection of thickness in atmospheric layer. Dense wind is powerful tool for consistency of wind field. Therefore, because air is not dry, the variation of the geostrophic wind with respect to height should be describe with better tool, namely *dense wind*.

1. Introduction

Variation of wind with respect to height has been investigated many times and, in this field, observational studies as well as researches have been done since the beginning of the last century. There are various profits for research on variation of the wind with respect to height. In the first place, it is used for detection of advection of light or dense air, and in the second place, it helps to detect of the thunder storm's type. The reason for second profit is related to the fact that second critical factor in determination of the type and the potential of intensity of thunder storm, is variation of wind with respect to height. However, for this matter of fact, some meteorologists focused their studies on planetary boundary layer, whereas others worked on troposphere as whole.

Regarding to first matter; observations of Charnock et al. [1] of trade wind, had been done at Anegada Island ($15^{\circ}N.64^{\circ}W$). This island, idiomatically, is isolated point of the earth that surrounded by ocean. Charnock and his colleagues' observations include 466 double soundings with balloon using theodolite in fifteen separate days during 27 days' observations at boundary layer. The important results in cases of Anegada's studies are as follows:
A: At the first 1350-meter (height) wind has 24 degrees veering;
B: Acceleration terms in comparison with Coriolis, pressure gradient force and friction terms; are ignorable;

C: They realized that observational wind at upwind coast is almost representative of wind over ocean considering perturbing effect of the Island.
Carlstead [2], tried to apply geostrophic wind's vertical profile in numerical model to cloudiness forecasting and determination of rainy area. Following Charnock et al. [1], variation of wind has been researched by Estoque [3] during study of planetary boundary layer at Christmas Island.
Moreover, one result of variation of geostrophic wind with respect to height, entitled *Thermal wind*, investigated widely, in baroclinic medium by Foster and Levy [4]. They studied variation of speed of geostrophic wind with respect to height for the reason of horizontal gradient of temperature and friction. Also, in their work, the ratio of geostrophic wind's speed has been investigated at two special levels.
Sometime, research on variation of wind with respect to height, is a tool for study of Temperature or humidity fluxes. And sometimes; it is an implement for search of momentum transfer. For the reason of the fact that atmospheric system or oceanic system are systems that, all their parameters are related to each other; therefore, investigation of variation of wind with respect to height, is usable for many purposes and applications undoubtedly.
All researchers those have been worked on variation of geostrophic wind with respect to height, had two common ideas. They have been called difference between two geostrophic wind vectors at two pressure levels; the *thermal wind* as the first idea. Also, they have been assumed the atmosphere as dry air, as a second idea.
Especially, this subject with same hypothesizes, has been used in dynamic meteorology's text books, that is to say, in introducing of thermal wind, they assumed atmosphere is dry and derived formulae related to the subject in this case; although this assumption used for simplicity of the work. For instance, the subject is written in Hess's text book [5], Gill's text book [6], Dutton's text book [7], Holton and Hakim's text book [8] and in other dynamic meteorology text books. In addition; thermal wind has an entrée in *Glossary of Meteorology* [9] with same descriptions.
The purpose of this paper is introducing of three versions of dense wind in natural medium of air that includes humidity, not dry air by mathematical approach.
In natural medium of air; variation of geostrophic wind with respect to height will be occurred, whenever, the field would be baroclinic medium and it is clear that the reason of baroclinity is "*the existence of horizontal gradient of density.*" For atmosphere; the horizontal gradient of density is related to the horizontal gradient of temperature as well as the horizontal gradient of humidity or in general; both of them. In troposphere, especially in planetary boundary layer – that can be extended until three thousand meter above the oceans' surface – there is the horizontal gradient of density because of existence of horizontal gradient of temperature, horizontal gradient of humidity or both of them; so, the field is baroclinic. Therefore; it is necessary that variation of geostrophic wind with respect to height would be study in real atmosphere carefully, i.e., atmosphere with humid air. Our aim in this paper is, looking to this subject in the condition of real atmosphere.
However, a question that arises from the above-mentioned introduction is; if we consider atmosphere as natural atmosphere including humidity; then how the looking to variation of the wind in vertical direction should be modify? In this paper, the variation of the geostrophic wind with respect to height will be considered in the natural atmosphere, not in dry air.

2. Geostrophic Wind

Geostrophic wind can be introduced by:

$$\mathbb{v}_g = f^{-1}\mathbb{k}_p \times \nabla_p \Phi \tag{1}$$

where in equation (1) $\mathbb{v}_g$ is geostrophic wind vector, f is Coriolis parameter, $\mathbb{k}$ is vertical unit vector in pressure coordinates system[1], ∇ is operator for gradient, Φ is geopotential and subscript p shows that equation (1) is written in pressure coordinates system.
Equation (1) shows the magnitude of geostrophic wind is proportional to the horizontal gradient of geopotential and is parallel to equipotential lines on isobaric surface.[8]
Writing eastward and northward components of geostrophic wind yields following equations:

$$u_g = -\frac{1}{f}\frac{\partial \Phi}{\partial y} \tag{2-a}$$

and

$$v_g = \frac{1}{f}\frac{\partial \Phi}{\partial x} \tag{2-b}$$

where in (2-a) u_g is eastward component of geostrophic wind or geostrophic current in ocean and in (2-b) v_g is northward component of geostrophic wind or geostrophic current in ocean.
By scale analysis of vertical component of momentum equation in midlatitudes and Cartesian coordinate system; we get hydrostatic approximation:

$$-\frac{1}{\rho}\frac{\partial p}{\partial z} - g \cong 0 \tag{3}$$

In equation (3) ρ is density, p is pressure, g is acceleration due to gravity and z is vertical coordinate

[1] In this paper; whenever we refer to *"pressure coordinates system*" our purpose is "*Cartesian coordinates system with pressure as vertical coordinate"*. Note this coordinates system is "*Left-handed system*".

of Cartesian coordinates system. In practice, most of researchers use equation (3) as hydrostatic equation same below:

$$\frac{dp}{dz} = -\rho g \tag{4}$$

Multiplying both sides of equation (4) by dz we get:

$$dp = -\rho g dz \tag{5}$$

Consider a layer of air that its lower level has p_1 pressure and $z_1$height; and its upper level has p_2 pressure and z_2 height. By integrating equation (5) from lower level to upper level of the layer, we get:

$$(p_1 - p_2) = \bar{\rho} g (z_2 - z_1) \tag{6}$$

Where $\bar{\rho}$ is average density of the layer and by means of neglecting variation of acceleration due to gravity for meteorological purposes. Noting that $p_2 < p_1$ and $z_1 < z_2$; if we call $(p_1 - p_2) = \delta p$, the partial pressure of column of air in the layer; and $(z_2 - z_1) = \delta z$, the partial height or thickness of the layer; from equation (6) and these assumptions, we have:

$$\delta p = \bar{\rho} g \delta z \tag{7}$$

Calculation of pressure in equation (7) shows height is function of pressure, density and acceleration due to gravity, same below:

$$\delta z = {}^{\delta p}/_{\bar{\rho} g} \tag{8}$$

By means of equation (8) whenever we pass on isobaric surface; increasing $\bar{\rho}$ decreases δz and decreasing $\bar{\rho}$ increases δz. Therefore, for the reason of variation of temperature's horizontal gradient or humidity's horizontal gradient on isobaric surface; there is the horizontal gradient of height, because according to the equation of state for moist air – that will introduce afterwards – density is a function of pressure, temperature and humidity.

The definition of geopotential in Cartesian coordinates system is [8]:

$$\Phi = gz \tag{9}$$

where Φ is geopotential. Geopotential is multiplication of height and acceleration due to gravity; therefore – in the case – geopotential varies in vertical direction because of variation of height, and geostrophic wind must have vertical shear in the presence of a horizontal density gradient, as can be shown easily from simple physical considerations based on hydrostatic equilibrium; then, geostrophic wind varies in vertical direction. Since the geostrophic wind [equation (1)] is proportional to the geopotential gradient on an isobaric surface. Therefore, a geostrophic wind directed along the positive y axis that increases in magnitude with height, requires the slop of the isobaric surface along the x axis for the reason of increasing height as well, as shown in Figure 1. According to the equation (8), δz – the thickness of isobaric layer – corresponds to variation of density.

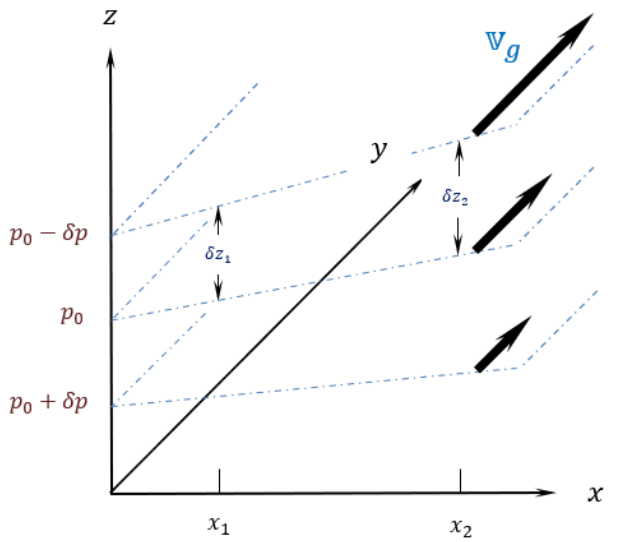

Figure 1. Relationship between vertical shear of the geostrophic wind and horizontal height gradients. (Note that $0 < \delta p$) [8]

3. Dense wind

The characteristic of baroclinic field, is that wind changes with respect to height, because of existence of the horizontal gradient of density. In this field, the geostrophic wind varies with height as well, as we can see in Figure 1.

3.1. Definition

"*Dense wind is vectorial difference of geostrophic wind vector at upper level and geostrophic wind vector at lower level*" (of the atmospheric layer), that is:

$$\mathbb{V}_D \equiv \mathbb{V}_{g(p_2)} - \mathbb{V}_{g(p_1)} \tag{10}$$

where in Equation (10) $\mathbb{V}_D$ stands for dense wind vector, $\mathbb{V}_g$ is geostrophic wind, and subscripts p_1 and p_2 refer to pressure levels in the manner that level p_2 has more height than level p_1 i.e., $p_2 < p_1$.

According to definition (10); eastward and northward components of dense wind can be shown as following:

$$u_D = u_{g(p_2)} - u_{g(p_1)} \tag{11-a}$$

and

$$v_D = v_{g(p_2)} - v_{g(p_1)} \tag{11-b}$$

Typical layer of atmospheric system is shown in Figure 2.

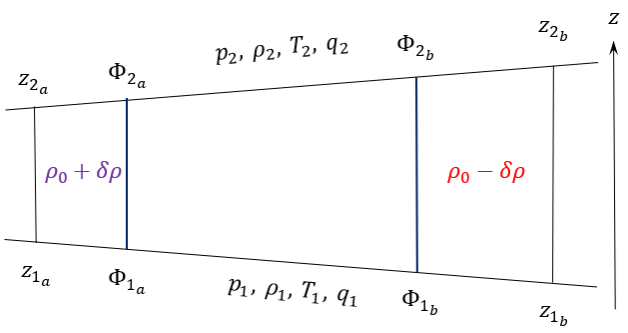

Figure 2. Typical layer of atmospheric system.

Despite its name, dense wind, while a vector, is not a true wind. Instead, it is a geostrophic wind shear, representing the change of wind with respect to height, causing some advections.

To derive dense wind equations, first consider the equation of state for humid air (common air) [10]. This equation has the form:

$$p = \rho_{\mathrm{M}}(1 + 0.608q)R_d T \tag{12}$$

where, p, ρ_{M}, q, R_d and T are air pressure, air density, specific humidity of air, gas constant for dry air and dry air temperature respectively.

If we introduce virtual temperature with following equation:

$$T_v = (1 + 0.608q)T \tag{13}$$

where, T_v is virtual temperature [11]; then the equation of the state for humid air can be written as:

$$p = \rho_{\mathrm{M}} R_d T_v \tag{14}$$

Where p is pressure, ρ_{M} is density of humid air, R_d is gas constant for dry air and T_v is virtual temperature.

Now, if we differentiate equations (2-a) and (2-b) with respect to p we get:

$$\frac{\partial u_g}{\partial p} = -\frac{1}{f}\frac{\partial}{\partial p}\left(\frac{\partial \Phi}{\partial y}\right) = -\frac{1}{f}\frac{\partial}{\partial y}\left(\frac{\partial \Phi}{\partial p}\right) \tag{15-a}$$

and

$$\frac{\partial v_g}{\partial p} = \frac{1}{f}\frac{\partial}{\partial p}\left(\frac{\partial \Phi}{\partial x}\right) = \frac{1}{f}\frac{\partial}{\partial x}\left(\frac{\partial \Phi}{\partial p}\right) \tag{15-b}$$

In pressure coordinates system, hydrostatic equation, applying for humid air and considering the equation of state; is [12]:

$$\frac{\partial \Phi}{\partial p} = -\alpha_{\mathrm{M}} = -\frac{1}{\rho_{\mathrm{M}}} = -\frac{R_d T_v}{p} \tag{16}$$

where α_{M} is specific volume of humid air and ρ_{M} is its density.

If we select equivalent of $\frac{\partial \Phi}{\partial p}$ from equation (16) that is $-\frac{1}{\rho_{\mathrm{M}}}$ and substitute in equations (15-a) and (15-b), we get:

$$\frac{\partial u_g}{\partial p} = -\frac{1}{f}\frac{\partial}{\partial y}\left(\frac{-1}{\rho_{\mathrm{M}}}\right) \tag{17-a}$$

and

$$\frac{\partial v_g}{\partial p} = \frac{1}{f}\frac{\partial}{\partial x}\left(\frac{-1}{\rho_{\mathrm{M}}}\right) \tag{17-b}$$

or

$$\frac{\partial u_g}{\partial p} = -\frac{1}{f(\rho_{\mathrm{M}})^2}\frac{\partial \rho_{\mathrm{M}}}{\partial y} \tag{18-a}$$

and

$$\frac{\partial v_g}{\partial p} = \frac{1}{f(\rho_{\mathrm{M}})^2}\frac{\partial \rho_{\mathrm{M}}}{\partial x} \tag{18-b}$$

which can be written as vector form:

$$\frac{\partial \mathbb{v}_g}{\partial p} = \frac{1}{f(\rho_{\mathrm{M}})^2}\mathbb{k}_p \times \nabla_p \rho_{\mathrm{M}} \tag{19-D-I}$$

we call the equation (19-D-I) as "*First version of Dense wind equation.*"

By integration of equation (19-D-I) from lower level p_1 to upper level p_2 $(p_2 < p_1)$ of the atmospheric layer; one can derive "*First version of Dense wind vector*":

$$\mathbb{v}_{g(p_2)} - \mathbb{v}_{g(p_1)} \equiv \mathbb{v}_{\mathrm{D_I}} = \frac{1}{f}\int_{p_1}^{p_2}\left(\frac{1}{(\rho_{\mathrm{M}})^2}\mathbb{k}_p \times \nabla_p \rho_{\mathrm{M}}\right) dp \tag{20-D-I}$$

where in equation (20-D-I); $\mathbb{v}_{g(p_2)}$ is geostrophic wind vector at upper level of the atmospheric layer, $\mathbb{v}_{g(p_1)}$ is geostrophic wind vector at lower level of the atmospheric layer, $\mathbb{v}_{\mathrm{D_I}}$ stands for first version of dense wind vector, f is Coriolis parameter, p_1 is atmospheric pressure at lower level of the atmospheric layer, p_2 is atmospheric pressure at upper level of the atmospheric layer, ρ_{M} stands for density of natural air, $\mathbb{k}_p$ is vertical unit vector in pressure coordinates system and ∇_p is gradient operator in pressure coordinates system.

Eastward and northward components of first version of dense wind can be derived by integration of equations (18.a) and (18.b) – similar to deriving equation (20-D-I) – directly or one can determine the eastward and northward components of first version of dense wind from equation (20-D-I) directly:

$$u_{\mathrm{D_I}} = -\frac{1}{f}\int_{p_1}^{p_2}\left(\frac{1}{(\rho_{\mathrm{M}})^2}\frac{\partial \rho_{\mathrm{M}}}{\partial y}\right) dp \tag{21-D-I-a}$$

and

$$v_{\mathrm{D_I}} = \frac{1}{f}\int_{p_1}^{p_2}\left(\frac{1}{(\rho_{\mathrm{M}})^2}\frac{\partial \rho_{\mathrm{M}}}{\partial x}\right) dp \tag{21-D-I-b}$$

where in equation (21-D-I-a) $u_{\mathrm{D_I}}$ is eastward component of dense wind and in equation (21-D-I-b) $v_{\mathrm{D_I}}$ stands for northward component of dense wind, both of them from first version of dense wind.

From first version of dense wind vector or its components; one can find out that:
A: If we go from pole to equator, dense wind becomes stronger[2];
B: If the atmospheric layer has more altitude; then dense wind becomes more powerful;
C: If the horizontal gradient of density would be greater, dense wind becomes stronger, because dense wind is proportional to the horizontal gradient of density, and finally;
D: If the pressure difference will be higher in the layer, dense wind becomes more powerful.
In this manner, representative of first version of dense wind vector, i.e., equation (20-D-I) shows that: "*dense wind blows parallel to Isopycnals, so that, light air is located at the left side of downwind.*" (In the northern hemisphere) This fact is illustrated in Figures 3 and 4.

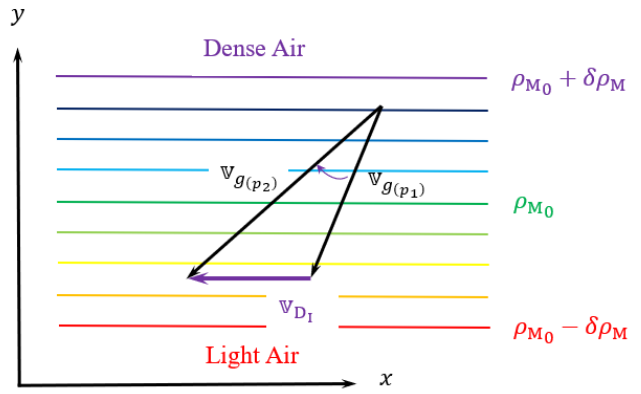

Figure 3. Clockwise rotating of geostrophic wind with respect to height; (Veering) and dense air advection.

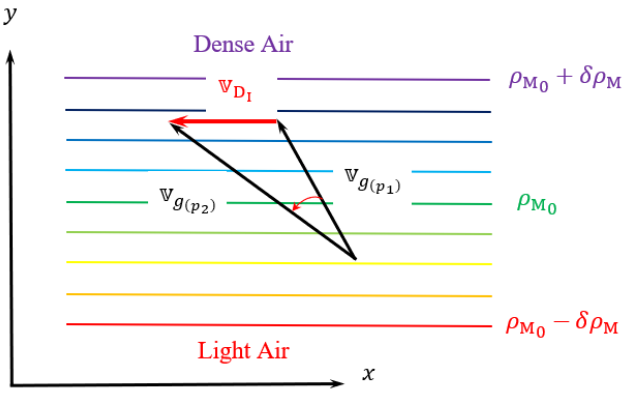

Figure 4. Counterclockwise rotation of geostrophic wind with respect to height (Backing) and light air advection.

In connection with Figure 3, clockwise turning of geostrophic wind with respect to height (veering) is associated with dense air advection by geostrophic wind in the layer. In other words; veering of geostrophic wind with respect to height associated with cold or dry air in the layer.
Conversely, as shown in Figure 4, counterclockwise turning of geostrophic wind with respect to height (backing) implies light air advection by geostrophic wind in the layer. In other words; backing of geostrophic wind with respect to height associated with advection of warm or moist air in the layer.
Therefore, it is possible to obtain a reasonable estimate of the horizontal light or dense air advection and its vertical dependence at a given location solely from data on the vertical profile of the wind given by a single sounding. Alternatively, the geostrophic wind at any level can be estimated from the advection of light or dense air field, provided that the geostrophic velocity is known at a single level.
Thus, for example, if the geostrophic wind at 850 h Pa is known and the mean horizontal density gradient in the layer 850 – 500 h Pa is also known, the first version of thermal wind equation can be applied to obtain the geostrophic wind at 500 h Pa.
Likewise, it is possible to introduce simpler forms of first version of dense wind vector and its components. Among of them there are:

$$\mathbb{v}_{D_I} = \frac{1}{f}\left\langle\frac{1}{(\rho_M)^2}\right\rangle\int_{p_1}^{p_2}\left(\mathbb{k}_p \times \nabla_p\rho_M\right)dp \qquad (22\text{-D-I})$$

with eastward component:

$$u_{D_I} = -\frac{1}{f}\left\langle\frac{1}{(\rho_M)^2}\right\rangle\int_{p_1}^{p_2}\frac{\partial\rho_M}{\partial y}dp \qquad (23\text{-D-I-a})$$

and northward component:

$$v_{D_I} = \frac{1}{f}\left\langle\frac{1}{(\rho_M)^2}\right\rangle\int_{p_1}^{p_2}\frac{\partial\rho_M}{\partial x}dp \qquad (23\text{-D-I-b})$$

Here the angle brackets in equations (22-D-I), (23-D-I-a) and (23-D-I-b) denote a vertical average.[3]
Even, one can introduces simpler form of first version of dense wind vector and its components same below:

$$\mathbb{v}_{D_I} = \frac{1}{f}\left\langle\frac{1}{(\rho_M)^2}\right\rangle\langle\mathbb{k}_p \times \nabla_p\rho_M\rangle(p_2 - p_1) \qquad (24\text{-D-I})$$

with eastward component:

$$u_{D_I} = -\frac{1}{f}\left\langle\frac{1}{(\rho_M)^2}\right\rangle\left(\frac{\partial\langle\rho_M\rangle}{\partial y}\right)_p(p_2 - p_1) \qquad (25\text{-D-I-a})$$

and northward component:

$$v_{D_I} = \frac{1}{f}\left\langle\frac{1}{(\rho_M)^2}\right\rangle\left(\frac{\partial\langle\rho_M\rangle}{\partial x}\right)_p(p_2 - p_1). \qquad (25\text{-D-I-b})$$

[2] Use of geostrophic wind in tropical regions must be with careful deliberation because geostrophic wind in these regions is magnified and especially on equator is meaningless.

[3] There are many procedures about averaging in meteorology. Every method for averaging particular parameter or term, is related to position, time and specifications of the medium. All meteorological or oceanographical parameters; decreases logarithmic or semi-logarithmic and increases exponentially or semi-exponentially with respect to height or depth. Therefore, for every case, we need to use special manner for it. As a simple example, if we consider a layer of air between 500 and 300 hectopascals, the easiest way is using linear averaging, i.e., adding the value of parameters or terms of above and below the layer and dividing the result by 2.

3.2. Second version of dense wind

It can be shown that if we choose equivalent of $\frac{\partial \Phi}{\partial p}$, $-\frac{R_d T_v}{p}$, instead of $-\frac{1}{\rho_M}$ from equation (16) and substitute in equations (15-a) and (15-b); then differentiate these equations with respect to p, one can obtain another version of dense wind equation, dense wind vector and its components as following forms respectively:

$$\frac{\partial u_g}{\partial p} = -\frac{1}{f}\frac{\partial}{\partial y}\left(-\frac{R_d T_v}{p}\right) \quad (26\text{-a})$$

and

$$\frac{\partial v_g}{\partial p} = \frac{1}{f}\frac{\partial}{\partial x}\left(-\frac{R_d T_v}{p}\right) \quad (26\text{-b})$$

or

$$\frac{\partial u_g}{\partial \ln p} = \frac{R_d}{f}\frac{\partial T_v}{\partial y} \quad (27\text{-a})$$

and

$$\frac{\partial v_g}{\partial \ln p} = -\frac{R_d}{f}\frac{\partial T_v}{\partial x} \quad (27\text{-b})$$

Equations (27-a) and (27-b) can be written in the vector form in the following line:

$$\frac{\partial \mathbb{v}_g}{\partial \ln p} = -\frac{R_d}{f}\left(\mathbb{k}_p \times \nabla_p T_v\right) \quad (19\text{-D-II})$$

we call the equation (19-D-II) as "*second version of Dense wind equation.*"

By integration of equation (19-D-II) from lower level p_1 to upper level p_2 $(p_2 < p_1)$ of the atmospheric layer; one can derive "*second version of Dense wind vector*":

$$\mathbb{v}_{g(p_2)} - \mathbb{v}_{g(p_1)} \equiv \mathbb{v}_{D_{II}} = -\frac{R_d}{f}\int_{p_1}^{p_2}\left(\mathbb{k}_p \times \nabla_p T_v\right) d \ln p \quad (20\text{-D-II})$$

where in equation (20-D-II); $\mathbb{v}_{g(p_2)}$ is geostrophic wind vector at the upper level of the atmospheric layer, $\mathbb{v}_{g(p_1)}$ is geostrophic wind vector at the lower level of the atmospheric layer, $\mathbb{v}_{D_{II}}$ stands for second version of dense wind vector, f is Coriolis parameter, p_1 is atmospheric pressure at the lower level of the atmospheric layer, p_2 is atmospheric pressure at the upper level of the atmospheric layer, $\mathbb{k}_p$ is vertical unit vector in pressure coordinates system, ∇_p is gradient operator in pressure coordinates system and T_v stands for virtual temperature of natural air.

Eastward and northward components of second version of dense wind in this point of view, can be derived by integration of equations (27.a) and (27.b) directly or decompose of second version of dense wind vector (20-D-II) presently:

$$u_{g(p_2)} - u_{g(p_1)} \equiv u_{D_{II}} = \frac{R_d}{f}\int_{p_1}^{p_2}\frac{\partial T_v}{\partial y} d \ln p \quad (21\text{-D-II-a})$$

and

$$v_{g(p_2)} - v_{g(p_1)} \equiv v_{D_{II}} = -\frac{R_d}{f}\int_{p_1}^{p_2}\frac{\partial T_v}{\partial x} d \ln p \quad (21\text{-D-II-b})$$

where in equation (21-D-II-a) $u_{D_{II}}$ is eastward component of second version of dense wind and in equation (21-D-II-b) $v_{D_{II}}$ stands for northward component of second version of dense wind.

From second version of dense wind vector or its components; one can find out that:

A: If we go from pole to equator, dense wind becomes stronger (with pay attention to footnote No. 2);

B: If the horizontal gradient of virtual temperature would be greater, dense wind becomes stronger, because, dense wind is proportional to the horizontal gradient of virtual temperature, and finally;

C: If the pressure difference will be higher in the layer, dense wind becomes more powerful.

In this manner, representative of second version of dense wind vector, i.e., equation (20-D-II) shows that: "*dense wind blows parallel to Isopleths of virtual temperature so that, greater virtual temperature is located at the right side of downwind.*" (In the northern hemisphere) This is illustrated in Figures 5 and 6.

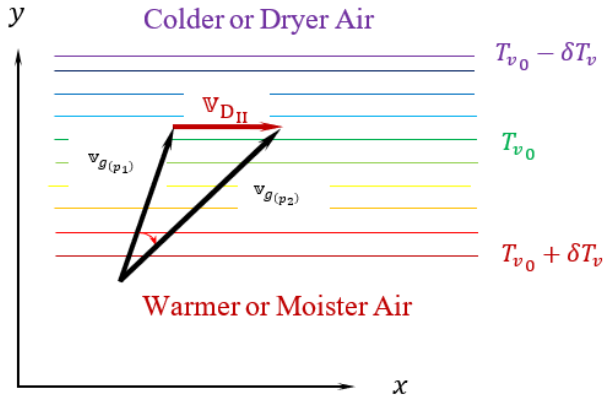

Figure 5: Clockwise rotation of geostrophic wind with respect to height. (Veering) and warmer or moister air advection.

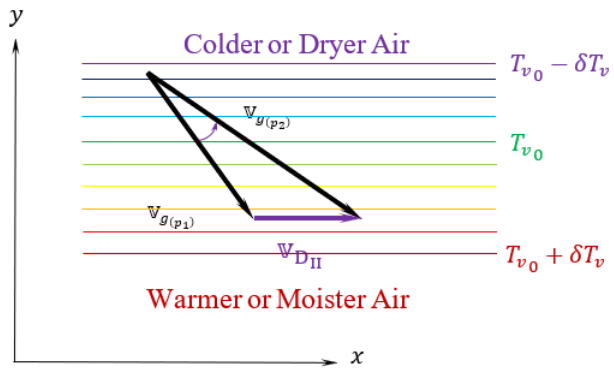

Figure 6: Counterclockwise rotation of geostrophic wind with respect to height. (Backing) and colder or dryer air advection.

In connection with Figure 5; clockwise turning of geostrophic wind with respect to height (veering) is associated with warmer or moister air advection by geostrophic wind in the layer. Conversely, as shown in Figure 6; counterclockwise turning of geostrophic wind with respect to height (backing) implies colder or dryer air advection by geostrophic wind in the layer.
In a similar way, it is possible to introduce simpler forms of second version of dense wind vector and its components in the following lines:

$$\mathbb{v}_{\mathrm{D_{II}}} = -\frac{R_d}{f}\langle \mathbb{k}_p \times \nabla_p T_v \rangle \ln\left(\frac{p_2}{p_1}\right) \qquad \text{(22-D-II)}$$

$$u_{\mathrm{D_{II}}} = \frac{R_d}{f}\frac{\partial \langle T_v \rangle}{\partial y} \ln\left(\frac{p_2}{p_1}\right) \qquad \text{(25-D-II-a)}$$

$$v_{\mathrm{D_{II}}} = -\frac{R_d}{f}\frac{\partial \langle T_v \rangle}{\partial x} \ln\left(\frac{p_2}{p_1}\right) \qquad \text{(25-D-II-b)}$$

In equations (22-D-II), (25-D-II-a) and (25-D-II-b); broken brackets refer to average value of term or parameter in the atmospheric layer.
Therefore, it is possible to obtain a reasonable estimate of the horizontal mean virtual temperature advection and its vertical dependence at a given location solely from data on the vertical profile of the wind given by a single sounding. Alternatively, the geostrophic wind at any level can be estimated from the advection of mean virtual temperature field, provided that the geostrophic velocity is known at a single level. Thus, for example, if the geostrophic wind at 850 hectopascals level is known and the mean horizontal virtual temperature gradient in the layer of 850–500 hectopascals is also known, the second dense wind equation can be applied to obtain the geostrophic wind at 500 hectopascals.

3.3. Third version of dense wind

Furthermore; there is another version of dense wind. This version of dense wind is originated form the thickness of the atmospheric layer.
Consider hydrostatic equation in Cartesian coordinates system:

$$\frac{dp}{dz} = -\rho g \qquad (4)$$

Parameters in equation (4) have been introduced after equation (3). By considering equation (9); equation (4) can be written:

$$-\frac{dp}{\rho} = g dz = d\Phi \qquad (28)$$

where $d\Phi$ is differential part of geopotential. Atmosphere has humidity, therefore; equation (28) for moist air can be written as:

$$d\Phi = -\frac{dp}{\rho_{\mathrm{M}}} \qquad (29)$$

where ρ_{M} stands for density of (natural) air.

Consider equation of state for moist air [equation (14)], computation of density of moist air from equation (14) yields:

$$\rho_{\mathrm{M}} = \frac{p}{R_d T_v} \qquad (30)$$

If we substitute equivalent of ρ_{M} from equation (30) into equation (29), yields:

$$d\Phi = -R_d T_v \frac{dp}{p} = -R_d T_v d \ln p \qquad (31)$$

Getting approximate increasing parts of equation (31), yields:

$$\delta\Phi = -R_d T_v \, \delta \ln p \qquad (32)$$

If we integrate equation (31) with respect to vertical coordinate; from the below of atmospheric layer with pressure p_1 and geopotential $\Phi_1$to the upper layer of it with pressure p_2 and geopotential Φ_2 as Figure 2 shows; we get:

$$\int_{p_1}^{p_2} d\Phi = -R_d \int_{p_1}^{p_2} T_v d \ln p \qquad (33)$$

After calculating equation (33), we have:

$$\delta\Phi \equiv (\Phi_2 - \Phi_1) = R_d \int_{p_2}^{p_1} T_v \, d \ln p \qquad (34)$$

where $\delta\Phi$ is the thickness of the layer by geopotential and equation (34) shows that the thickness of the atmospheric layer is proportional to vertical average of virtual temperature when we consider an atmospheric layer. Therefore, we call it "*The thickness equation*".
Consider equations (15-a) and (15-b):

$$\frac{\partial u_g}{\partial p} = -\frac{1}{f}\frac{\partial}{\partial y}\left(\frac{\partial \Phi}{\partial p}\right) \qquad \text{(15-a)}$$

and

$$\frac{\partial v_g}{\partial p} = \frac{1}{f}\frac{\partial}{\partial x}\left(\frac{\partial \Phi}{\partial p}\right) \qquad \text{(15-b)}$$

And, equations (15-a) and (15-b) can be written in the vector form as bellow:

$$\frac{\partial \mathbb{v}_g}{\partial p} = \frac{1}{f}\mathbb{k}_p \times \nabla_p\left(\frac{\partial \Phi}{\partial p}\right) \qquad \text{(19-D-III)}$$

Equation (19-D-III) is called "*third version of dense wind equation.*"
By vertical integrating of equation (19-D-III) from the below level of the atmospheric layer with pressure p_1 and geopotential Φ_1 to the upper level of this atmospheric layer with pressure p_2 and geopotential Φ_2; we get:

$$\mathbb{v}_{g(p_2)} - \mathbb{v}_{g(p_1)} \equiv \mathbb{v}_{\mathrm{D_{III}}} = \frac{1}{f}\int_{p_1}^{p_2}\left[\mathbb{k}_p \times \nabla_p\left(\frac{\partial \Phi}{\partial p}\right)\right] dp \qquad (35)$$

Therefore, the "*third version of dense wind vector*" is:

$$\mathbb{v}_{\mathrm{D_{III}}} = \frac{1}{f}\mathbb{k}_p \times \nabla_p(\Phi_2 - \Phi_1) \qquad \text{(20-D-III)}$$

The third version of dense wind shows dense wind is proportional to thickness gradient of the atmospheric layer.

Now, we can derive eastward and northward components of third version of dense wind from equation (20-D-III) directly or integrating equations (15-a) and (15-b) with respect to vertical coordinate; from the below of atmospheric layer with pressure p_1 and geopotential Φ_1 to the upper of atmospheric layer with pressure p_2 and geopotential Φ_2 as is shown in Figure 2; we get:

$$\int_{p_1}^{p_2} \frac{\partial u_g}{\partial p}\, dp = -\frac{1}{f}\int_{p_1}^{p_2} \frac{\partial}{\partial y}\left(\frac{\partial \Phi}{\partial p}\right) dp = -\frac{1}{f}\frac{\partial}{\partial y}\int_{p_1}^{p_2} d\Phi \qquad \text{(36-a)}$$

and

$$\int_{p_1}^{p_2} \frac{\partial v_g}{\partial p}\, dp = \frac{1}{f}\int_{p_1}^{p_2} \frac{\partial}{\partial x}\left(\frac{\partial \Phi}{\partial p}\right) dp = \frac{1}{f}\frac{\partial}{\partial x}\int_{p_1}^{p_2} d\Phi \qquad \text{(36-b)}$$

Calculation's results of above equations are as follows:

$$u_{g(p_2)} - u_{g(p_1)} \equiv u_{\mathrm{D_{III}}} = -\frac{1}{f}\frac{\partial}{\partial y}(\Phi_2 - \Phi_1) \qquad \text{(21-D-III-a)}$$

and

$$v_{g(p_2)} - v_{g(p_1)} \equiv v_{\mathrm{D_{III}}} = \frac{1}{f}\frac{\partial}{\partial x}(\Phi_2 - \Phi_1) \qquad \text{(21-D-III-b)}$$

From third version of dense wind vector or its components; one can find out that:

A: If we go from pole to equator, dense wind becomes stronger (with pay attention to footnote No. 2);

B: If the horizontal gradient of the thickness of atmospheric layer would be greater, dense wind becomes stronger, because, dense wind is proportional to the horizontal gradient of the thickness of the atmospheric layer, and finally;

C: If the geopotential difference between lower level and upper level of the atmospheric layer will be higher, dense wind becomes more powerful.

In this manner, representative of third version of dense wind vector, i.e., equation (20-D-III) shows that: "*dense wind blows parallel to isolines of thickness of the atmospheric layer so that, more thickness of the layer is located at the right side of downwind.*" (In the northern hemisphere) This is illustrated in Figures 7 and 8.

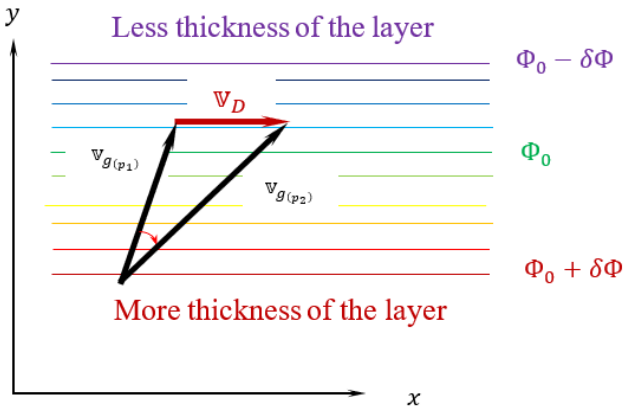

Figure 7: Clockwise rotation of geostrophic wind with respect to height. (Veering) and more thickness advection.

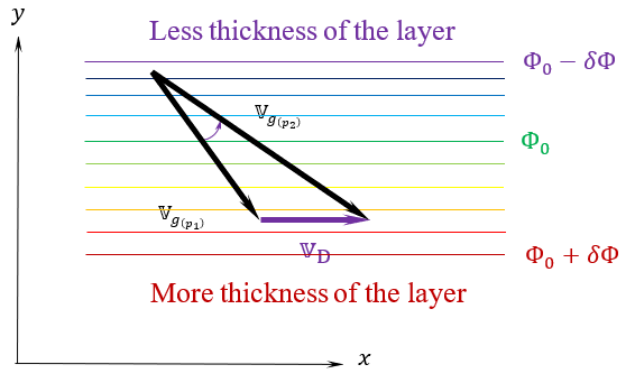

Figure 8: Counterclockwise rotation of geostrophic wind with respect to height. (Backing) and less thickness advection.

Therefore, it is possible to obtain a reasonable estimate of the horizontal more (or less) thickness advection of the atmospheric layer and its vertical dependence at a given location solely from data on the vertical profile of the wind given by a single sounding. Alternatively, the geostrophic wind at any level can be estimated from the advection of more (or less) thickness of the atmospheric layer, provided that the geostrophic velocity is known at a single level. Thus, for example, if the geostrophic wind at 700 hectopascals level is known and the more (or less) thickness advection in the layer 700–500 hectopascals is also known; the advection of more (or less) thickness, can be applied to third version of dense wind for obtain the geostrophic wind at 500 hectopascals level.

4. Results and Discussion

All versions of the dense wind equation are an extremely useful diagnostic tools, which is often used to check analyses of the observed wind field for consistency.

It can also be used to estimate the mean horizontal dense air, virtual temperature and thickness advections in an atmospheric layer as shown in Figures 3, 4, 5, 6, 7 and 8 respectively.

Dense wind – as exist in the nature of atmosphere except somewhere that thermal wind or moist wind is true – is struggle of the atmosphere to return

thermodynamic equilibrium and complete the dynamic cycle of atmosphere. This movement begins from the fact that solar radiation disturbs the thermodynamic equilibrium resulting production of horizontal gradient of density. Horizontal gradient of density produces horizontal gradient of potential energy and in turn, this condition forces atmosphere to generate horizontal gradient of pressure and finally, it causes to blow wind for returning thermodynamic equilibrium of atmosphere.

Concerning various insolation and non-uniform transfer of diffusion of heat and humidity in the different layers of the atmosphere; horizontal gradients of density are not same in the layers and wind velocities cannot be the same at atmospheric layers. Therefore, this phenomenon produces dense wind that is effort of atmosphere to adjust horizontal gradient of density and reducing dense wind speed. By continuous reduction of dense wind speed, thermodynamic disequilibrium of atmosphere weakens and weakens, until returning of thermodynamic equilibrium of the atmosphere. If we assume there will be no more solar radiation, finally the wind will be disappeared in presence of friction.

So, dense wind is the key of understanding of dense or light air; virtual temperature or thickness of the atmospheric layer advections and one of the mechanisms of returning thermodynamic equilibrium of atmosphere.

5. Conclusions

Looking at the variation of the geostrophic wind with respect to height, shouldn't limit to dry atmosphere because the atmosphere has humidity and not dry and strictly in general, the air is not dry. Therefore, the variation of the geostrophic wind with respect to height should be describe with better tool, namely *dense wind*. It is necessary to note two basic points. First; until God wills and sun radiates; atmospheric and oceanic mediums are baroclinic. And the theory of barotropic medium – same as geostrophic wind – is acceptable for simplification of meteorological and oceanic analyses. Second point is with regard to more affection of temperature in variation of air density; although in many places far from oceanic medium, the dense wind gains energy more from horizontal gradient of temperature rather than the horizontal gradient of humidity, but it is not sufficient reason to call the vectorial difference of the geostrophic wind at upper and lower level of the layer as thermal wind, because we cannot deny presence of humidity anywhere.

List of Symbols

Symbol	Description
f	Coriolis parameter
g	Acceleration due to gravity
$\mathbb{k}_p$	Vertical unit vector in pressure coordinates system
p	Pressure, vertical coordinate of pressure coordinates system
p_0	Reference pressure
p_1	Pressure of below level of layer
p_2	Pressure of upper level of layer
q	Specific humidity
q_1	Specific humidity of lower level of layer
q_2	Specific humidity of upper level of layer
R_d	Gas constant for dry air
T	Temperature
T_1	Temperature of below level of layer
T_2	Temperature of upper level of layer
T_v	Virtual temperature
T_{v0}	Reference virtual temperature
u	Eastward component of velocity
u_{D}	Eastward component of dense wind
$u_{\mathrm{D_I}}$	1st Ver. of, eastward component of dense wind
$u_{\mathrm{D_{II}}}$	2nd Ver. of, eastward component of dense wind
$u_{\mathrm{D_{III}}}$	3rd Ver. of, eastward component of dense wind
u_g	Eastward component of geostrophic wind
v	Northward component of velocity
v_{D}	Northward component of dense wind
$v_{\mathrm{D_I}}$	1st Ver. of Northward component of dense wind
$v_{\mathrm{D_{II}}}$	2nd Ver. of Northward component of dense wind
$v_{\mathrm{D_{III}}}$	3rd Ver. of Northward component of dense wind
v_g	Northward component of geostrophic wind
$\mathbb{v}_{\mathrm{D}}$	Dense wind vector
$\mathbb{v}_{\mathrm{D_I}}$	1st Ver. of Dense wind vector
$\mathbb{v}_{\mathrm{D_{II}}}$	2nd Ver. of Dense wind vector
$\mathbb{v}_{\mathrm{D_{III}}}$	3rd Ver. of Dense wind vector
$\mathbb{v}_g$	Geostrophic wind vector
x	Eastward direction
x_1	First distance
x_2	Second distance
y	Northward direction
z	Height, vertical coordinate of Cartesian coordinates system
z_1	Height of below level of layer
z_2	Height of upper level of layer
α_{M}	Specific volume of humid air
δp	Increment of pressure
$\delta \ln p$	Increment of natural logarithm of pressure
δT_v	Increment of virtual temperature
δz	Increment of height
δz_1	Increment of height for first distance
δz_2	Increment of height for second distance
$\delta \rho$	Increment of density
$\delta \Phi$	Increment of geopotential

ρ	Density
ρ_0	Reference density
ρ_1	Density of lower level of layer
ρ_2	Density of upper level of layer
ρ_M	Density of humid air
$\bar{\rho}$	Average density
Φ	Geopotential
Φ_0	Reference geopotential
Φ_1	Geopotential of lower level of layer
Φ_2	Geopotential of upper level of layer
ln ...	Natural logarithm
∇_p	Gradient operator in pressure coordinates system
$\langle ... \rangle$	Vertical average

8. References

[1] Charnock, H., Francis, J. R. D. and Sheppard, P. A., (1956), *An Investigation of Wind Structure in the Trades: Anegada 1953*. Philosophical Transactions of the Royal Society of London, Ser. A, **249**, 179-234.

[2] Carlstead, M., (1959), Forecasting Middle Cloudiness and Precipitation Areas by Numerical Methods. *Mon. Wea. Rev.*, **87**, 375-381.

[3] Estoque, M. A., (1971), The Planetary Boundary Layer Wind over Christmas Island. *Mon. Wea. Rev.*, **99**, 193-201.

[4] Foster, R. C. and Levy, G., (1998), *The Contribution of Organized Roll Vortices to the Surface Wind Vector in Baroclinic Conditions*, Journal of the Atmospheric Science, **55** (8), p.1466-1472.

[5] Hess, S. L., (1959), *Introduction to Theoretical Meteorology*, Malabar, Krieger Publishing, xiv + 364 pp.

[6] Gill, A. E., (1982), *Atmosphere-Ocean Dynamics*, San Diego, Academic press, xv + 662 pp.

[7] Dutton, J. A., (1995), *Dynamics of Atmospheric Motion*, New York, Dover Publications, Inc., xx + 617 pp.

[8] Holton, J. R. and, G. J. Hakim, (2013), *An Introduction to Dynamic Meteorology*, Amsterdam, 5th edition, Elsevier, xvi + 532 pp.

[9] Glickman, T. S. (managing editor), (2000), *Glossary of Meteorology*, Boston, 2nd edition, American Meteorological Society, xii + 855 pp.

[10] Curry J. A. and P. J. Webster, (1999), *Thermodynamics of Atmosphere and Oceans*. San Diego, Academic Press, xvii + 471pp.

[11] Iribarne, J. V. and W. L. Godson, (1981), *Atmospheric Thermodynamics*. Dordrecht, D. Reidel Publishing Co., xv + 259 pp.

[12] Haltiner, G. J. and R. T. Williams, (1980), *Numerical Prediction and Dynamic Meteorology*. New York, John Wiley & Sons, xvii + 477 pp

INTERNATIONAL JOURNAL OF
COASTAL, OFFSHORE & ENVIRONMENTAL ENGINEERING IJCOE Vol.7/No. 3/Summer 2022 (20-30)

Available online at: www. Ijcoe.org

Assessment of long-term consistency of ocean-color satellite-derived chlorophyll-a products in the Persian Gulf

Masoud Moradi[1*,2]

*[*1] Iranian National Institute of Oceanography and Atmospheric Science (INIOAS); Moradi_msd@yahoo.com*
[2] Center for International Scientific Studies & Collaboration (CISSC), ministry of Science Research and Technology, Tehran, Iran

ARTICLE INFO

Article History:
Received: 07 Dec. 2021
Accepted: 16 Aug. 2022

Keywords:
Remote sensing
Ocean color
Atmospheric correction
Coastal waters
Correlation analysis

ABSTRACT

Over the past two decades, several ocean color satellites have operated in parallel. The combination of different ocean color satellite sensor products is a vital task for studying the biogeochemistry of seas. In this study, we evaluated the temporal consistency of the monthly time-series and monthly interannual variations of satellite-derived chlorophyll-a concentrations (Chl-*a*) from four satellite sensors during 2002-2020 period over the Persian Gulf. Statistical correlation between Chl-*a* time series and anomalies from selected satellite sensors were significantly correlated for 84% area of the Persian Gulf. Correlations were reasonably sensitive to the choice of Chl-*a* retrieval and atmospheric correction algorithms. The standard algorithms for Chl-*a* retrieval showed the lowest value of correlations, and it was indicated that these algorithms were not suitable for Chl-*a* estimations from satellite sensors over the Persian Gulf. The OCI algorithm for Chl-*a* retrieval showed more consistency among different satellite sensors and it was shown that it is more suitable than previous ones for estimation of Chl-a from selected satellite sensors. Also, it was shown that the SeaDAS and POLYMER atmospheric correction algorithms have a great influence on the Chl-*a* estimations from selected satellite sensors. It was shown that more than 70% of the study area indicated imperfect consistency between selected atmospheric correction algorithms applied on different satellite sensors. Choosing the best atmospheric correction and Chl-*a* retrieval algorithms is the most important task in the estimation and utilization of Chl-a in the Persian Gulf.

1. Introduction

Phytoplankton biomass is a crucial indicator of ocean biology, and it has been used to predict climate change and the state of the oceans [1–3]. Understanding of ocean biology and marine ecosystems, and as well as their interactions, would be achieved by knowledge of spatial and temporal variations of phytoplankton biomass [4–6]. Long-term and interannual variations phytoplankton biomass and primary productivity and of the marine ecosystem are economically important in fisheries and marine resource management [7,8]. The near-surface chlorophyll-a concentration derived from ocean color sensors (Chl-*a*) is the most valuable factor to study the phytoplankton biomass [9].

Various ocean color satellite sensors have produced useful long-term data collections over the ocean's surface layer for the past three decades [7,10,11]. Remote sensing of ocean color is expected to be the primary source of data for detecting long-term changes in phytoplankton biomass due to the spatial and temporal sampling capabilities of corresponding satellite data [12]. However, the lifespans recent satellites (5-10 years) are insufficient to analyze the response of phytoplankton biomass to climate change and the other long-term climatological and environmental indicators [13]. In this regard, combination of different satellite sensor datasets is an ideal approach to study the changes in phytoplankton biomass and the effect of climate and environmental factors on their variabilities [3,12]. During the past three decades, many ocean color satellites have been lunched to study the biological characteristics of the oceans and marine environments. Among them, Sea-viewing Wide Field-of-view Sensor (SeaWiFS) (1997-2010), Moderate Resolution Imaging Spectrometer (MODIS) (2002-present), Medium Resolution Imaging Spectrometer (MERIS) (2002-2012), and Visible Imager Radiometer (VIIRS) (2011-present) have been used extensively in biological oceanography.

Several researches have tried to evaluate the variability and seasonal cycles of Chl-*a* estimated from two or more ocean-color satellite sensors [14–16]. However, there are limited documents on the consistency of seasonal and interannual variations of Chl-*a* among SeaWiFS, MERIS, MODIS, and VIIRS in a long-period (e.g. >10 years). Furthermore, the sensitivity of the different Chl-*a* retrieval algorithms and atmospheric-correction have not been considered in the assessment of multi merged ocean color satellite sensors applications. consequently, temporal consistency of correlation between Chl-*a* products from different satellite sensors remains a challenging issue.

In this paper, we demonstrate the seasonal and interannual fluctuations in monthly Chl-*a* products for SeaWiFS, MERIS, MODIS, and VIIRS over the Persian Gulf using statistical methods.

2. Data and Methods

2.1. Study area

Persian Gulf is a shallow marginal sea which connects to the Gulf of Oman through the Strait of Hormuz. Persian Gulf is dominantly shallow with average depth of 30 m and maximum depth of ~90 m [17]. The surrounding areas are hot and dry during March-October, and precipitation rate is very low (<300 mm y^{-1}) [18]. Persian Gulf is surrounded by deserts where are the source of frequent dust storms. The number of observed dust storms reach 15-20 per year and usually caused by winds blowing from Arabian Sea (*Shamal* wind) and north-east Africa [19]. Surface currents enters the Gulf from Strait of Hormuz and then reverse back along the southern coasts [20,21].

Many researchers have used ocean color data to study the spatial-temporal variations and dynamics of phytoplankton in the Persian Gulf [16,22–24]. Phytoplankton growth is highly influenced by dust deposition and fertilization in the Persian Gulf which leads to monstrous growth and generation of algal blooms [23,25,26]. Oceanographic and atmospheric factors are the main parameters that control the variability of Chl-*a* in this area. Consequently, the effect of these factors on optical properties of atmosphere and Chl-*a* retrieval algorithms increase the uncertainties in the satellite-derived Chl-*a* concentrations. To date, several studies aimed to evaluate the effect of atmosphere on Chl-*a* accuracy in the southern parts of the Persian Gulf [15,27]. However, the accuracy of Chl-*a* retrieval algorithms and also consistency of long-term Chl-*a* series from different satellite sensors have not been determined. To evaluate the effect of uncertainties on the Chl-*a* retrieval algorithms, we have to compare the available Chl-*a* products and determine how they are comparable, and how they are affected by atmospheric and retrieval algorithms.

2.2. Satellite data

The monthly level-3 Standard Mapped Imageries of SeaWiFS, MERIS, MODIS, and VIIRS Chl-*a* datasets with spatial resolution 4km×4km were downloaded from NASA ocean-color website (http://oceancolor.gsfc.nasa.gov/) for the time period 2002-2020. The selected datasets have been processed using a conceptually similar atmospheric correction algorithm [3,28] and Chl-*a* retrieval algorithms [29,30]. The performed atmospheric correction is considered as a common framework that removes the bad data influenced by high sensor view angle, high solar-zenith angels, high aerosol loads, sun glint and stray-light contamination. The Chl-*a* retrieval algorithms estimate the chlorophyll-*a* concentrations using empirical blue-green reflectance band ratio, and tune the specific wavelengths of each sensor. We used monthly datasets because: (i) they are usually the smallest time frame during which the highest spatial coverage for a single sensor may be achieved (>80%) [31], (ii) the results of this study may be comparable with previous studies that use long-term analysis [9,32,33], (iii) unwanted satellite sensor noises are filtered in the monthly averaged time-series data, and (iv) it reduces the analysis computing time.

In addition to the above standard Chl-*a* products, other Chla- datasets have been downloaded and processed during the same period and similar spatial properties from the NASA ocean-color website to evaluate the consistency of Chl-a time-series on a single sensor, and among the selected four sensors. This help us to select the best Chl-*a* dataset from each single sensor and decide how different atmospheric correction and Chl-*a* retrieval algorithms influence the products. The GSM or OCI bio-optical algorithms have been used to process these additional Chl-*a* products. The GSM algorithm considers the absorption by combined detrital and dissolved matter and particle backscattering to retrieve Chl-*a* using a semi-analytical inversion model [34,35]. The OCI performs a band-difference of remote-sensing reflectance in the green part of the visible spectrum, and tunes the results using a linear baseline between blue and red wavebands [30,36]. This algorithm is applicable only in oligotrophic waters where Chl-*a*<0.25 mg m^{-3} and reverts to standard band-ratio algorithm at higher Chl-*a*>0.3 mg m^{-3}.

In addition to the standard MERIS data, additional MERIS datasets were processed using a different atmospheric correction algorithm called POLYMER to evaluate the sensitivity of Chl-*a* time-series to the variations of atmospheric correction algorithms. The standard Chl-*a* products have been processed using SeaDAS atmospheric correction algorithm. In contrast,

Table 1- List of satellite datasets used in this study. The acronyms in the last column indicate the performed atmospheric correction and chlorophyll-a retrieval algorithms, and are used as reference to the selected corresponding dataset.

Sensor	Atmospheric correction	Chl-*a* retrieval	Duration	Acronym	
SeaWiFS	SeaDAS	OC4	1997-2010	SeaWiFS-SO	*Comparison-I*
MERIS	SeaDAS	OC4E	2002-2012	MERIS-SO	
MODIS	SeaDAS	OC3M	2002-present	MODIS-SO	
VIIRS	SeaDAS	OC3V	2012-present	VIIRS-SO	
MODIS	SeaDAS	OC3M	2002-present	MODIS-SO	*Comparison-II*
MODIS	SeaDAS	GSM	2002-present	MODIS-SG	
MODIS	SeaDAS	OCI	2002-present	MODIS-SI	
MERIS	SeaDAS	OC4E	2002-2012	MERIS-SO	*Comparison-III*
MODIS	SeaDAS	GSM	2002-present	MODIS-SG	
SeaWiFS	SeaDAS	OCI	1997-2010	SeaWiFS-SI	
MERIS	POLYMER	OC4E	2002-2012	MERIS-PO	*Comparison-IV*
SeaWiFS	SeaDAS	OC4	1997-2010	SeaWiFS-SO	
MODIS	SeaDAS	OC3M	2002-present	MODIS-SO	
MERIS	SeaDAS	OC4E	2002-2012	MERIS-SO	

POLYMER algorithm is a coupled ocean-atmosphere algorithm based on spectral optimization, and it conceptually differs with SeaDAS [9]. The POLYMER algorithm for MERIS sensor shows a more ability to perform in the presence of sun glint, and therefore it generates extensible spatial coverage that did not observe in the other atmospheric correction algorithms [3].

The list of selected Chl-*a* datasets and corresponding atmospheric correction and Chl-*a* retrieval algorithms are show in Table 1. Here, the following four comparisons were made:

- *Comparison-I*: Chl-*a* datasets of SeaWiFS-SO, MERIS-SO, MODIS-SO, and VIIRS-SO were used to compare their temporal consistency during the study period using a common framework.
- *Comparison-II*: Chl-*a* datasets of MODIS-SO, MODIS-SG, and MODIS-SI were used to assess the impacts of different Chl-*a* retrieval algorithms on the temporal comparisons of a single sensor.
- *Comparison-III*: Chl-*a* datasets of MERIS-SO, MODIS-SG, and SeaWiFS-SI were used to assess the impacts of different Chl-*a* retrieval algorithms on the temporal consistency of different sensors.
- *Comparison-IV*: Chl-*a* datasets of SeaWiFS-SO, MODIS-SO, MERIS-SO, and MERIS-PO were used to assess the impacts of different atmospheric correction algorithms on the temporal consistency of Chl-*a* time-series.

In general, Chl-*a* datasets are log-normally distributed over the coastal areas and marginal seas [37]. Hence, all Chl-*a* imageries were transformed in Log_{10} bases prior to further analysis.

2.3. Calculate monthly climatology and anomaly

Monthly climatologies of the selected datasets were produced at each grid pixel. The Chl-*a* monthly climatology products of each satellite sensors were calculated for the whole period using Climate Data Toolbox for MATLAB® [38]. To calculate the monthly climatologies, the same number of observations and a common grid point were used for each of the selected Chl-*a* product to compute the monthly climatology. As a result, any biases and errors caused by missing data were consistent among different Chl-*a* products, and therefore the minimal effect of missing data was achieved. In addition, monthly anomalies were calculated for further analysis. Monthly anomalies were calculated by subtracting the monthly climatology from the corresponding monthly time-series datasets of each grid point for selected sensors during the study period. After that, the monthly Chl-*a* time-series and anomalies were transformed in Log10 bases (here after will be shown as Log10(Chl-*a*)) to fully cover the log-normal distribution of these datasets.

2.3. Statistical analysis

The Pearson correlation coefficient (r), as the most known index for correlation of variables, was used in this study. Pearson correlation coefficient assumes that the variables are normally distributed and a linear relationship exists between them. Based on the probability of the correlation between variables, the significance of each correlation (p) was calculated.

The linear regression type-1 was selected to calculate the trend of Chl-*a* datasets of each satellite sensor product. The type-1 linear regression was selected because: (a) it has been widely used for detection of

Chl-*a* trends [39], (b) comparison of log-transformed Chl-*a* anomalies and time-series are well recognized than those observed by complex trend detection methods [3], and (c) we are going to test whether trends between different sensor products provide an insight to the correlation between them, and we do not looking for the exact trends in the datasets. Trends in Chl-*a* time-series and anomalies data is computed as:

$$Y = XS + I \quad (1)$$

where 'Y' is the log-transformed anomaly, 'X' is time in year, 'S' is the slope of regression, and 'I' is the intercept. In this equation, 'S' defines the trend, and it is shown only when the Pearson correlation coefficient (r) was statistically significant ($p<0.05$).

In this study, we used the Z-test to identify whether two correlation coefficients are statistically different [40]. The score of a known r-value for two separate correlations is determined as bellow:

$$Z_n = 0.5log\left(\frac{1+r_n}{1-r_n}\right) \quad (2)$$

where Z_n is the score of each r-value. The overall Z_{score} is computed as bellow (Cohen and Cohen, 1983):

$$Z_{score} = \frac{Z_n - Z_{n+1}}{\{[1/(m_n-3)] + [1/(m_{n+1}-3)]\}^{1/2}} \quad (3)$$

where Z_{score} is then converted into the p-value assuming normal distribution of target datasets. A two-tailed test was performed to estimate accurate p-values. If $p<0.05$ the r-values are considered to be statistically significant and different, otherwise they deemed to be similar.

3. Results

3.1. Comparison of the standard Chl-a products (Comparison-I)

Correlation coefficient (r) between standard monthly Chl-*a* time-series from different satellite sensors are shown in Fig. 1. Over the most of the study area, the Chl-a time-series of the different satellite sensors show a high correlation (>0.85). The significance of correlations between different satellite sensors shows that the correlation between MODIS-SO and VIIRS-SO differs from the other pairs. Correlation between pairs of the Comparison-I, except the MODIS-SO vs. VIIRS-So, show that the 49-64% of the study area are very highly correlated ($p<0.0001$), 76-83% are highly correlated ($p<0.01$), 84-89% are significantly correlated ($p<0.05$), and 11-15% are not significant (Fig. 1 e-f) (Table 2). Correlation between MODIS-SO and VIIRS-SO shows that the only 9% of the study area are very highly correlated, 24% are highly correlated, 37% are significantly correlated, and 63% are not significantly correlated (Fig. 2h). The most important reason for this observation rises from the missing data over the study area between MODIS-SO and VIIRS-SO during the 2012-2020. The significantly correlated areas ($p<0.05$) are remarkably similar and the middle parts of the Persian Gulf show greatest r-values relative to the shallow regions. It is suggested that the shallow regions are affected by noises when compared with deeper regions.

Fig. 2a-d shows the r-values between monthly Chl-*a* anomalies from different ocean color sensors. The anomalies of Chl-*a* time-series represent the removed seasonal cycles from original data. After removing the seasonal cycles from Chl-*a* time-series, the correlations between sensors are not as high as the time-series in Fig. 1. It has been shown that the main fluctuation of Chl-*a* in the Persian Gulf is due to seasonal cycles. Hence, the large part of the total variance of Chl-*a* time-series is expected to be due to the seasonality, and the Chl-a anomalies reveal the interannual fluctuations of Chl-*a*. Nonetheless, over the most regions of the study area, Chl-*a* anomalies between different satellite sensors are highly correlated (>0.85), except the correlation between MODIS-SO vs. VIIRS-SO that shows r-values of 64-76%. The statistical significance of these correlations are considerably lower than those observed in Fig. 1e-h, with 63-69% of the total study area having significant correlation ($p<0.05$). Correlation between MODIS-SO and VIIRS-SO shows the lowest very high significant (4%), and about 65% percent of this correlation is insignificant (Table 2).

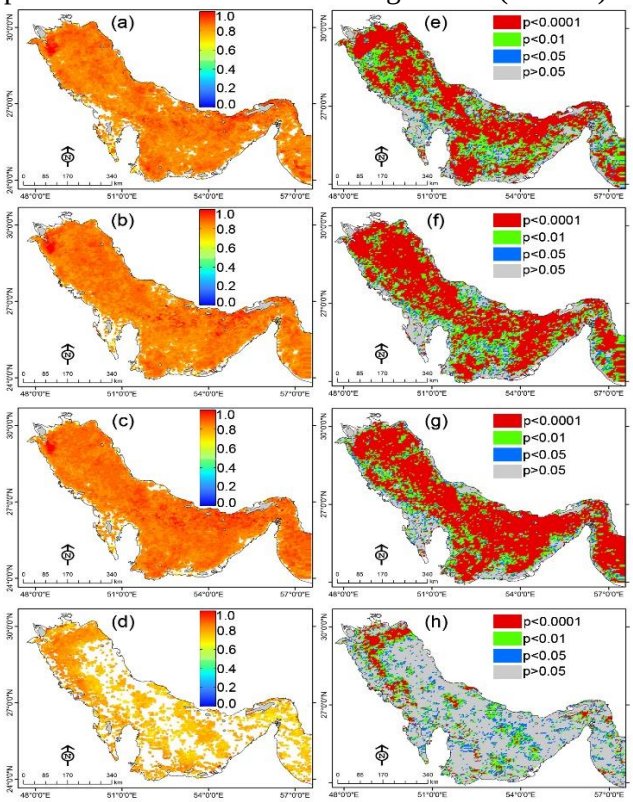

Figure 1. Maps of the correlation coefficient (r) between the monthly Chl-a time-series from different satellite sensors, Comparison-I. (a) MODIS-SO vs. MERIS-SO, (b) MODIS-SO vs. SeaWiFS-SO, (c) SeaWiFS-SO vs. MERIS-SO, (d) MODIS-SO vs. VIIRS-SO. (e)-(h) maps show the statistical significance (p) of the correlations of (a)-(d), respectively.

Table 2- Percentage area of the study area with significant (p<0.05), and not significant (p>0.05) correlations of the different comparisons denoted in table 1.

	Comparison	Chl-*a* time-series				Chl-*a* anomalies			
		p<0.0001	p<0.01	p<0.05	p≥0.05	p<0.0001	p<0.01	p<0.05	p≥0.05
I	MODIS-SO & MERIS-SO	49	76	84	15	24	49	63	37
	MODIS-SO & SeaWiFS-SO	57	81	87	12	25	52	66	34
	MERIS-SO & SeaWiFS-SO	64	83	89	11	26	55	69	30
	MODIS-SO & VIIRRS-SO	09	24	37	63	04	17	34	65
II	MODOS-SG & MODIS-SI	37	52	61	40	27	40	50	49
	MODIS-SG & MODIS-SO	12	25	34	65	06	16	25	75
	MODIS-SO & MODIS-SI	20	46	61	39	06	17	27	73
III	MERIS-SO & MODIS-SG	06	16	25	75	04	09	16	84
	MERIS-SO & SeaWiFS-SI	60	81	88	12	31	53	67	33
	MODIS-SG & SeaWiFS-SI	07	18	27	73	05	12	20	80
IV	MODIS-SO & MERIS-PO	04	12	21	79	03	07	13	87
	SeaWiFS-SO & MERIS-PO	06	13	22	77	05	11	18	82
	MERIS-SO & MERIS-PO	06	16	26	74	05	12	21	79

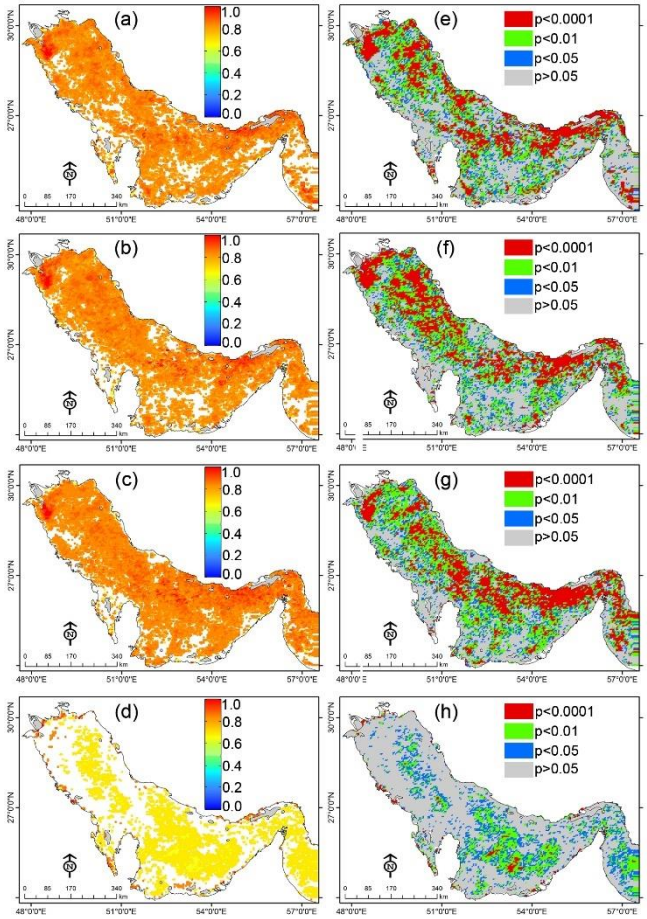

Figure 2- Maps of the correlation coefficient (r) between the monthly Chl-a anomalies from different satellite sensors, Comparison-I. (a) MODIS-SO vs. MERIS-SO, (b) MODIS-SO vs. SeaWiFS-SO, (c) SeaWiFS-SO vs. MERIS-SO, (d) MODIS-SO vs. VIIRS-SO. (e)-(h) maps show the statistical significance (p) of the correlations of (a)-(d), respectively.

3.2. Comparison of different Chl-a retrieval algorithms from a single sensor (Comparison-II)

Fig. 3 shows the correlation coefficient (r) and statistical significance (p) between Chl-*a* time-series from different Chl-*a* retrieval algorithms of MODIS. Results revealed that the Chl-*a* time-series are well correlated (>0.78) between different retrieval algorithms, but the most areas show the imperfect significant correlations (Table 2). The correlation between MODIS-SG and MODIS-SO shows the lowest significant values and less than 12% of the study area are very well correlated, and about 65% are not significantly correlated. The imperfect correlations are seen in the central parts and deeper regions where lower values of Chl-*a* are observed. Further, there are lower correlation (>0.70) in the Chl-*a* anomalies between different MODID data (Fig. 4). The Chl-*a* anomalies show the lowest correlation (~0.7) between MODIS-SO and MODIS-SI in the central parts of the Persian Gulf (Fig. 4c). The Chl-*a* anomalies show more correlations between different MODIS products in the shallow areas where p-values are significant. Despite the high correlation values of different Chl-*a* anomalies (>0.7) in the shallow areas of the study area, the majority of areas of the Persian Gulf do not show a significant correlation (p≥0.05) (Fig. 4d-f). This is mainly due to the gap of data between different Chl-*a* retrieval algorithms from MODIS data. Correlation coefficient (r-value) and probability maps (p-value) between monthly Chl-*a* time-series and anomalies from MODIS (Fig. 3a, c and 4a, c) revealed that the MODIS-SG vs. MODIS-SI shows the highest and the most significant correlation relative to the other sensor pairs proposed for Comparison-II. The worst case of comparison between Chl-*a* anomalies in Comparison-II belongs to the MODIS-SG vs. MODIS-SO pairs. Consequently, original time-series and removed seasonal cycles of Chl-*a* datasets using GSM and OCI retrieval algorithms agree perfectly in shallow high Chl-*a* waters (Fig. 4a) as OCI algorithm reverts to GSM algorithm at Chl-*a* concentrations >0.3 mg m^{-3}. In contrast, OC3M algorithm (MODIS-SO) shows the lowest agreement with SGM algorithm in both shallow and deeper areas, which indicates that the GSM and OC3 algorithms are not suitable for Chl-*a* estimations over the Persian Gulf even in the deeper areas.

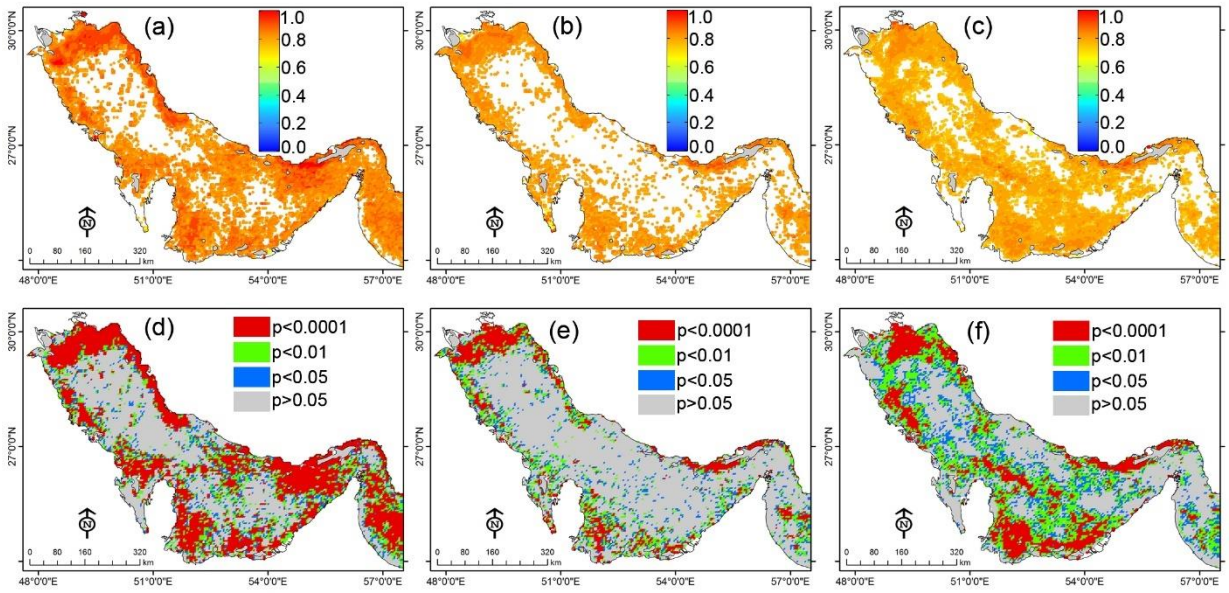

Figure 3. Maps of the correlation coefficient (r) between the monthly Chl-a time-series from MODIS using different Chl-a retrieval algorithms, Comparison-II. (a) MODIS-SG vs. MODIS-SI, (b) MODIS-SG vs. MODIS-SO, (c) MODIS-SO vs. MODIS-SI. (d)-(f) maps show the statistical significance (p) of the correlations of (a), (b), and (c), respectively.

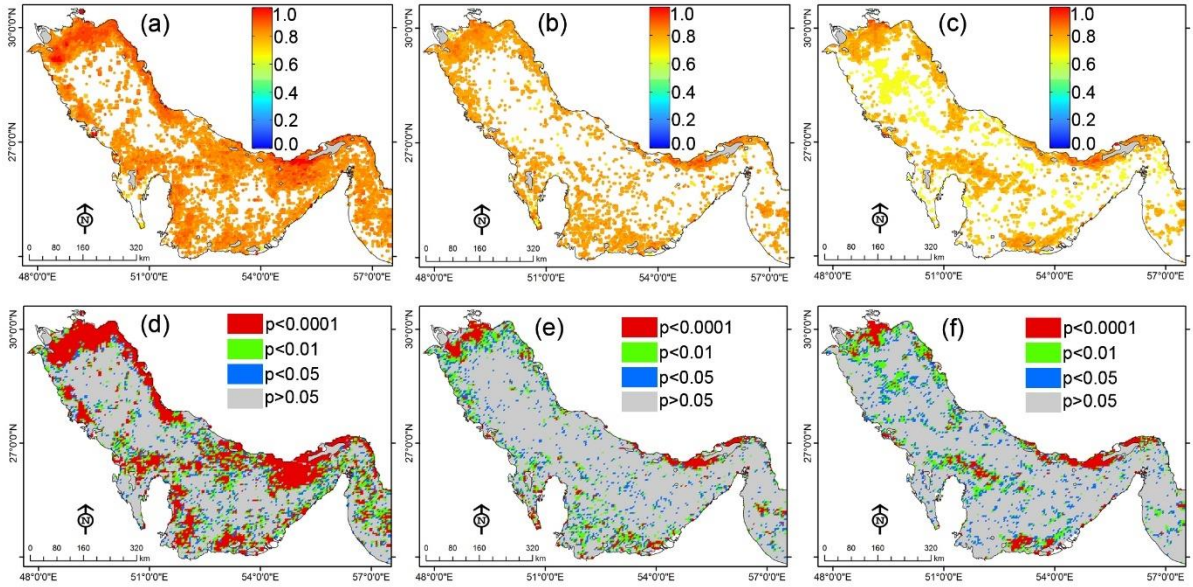

Figure 4. Maps of the correlation coefficient (r) between the monthly Chl-a anomalies from MODIS using different Chl-a retrieval algorithms, Comparison-II. (a) MODIS-SG vs. MODIS-SI, (b) MODIS-SG vs. MODIS-SO, (c) MODIS-SO vs. MODIS-SI. (d)-(f) maps show the statistical significance (p) of the correlations of (a), (b), and (c), respectively.

3.3. Comparison of different Chl-a retrieval algorithms from different sensors (Comparison-III)

Maps of the correlation coefficient (r) between monthly Chl-*a* time-series from different satellite sensors using different Chl-*a* retrieval algorithms are shown in Fig. 5. Only the results of Fig. 5b is consistent with Fig. 1, which indicates the correlations between MERIS-SO and SeaWiFS-SI are consistent with MERIS-SO and SeaWiFS-SO products. About 88% of the study area are significantly correlated for MERIS-SO vs. SeaWiFS-SI, and the other pairs of comparisons in *Comparison-III* scenario show less than 30% are significantly correlated over the shallow areas (Table 2). In addition, Fig. 4 indicates the influence of inter-sensor differences on the correlation maps and shows that the r-values and p-values between MERIS and SeaWiFS are higher than the other pairs over the whole Persian Gulf. Fig. 6 shows correlation coefficient maps between Chl-*a* anomalies from different satellite sensors using different Chl-*a* retrieval algorithms. It is consistent with Fig. 5 and indicates that the Chl-*a* anomalies between MERIS-SO and SeaWiFS-SI are significantly correlated for 67% of the whole study area (Fig. 6b, e).

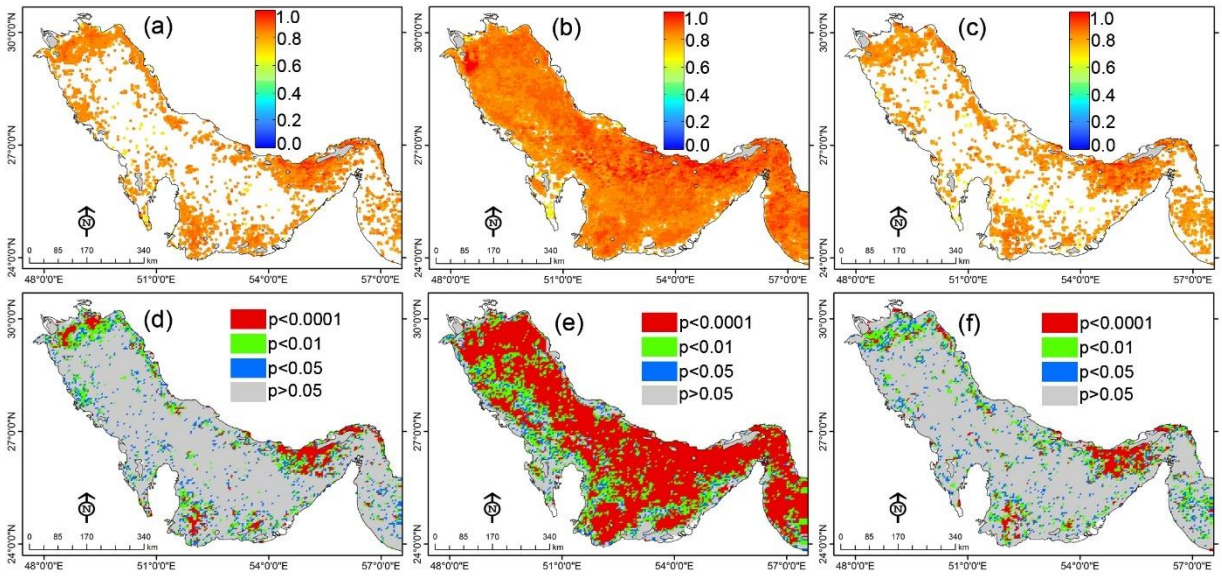

Figure 5. Maps of the correlation coefficient (r) between the monthly Chl-a time-series from different satellite sensors using different Chl-a retrieval algorithms, Comparison-III. (a) MERIS-SO vs. MODIS-SG, (b) MERIS-SO vs. SeaWiFS-SI, and (c) MODIS-SG vs. SeaWiFS-SI. (d)-(f) maps show the statistical significance (p) of the correlations of (a), (b), and (c), respectively.

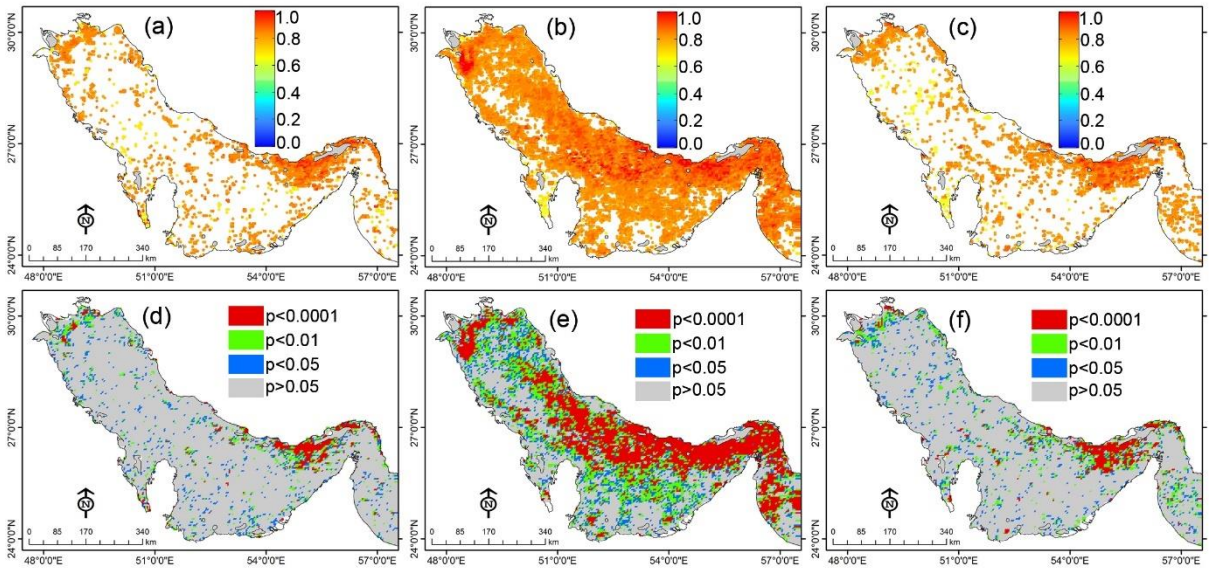

Figure 6. Maps of the correlation coefficient (r) between the monthly Chl-a anomalies from different satellite sensors using different Chl-a retrieval algorithms, Comparison-III. (a) MERIS-SO vs. MODIS-SG, (b) MERIS-SO vs. SeaWiFS-SI, and (c) MODIS-SG vs. SeaWiFS-SI. (d)-(f) maps show the statistical significance (p) of the correlations of (a), (b), and (c), respectively.

when compared with Chl-*a* retrieval algorithms from the same sensor (Fig. 3), the r-values are lower than for a single sensor, indicating the discrepancies of inter-sensor Chl-*a* estimations. However, the correlation coefficients for GSM and OC3/OC4 algorithms (<0.88) are less than the corresponding values of the OCI (>0.9) algorithm. Nonetheless, correlation maps of the *Comparison-III* scenario indicate the consistency in the Chl-*a* time-series and anomalies irrespective of the choice in Chl-*a* retrieval algorithms, although the most of the study area (75-84%) for GSM and OC3/OC4 algorithms are not significantly correlated.

3.4. Comparison of different atmospheric correction algorithms (Comparison-IV)

The maps of the correlation coefficient (r) between the monthly Chl-*a* time-series from different satellite sensors (MERIS, MODIS, and SeaWiFS) using two different atmospheric correction algorithms (SeaDAS and POLYMER) are shown in Fig. 7. The Chl-*a* time-series are significantly for 21-26% of the whole study area (Table 2), and most of the study area (74-79%) show insignificant correlations. However, the r-values from different satellite sensors in *Comparison-IV* varies from 0.82-0.97 (Fig. 7a-c). Fig. 8 shows maps of the correlation coefficient (r) between monthly Chl-*a*

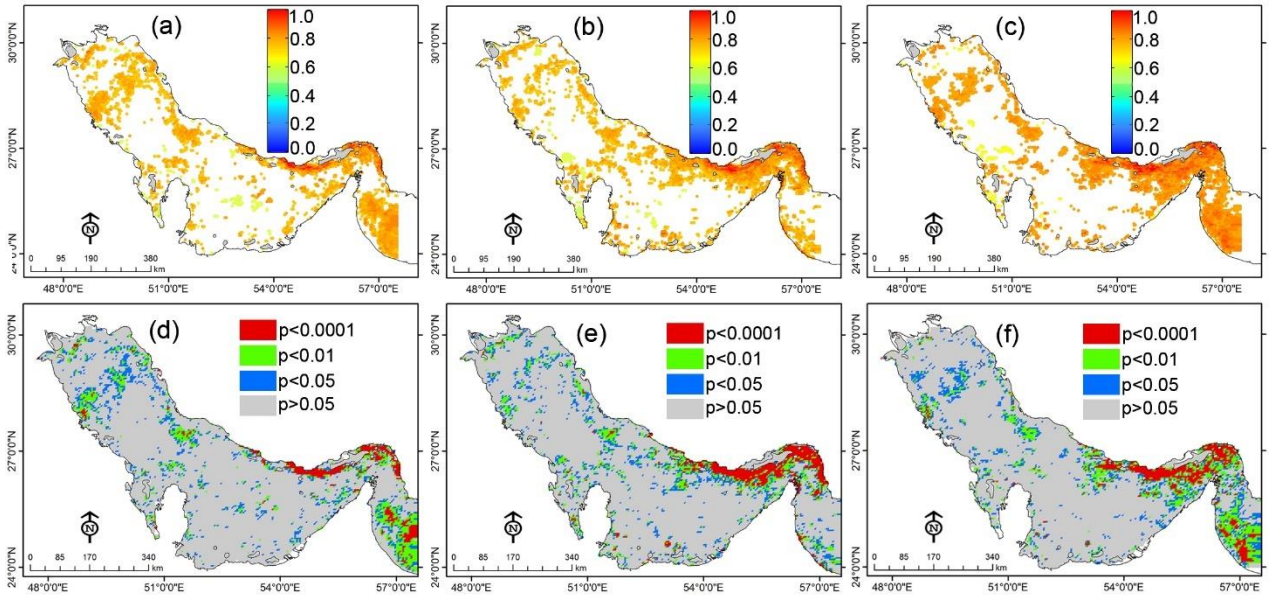

Figure 7. Maps of the correlation coefficient (r) between the monthly Chl-a time-series from different satellite sensors using different atmospheric correction algorithms, Comparison-IV. (a) MODIS-SO vs. MMERIS-PO, (b) MERIS-SO vs. MERIS-PO, and (c) SeaWiFS-SO vs. MERIS-PO. (d)-(f) maps show the statistical significance (p) of the correlations of (a), (b), and (c), respectively.

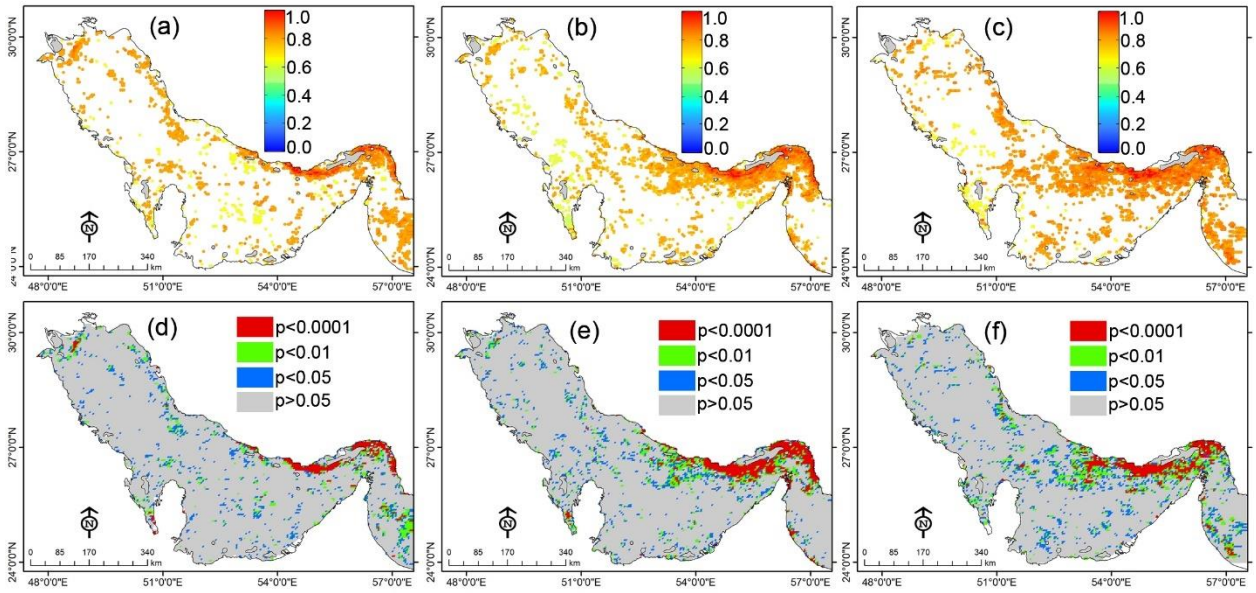

Figure 8. Maps of the correlation coefficient (r) between the monthly Chl-a anomalies from different satellite sensors using different atmospheric correction algorithms, Comparison-IV. (a) MODIS-SO vs. MMERIS-PO, (b) MERIS-SO vs. MERIS-PO, and (c) SeaWiFS-SO vs. MERIS-PO. (d)-(f) maps show the statistical significance (p) of the correlations of (a), (b), and (c), respectively.

anomalies for the pairs of *Comparison-IV* scenario where 79-87% of the study area show imperfect correlations (Table 2). Results are consistent with those obtained between GSM and OC3/OC4 Chl-*a* retrieval algorithms (Fig. 5, 6).

Results of the comparison between MODIS-SO and MERIS-PO, and the comparison between SeaWiFS-SO and MERIS-PO show the effect of both different atmospheric correction algorithms and different sensors, whereas comparison between MERIS-PO and MERIS-SO are just influenced by different atmospheric correction algorithms. The correlations between MERIS-PO and MERIS-SO are generally greater in northern coastal regions and they are slightly lower in the middle and southern regions (<0.74). In general, results of the Comparison-IV scenario (Fig. 7 and 8) indicate that the consistency of the Chl-*a* time-series and anomalies between different satellite sensors irrespective of the choice of atmospheric correction algorithms are imperfect over more than 70% of the Persian Gulf. Therefore, it could be concluded that the SeaDAS and POLYMER algorithms are not significantly correlated over the Persian Gulf.

4. Discussion

The Chl-*a* time-series for SeaWiFS, MERIS, and MODIS, are significantly correlated for >84% of the whole Persian Gulf (Table 2). Also, it was found that MODIS and VIIRS are correlated (~0.9) over the 37% of the study area, and the reminders are imperfectly correlated (Fig. 1). Furthermore, correlations between anomalies of the Chl-*a* from different satellite sensors are consistent with those obtained form Chl-*a* time series, although the spatial extent of prefect correlations are lower than Chl-*a* time-series (Fig. 2). It is encouraging to see such consistency in the Chl-a datasets from different satellite sensors despite of differences in design, wavelengths, overpass time, and pre- and post-lunch calibration instrument characteristics of each sensor. An irregular temporal sampling of ocean color satellite sensors produces biases in the monthly Chl-*a* series which is observable in the regional interannual variabilities. In addition, missing data and gaps in ocean color datasets may increase the inconsistency between different satellite sensors. The correlation between Chl-*a* from different satellite sensors appears reasonably sensitive to the Chl-*a* retrieval algorithms (Fig. 4-6), and to the atmospheric correction algorithms (Fig. 7 and 8). In this regard, SeaDAS and POLYMER atmospheric correction algorithms are highly consistent and no more significant differences were observed. In contrast, OC3/OC4 and OCI of Chl-*a* retrieval algorithms show very different results over the study area, where OCI showed more consistent results than OC3/OC4 algorithms for all of the selected satellite sensors. The analysis of the Chl-*a* anomalies showed similar results. The interannual consistency between different satellite sensors shows that the biases between sensors and algorithms are minimized. Also, it confirms the high stability and sensor calibration of the selected ocean color sensors.

It is clear from different satellite sensors that the differences of Chl-*a* raised mainly from different Chl-a retrieval algorithms (OC3/OC4, GSM, and OCI). However, along the middle and southern coastal regions, higher differences in Chl-*a* are observed when applying different atmospheric correction algorithms compared with different Chl-*a* retrieval algorithms. This finding indicates that the accurate atmospheric correction is clearly affects the Chl-*a* estimations from ocean color satellite sensors. Over the southern and middle of the Persian Gulf dust deposition and aerosol content raised from adjacent Sahara significantly influence the Chl-*a* estimation and emphasizes on the selection of an accurate atmospheric correction algorithm. Choosing the best atmospheric correction algorithm between POLYMER and SeaDAS for SeaWiFS, MERIS, and MODIS over the study area requires more investigation which is beyond the scope of this study.

Most of the ocean color satellites have life cycles of 5-10 years, and many of them have completed their mission (e.g. MERIS and SeaWiFS). Long-term detection of seasonal and interannual variations of Chl-*a* requires the combination of different ocean color missions which have overlapped to enable cross-calibration. The SeaWiFS, MERIS, and MODIS sensors have operated in parallel for 8 years, and MODIS and VIIRS are in orbit from 9 years ago. Hence, the results of this study provide an insight for merging of the selected satellite sensors for long-term analysis of Chl-*a*.

5. Conclusion

In this study, we used the monthly Chl-*a* time-series during the last 20-year period to evaluate the temporal consistency between four satellite sensors, SeaWiFS, MERIS, MODIS, and MODIS. Monthly anomalies of the Chl-*a* series were calculated for each satellite sensor over the study time period. Statistical analysis revealed that the Chl-*a* time-series and anomalies of three sensors were correlated for >84% and 63% of the study area, respectively. Chl-a series and anomalies from VIIRS showed to be correlated with MODIS over 37% and 34% of the study area. The consistency between different atmospheric correction and Chl-*a* retrieval algorithms from different sensors revealed that the accurate selection of Chl-*a* retrieval and atmospheric correction algorithms are very critical over the study area. The Chl-*a* time-series and anomalies showed consistency between GSM and OCI Chl-*a* retrieval algorithms in shallow regions where Chl-*a* concentrations are >0.3 mg m^{-3}. The OC3M and OC4 algorithms showed the lowest correlation with GSM algorithm in both shallow and deep regions of the Persian Gulf. The results indicated that the OC3/OC4 and GSM algorithms are not suitable for Chl-*a* estimations over the whole area of the study area, and in contrast the OCI algorithm provides more reasonable estimations of Chl-*a*. Furthermore, results revealed that the different atmospheric correction algorithms are reasonably influence the Chl-*a* estimations from different satellite sensors. In this regard, more than 70% of the study area showed an imperfect consistency between SeaDAS and POLYMER atmospheric correction algorithms. Consequently, performing the best atmospheric correction, and Chl-*a* retrieval algorithms are critical tasks in Chl-*a* estimations and applications in the Persian Gulf. The results also provide a decision for combining the ocean color satellite products for performing the long-term Chl-*a* datasets, while properly minimize the systematic differences between different satellite sensors.

Acknowledgment

This work has been supported by the Center for International Scientific Studies & Collaboration (CISSC), ministry of Science Research and

Technology. I express my gratitude to Dr. Masoud Sadreenasab, president of CISSC, for his kind cooperation.

6. References

[1] Saba VS, Friedrichs MAM, Antoine D, Armstrong RA, Asanuma I, Behrenfeld MJ, et al. (2011). An evaluation of ocean color model estimates of marine primary productivity in coastal and pelagic regions across the globe. *Biogeosciences*. 8(2):489–503.

[2] Gregg WW, Rousseaux CS. (2014). Decadal trends in global pelagic ocean chlorophyll: A new assessment integrating multiple satellites, in situ data, and models. *Journal of Geophysical Research C: Oceans*.119(9):5921–33.

[3] Brewin RJW, Sathyendranath S, Müller D, Brockmann C, Deschamps PY, Devred E, et al. (2015). The Ocean Colour Climate Change Initiative: III. A round-robin comparison on in-water bio-optical algorithms. *Remote Sensing of Environment*.162.

[4] Brickley PJ, Thomas AC. (2004). Satellite-measured seasonal and inter-annual chlorophyll variability in the Northeast Pacific and Coastal Gulf of Alaska. *Deep-Sea Research Part II: Topical Studies in Oceanography*.51(1–3):229–45.

[5] Kim W, Moon JE, Park Y, Ishizaka J. (2016). Evaluation of chlorophyll retrievals from Geostationary Ocean Color Imager (GOCI) for the North-East Asian region. *Remote Sensing of Environment*. 184:482–95.

[6] Song H, Long MC, Gaube P, Frenger I, Marshall J, McGillicuddy DJ. (2018). Seasonal Variation in the Correlation Between Anomalies of Sea Level and Chlorophyll in the Antarctic Circumpolar Current. *Geophysical Research Letters*. 45(10):5011–9.

[7] Mannino A, Novak MG, Nelson NB, Belz M, Berthon J-F, Blough N V., et al. (2019). Measurement protocol of absorption by chromophoric dissolved organic matter (CDOM) and other dissolved materials. IOCCG Ocean Optics and Biogeochemistry Protocols for Satellite Ocean Colour Sensor Validation. 1:1–77.

[8] Blauw AN, Benincà E, Laane RWPM, Greenwood N, Huisman J. (2018). Predictability and environmental drivers of chlorophyll fluctuations vary across different time scales and regions of the North Sea. *Progress in Oceanography*. 161:1–18.

[9] Sathyendranath S, Brewin RJ, Brockmann C, Brotas V, Calton B, Chuprin A, et al. (2019). An ocean-colour time series for use in climate studies: The experience of the ocean-colour climate change initiative (OC-CCI). *Sensors*. 19(19):4285.

[10] Allison DB, Stramski D, Mitchell BG. (2010). Seasonal and interannual variability of particulate organic carbon within the Southern Ocean from satellite ocean color observations. *Journal of Geophysical Research: Oceans*. 115(6).

[11] IOCCG. (2014). Phytoplankton functional types from Space. *Reports and Monographs of the International OceanColour Coordinating Group*. (15).

[12] Westberry TK, Schultz P, Behrenfeld MJ, Dunne JP, Hiscock MR, Maritorena S, et al. (2016). Annual cycles of phytoplankton biomass in the subarctic Atlantic and Pacific Ocean. *Global Biogeochemical Cycles*. 30(2):175–90.

[13] Friedland KD, Mouw CB, Asch RG, Ferreira ASA, Henson S, Hyde KJW, et al. (2018). Phenology and time series trends of the dominant seasonal phytoplankton bloom across global scales. *Global Ecology and Biogeography*. 1;27(5):551–69.

[14] Shang SL, Dong Q, Hu CM, Lin G, Li YH, Shang SP. (2014). On the consistency of MODIS chlorophyll-a products in the northern South China Sea. *Biogeosciences*. 11(2):269–80.

[15] Al-Naimi N, Raitsos DE, Ben-Hamadou R, Soliman Y. (2017). Evaluation of satellite retrievals of chlorophyll-a in the Arabian Gulf. *Remote Sensing*. 2017; 9(3).

[16] Moradi M, Kabiri K. (2015). Spatio-temporal variability of SST and Chlorophyll-a from MODIS data in the Persian Gulf. *Marine Pollution Bulletin*. 98(1–2):14–25.

[17] Swift SA, Bower AS. (2003). Formation and circulation of dense water in the Persian/Arabian Gulf. *Journal of Geophysical Research: Oceans*. 108(1).

[18] Vaughan GO, Al-Mansoori N, Burt JA. (2018). The arabian gulf. In: World Seas: An Environmental Evaluation Volume II: The Indian Ocean to the Pacific., 1–23.

[19] Paparella F, Xu C, Vaughan GO, Burt JA. (2019). Coral bleaching in the Persian/Arabian Gulf is modulated by summer winds. *Frontiers in Marine Science*. 6(1).

[20] Al-Yamani F, Naqvi SWA. (2019). Chemical oceanography of the Arabian Gulf. *Deep-Sea Research Part II: Topical Studies in Oceanography*. 161:72–80.

[21] Hunter JR. (1983). Aspects of the dynamics of the residual circulation of the Arabian Gulf. *Coastal Oceanography*. 31–42.

[22] Nezlin NP, Polikarpov IG, Al-Yamani F. (2007). Satellite-measured chlorophyll distribution in the Arabian Gulf: Spatial, seasonal and inter-annual variability. *International Journal of Oceans and Oceanography*. 2(1):139–56.

[23] Nezlin NP, Polikarpov IG, Al-Yamani FY, Subba Rao D V., Ignatov AM. (2010). Satellite monitoring of climatic factors regulating phytoplankton variability in the Arabian (Persian) Gulf. *Journal of Marine Systems*. 82(1–2):47–60.

[24] Ghanea M, Moradi M, Kabiri K. (2015). Investigation the behavior of MODIS ocean color products under the 2008 red tide in the eastern

Persian Gulf. In: International Archives of the Photogrammetry, *Remote Sensing and Spatial Information Sciences - ISPRS Archives*. p. 227–32.

[25] Fallahi, M., Torabi Azad, M., & Mansoury, D. (2021). A Hydrodynamic Model of Tidal Current in the Strait of Hormuz. *International Journal of Coastal and Offshore Engineering*, 5(1), 37-45.

[26] Moradi M, Moradi N. (2020). Correlation between concentrations of chlorophyll-a and satellite derived climatic factors in the Persian Gulf. *Marine Pollution Bulletin*. 161.

[27] Moradi, M. (2022). Inter-comparison of single-sensor and merged multi-sensor ocean color chlorophyll-a products in the shallow turbid waters-case study: Persian Gulf. *International Journal of Coastal and Offshore Engineering*, 7(2), 1-10.

[28] Werdell PJ, Franz BA, Bailey SW, Harding, Jr. LW, Feldman GC. (2007). Approach for the long-term spatial and temporal evaluation of ocean color satellite data products in a coastal environment. In: *Coastal Ocean Remote Sensing*. p. 66800G.

[29] Bailey SW, Werdell PJ. (2006). A multi-sensor approach for the on-orbit validation of ocean color satellite data products. *Remote Sensing of Environment*. 102(1–2):12–23.

[30] Hu C, Feng L, Lee Z. (2013). Uncertainties of SeaWiFS and MODIS remote sensing reflectance: Implications from clear water measurements. *Remote Sensing of Environment*. 133:168–82.

[31] Uitz J, Claustre H, Gentili B, Stramski D. (2010). Phytoplankton class-specific primary production in the world's oceans: Seasonal and interannual variability from satellite observations. *Global Biogeochemical Cycles*. 24(3).

[32] Vantrepotte V, Loisel H, Mlin F, Desailly D, Duforêt-Gaurier L. (2011). Global particulate matter pool temporal variability over the SeaWiFS period (1997-2007). *Geophysical Research Letters*. 38(2).

[33] Loisel H, Vantrepotte V, Ouillon S, Ngoc DD, Herrmann M, Tran V, et al. (2017). Assessment and analysis of the chlorophyll-a concentration variability over the Vietnamese coastal waters from the MERIS ocean color sensor (2002–2012). *Remote Sensing of Environment*. 190:217–32.

[34] Cui T, Zhang J, Tang J, Sathyendranath S, Groom S, Ma Y, et al. (2021). Assessment of satellite ocean color products of MERIS, MODIS and SeaWiFS along the East China Coast (in the Yellow Sea and East China Sea). *ISPRS Journal of Photogrammetry and Remote Sensing*. 87:137–51.

[35] Yu Z, Yang K, Luo Y, Shang C. (2020). Spatial-temporal process simulation and prediction of chlorophyll-a concentration in Dianchi Lake based on wavelet analysis and long-short term memory network. *Journal of Hydrology*. 582.

[36] Le C, Hu C, Cannizzaro J, Duan H. (2013). Long-term distribution patterns of remotely sensed water quality parameters in Chesapeake Bay. *Estuarine, Coastal and Shelf Science*. 128:93–103.

[37] Campbell JW. (1995). The lognormal distribution as a model for bio-optical variability in the sea. *Journal of Geophysical Research*. 100(C7).

[38] Greene CA, Thirumalai K, Kearney KA, Delgado JM, Schwanghart W, Wolfenbarger NS, et al. (2019). The Climate Data Toolbox for MATLAB. Geochemistry, Geophysics, *Geosystems*. 20(7):3774–81.

[39] Siegel DA, Behrenfeld MJ, Maritorena S, McClain CR, Antoine D, Bailey SW, et al. (2013). Regional to global assessments of phytoplankton dynamics from the SeaWiFS mission. *Remote Sensing of Environment*. 135:77–91.

[40] Cohen P, Cohen P, West SG, Aiken LS. (2014). Applied Multiple Regression/Correlation Analysis for the Behavioral Sciences. Applied Multiple Regression/Correlation Analysis for the Behavioral Sciences. *Psychology Press*.

INTERNATIONAL JOURNAL OF
COASTAL, OFFSHORE & ENVIRONMENTAL ENGINEERING IJCOE Vol.7/No. 3/Summer 2022 (31-42)

Available online at: www. Ijcoe.org

Spatial and temporal variations of the electrical conductivity and magnetic field of the Caspian Sea using Princeton Ocean Model

Sobhan Eskandari[1], Dariush Mansoury[2*]

[1] *Graduate of Physical Oceanography Department, Faculty of Natural Resources and Marine Sciences, Tarbiat Modares University; eskandarisobhan@modares.ac.ir*

[2*] *Assistant Professor, Physical Oceanography Department, Faculty of Natural Resources and Marine Sciences, Tarbiat Modares University; mansoury@modares.ac.ir*

ARTICLE INFO

Article History:
Received: 17 Jul. 2022
Accepted: 09 Oct. 2022

Keywords:
Magnetic field anomaly
Electrical conductivity
Electromagnetic induction
POM model
Caspian Sea

ABSTRACT

In this study, changes in the magnetic field and electrical conductivity across the Caspian Sea Basins were investigated using the Princeton Ocean Model (POM). In this model, bathymetry, temperature and salinity and atmospheric flux data were collected from GEBCO08, WOA and ECMWF databases, respectively. This model was implemented for ten years (2009-2019), and temperature, salinity and current velocity were extracted from the model output to calculate the electrical conductivity and simulate the magnetic field anomalies of the Caspian Sea. The calculated electrical conductivity indicates that the dominant factor in electrical conductivity was temperature. In the study area, the highest and lowest electrical conductivity were in the southern Caspian basin (SCB) with a value of 2.3 S/m in summer and in the northern Caspian basin (NCB) about 0.8 S/m in autumn. Also, the results show the highest and lowest magnetic fields in the SCB were 16 nT in March and 12 nT in November, respectively. The distribution of magnetic field anomalies with different values in the middle Caspian basin (MCB) can also be observed for all months. According to the results, the dominant factor in the magnetic field anomalies is the current velocity, which has the most effect on the magnetic field in the western part of the Caspian Sea.

1. Introduction

Electro-magnetic induction due to the flow of conducting seawater in the Earth's magnetic field has been a subject of research interest for many years [e.g.: 1, 2, 3, 4, 5, 6]. There has been a recent increase of research activities [e.g.: 7, 8, 9, 10, 11, 12, 13, 14, 15, 16, 17, 18]. The oceans play a special role in this induction due to their relatively high conductivity which leads to large lateral variability in surface conductance. The ocean-induced magnetic field is the smallest component of the Earth's magnetic field, and is five orders weaker than the Earth's magnetic field [18, 20]. These ocean magnetic signals are generated by sea interactions with the Earth's magnetic field. The magnetic field observed near the Earth's surface shows the interference of different magnetic field components [21]. The Earth's core field, known as the main field, generates more than 90% of the geomagnetic field measured at the Earth's surface. The Earth's magnetic field is generated by the movement of conductive material in the liquid part of the Earth's core, called Geodynamo, and refers to the core field. The Earth's surface magnetic field, generated by the Geodynamo core, resembles a dipole in the center of the Earth with a magnetic field ranging from 30,000 nT at the equator to more than 60,000 nT in the polar regions [22]. Another source of magnetic field is ocean dynamics. The oceans produce a magnetic field because the salty sea-water is a conductive fluid with a mean value between 3 to 4 S/m. Electrical signals detectable above the ground are due to seawater movement and ocean circulation caused by winds on the sea surface and differences in density due to changes in temperature and salinity. This combination of magnetic fields is the main subject of this research and is discussed in more detail. The studies show that the change in the electrical conductivity of seawater affects the characteristics of increasing and decreasing electromagnetic fields [23]. The electrical conductivity of the seawater in turn is mainly dependent on seawater temperature and salinity distribution [24]. which can be estimated using the Apel (1987) approximation [25], where temperature is

the dominant component [26]. The seawater electrical conductivity can be considered constant or variable with time; often variable electrical conductivity is considered instead of constant electrical conductivity distribution in the ocean [27]. As the oceans pass through the Earth's main magnetic field, the ionic content in the oceans generates electrical currents which flow across the world's oceans and produce magnetic fields called secondary magnetic fields. Electric currents that generate secondary fields are induced in the oceans by two different processes: (a) by time varying external magnetic fields, and (b) by the motion of the conducting ocean water through the Earth's main magnetic field [19]. An important question to be answered by such studies is whether the magnitude of the ocean induced magnetic field, (b), is sufficient for detection by present magnetometers. Magnetic field measurements at the ocean showed that this amount reached several nanotesla. In situ measurements at and below the ocean surface demonstrated that this magnitude reaches many tens of nanotesla [28]. Ocean eddies near Tasmania induce up to 25-nT magnetic fields at the sea surface. However, present numerical models predict much lower values. Stephenson and Bryan (1992) found the vertical component, bz, of the field at the sea surface to be of order 1 nT, while Tyler et al. (1997) and Vivier et al. (2004) reported field magnitudes within a few nanotesla. At the sea surface, in several spots south of Australia, at the satellite altitude its maximum value is 6 nT, also much larger than in the earlier studies. Similar calculations using ocean data products from the 1 °-resolution version of the ECCO-MIT model yield 20 nT as the maximum amplitude of the surface field, and 4 nT at 430 km [29]. Tyler et al. (1997) obtained the anomalies of the magnetic field in Antarctica and concluded that the changes in the magnetic field were about 2 nT at a depth of 20 m, 10 nT at a depth of 100 m, and up to several tens of nanotesla at lower depths. Researchers are interested in understanding the magnetic field produced by the ocean for a number of reasons. First, the ocean's magnetic field has become interesting for many oceanographers to study more about ocean currents. Secondly, the ocean's magnetic field is also relevant to geophysicists studying geological structures under the ocean [4]. However, the detection of the presented signals in satellite-based magnetometer measurements may be challenging today [30]. Nonetheless, the precision of the observations might improve with longer observation time series, by future processing improvements or through future magnetometer satellite missions. In addition, terrestrial magnetometers should be used. The expected changes at sea level (or ocean bottom) are of the order of several 0.1 nT and should be detectable by magnetometers on land, at ocean bottom, by deep sea telecommunication cables or in induction-based Tsunami early warning networks [31, 32, 33, 34]. The electrical conductivity of seawater samples on the southern shores of the Caspian Sea was measured at about 23 dS/m [35]. So far, no research has been done on the magnitude of the magnetic field in the Caspian Sea basins. In this research, for the first time, in a 0.08 °-resolution version of the POM model, oceanographic parameters such as temperature, salinity and current velocity were extracted and then they were used as inputs to study changes in magnetic field and electrical conductivity in the three Caspian basins. Tidal motions are not included in this analysis, because the tides in the Caspian Sea are negligible.

2. Methodology

2.1. Study area

The Caspian Sea is the largest lake in the world. All the features of the Caspian Sea, including size, depth, chemical properties, as well as circulation and thermohaline properties, classify it as a deep inland sea. In 2016, the average level of the Caspian Sea was measured to be -27.43 m against the surface of the Atlantic Ocean [36]. The Caspian Sea has a longitudinal geometry (1000 km long and 200 to 300 km wide) and has three northern, middle, and southern basins (Figure 1). The maximum depth in the northern basin is 20 m while the maximum depths in the middle and southern basins are 788 m and 1025 m, respectively [37]. Sea surface temperature in the NCB reaches below zero in winter and 25-26 °C in summer. In the southern Caspian basin (SCB), it occurs from 7-10 °C in winter to 25-29 °C in summer. The Caspian Sea has little salinity. In the deepest region, salinity changes reach about 12 psu to 13.5 psu [38, 39]. The elongated geometry and specific topography in the Caspian basins, acted upon by variable wind forcing and baroclinic effects result in spatially and temporally variable currents in the Caspian Sea. Despite strong variability of the sea currents, the general circulation has been described to be cyclonic. Especially standing out among these were the six instrumental surveys along the western coast of the MCB, carried out in the years 1935–1937 [40], showing predominantly southward currents along the western coast of the MCB, modified by wind-driven currents close to the surface [37, 41].

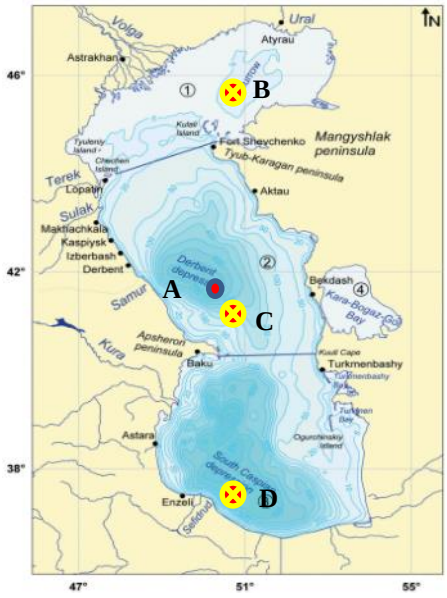

Figure 1. Caspian Sea [34]

2.2. Numerical system

The Princeton Ocean Model (POM) is a numerical ocean model on sigma coordinates, a right-angled curved horizontal grid, free surface boundary conditions, as well as turbulence and wave sub-models. It can be used for a wide range of issues such as circulation and mixing process in rivers, estuaries, continental shelf and slope, lakes, semi-closed and open oceans [42]. It uses the Mellor and Yamada (1982) turbulence closure scheme [43], while the horizontal viscosity terms are provided by the Smagorinsky (1993) parameterization [44]. Numerous applications of this model in the modeling field in oceans and seas have been studied in different parts of the world by many international researchers [45, 46, 47]. Message passing interface Princeton Ocean Model (mpiPOM) was developed by Advanced Taiwan Ocean prediction (ATOP) and is optimized for the needs and resources of the ATOP system [48]. It is desirable in terms of computer economy to separate vertically integrated equations (external mode) from vertical structure equations (internal mode). This technique, known as mode splitting [49], permits the calculation of the free surface elevation with little sacrifice in computational time by solving the velocity transport separately from the three-dimensional calculation of the velocity and thermodynamic properties. It generally uses the Smagorinsky diffusivity formula for horizontal diffusion [50]. The numerical technique for solving the temporal part of the equations is based on the mode separation method in which the external and internal modes equations are solved in two and three dimensions, respectively. In this study, the mpiPOM version is used for the Caspian Sea. The model domain is 36.40-47.50 °N and 46.50-55.00 °E with a horizontal resolution of 0.08 ° × 0.08 ° (in co-latitude and longitude) and 35 sigma levels. To apply the parallel processing (mpi), four cores were considered with the computational grid 68 × 52 (Eq. 1).

$$n_{proc} = [(im_{global} - 2)/(im_{local} - 2)] \times [(jm_{global} - 2)/(jm_{local} - 2)] \quad (1)$$

Where im_{global} = x-grid cells for modeled domain, jm_{global} = y-grid cells for modeled domain, im_{local} = x-grid cells for each processor, jm_{local} = y-grid cells for each processor, and n_{proc} =processors (i.e. num_of_nodes). The external time step is set to 5 s and the internal to 150 s. Surface fluxes use the 6-hourly atmospheric analyses from the European Centre for Medium-range Weather Forecast (ECMWF) at 0.125 °-resolution. The parameters used are 10 m winds, precipitation, evaporation, heat flux, and short and long wave radiation. Also, temperature and salinity data are used from World Ocean Atlas (WOA2005) at 1 °-resolution, and bathymetry data from General Bathymetric Chart of the Oceans (GEBCO08) at 0.5 °-resolution. The monthly average of Naval Research Laboratory (NRL) data was used for the data of the rivers (Volga, Kura and Ural) [51]. The model was run for 10 years from 2009 to 2019. After spinning up of 10 years, the model outputs were saved daily. In this study, we analyzed a year (2018) of model outputs. Salinity, temperature and current profiles have been extracted from model outputs. They were finally used to calculate the electrical conductivity into different layers of the Caspian Sea.

2.3. Stability and validation of the model

To check the stability of the model, salinity changes over time are shown in Figure 2a, which shows good stability after seven years of model implementation. To validate the output of the model, according to the measurement data available in 1996 [52], this model was implemented for ten years, from 1988 to 1997 [53]. Comparison of model output and in situ measurement data show that they are in good agreement. (Figure 2b). The comparison station is located at 41.5 °N and 50 °E (Figure 1_A).

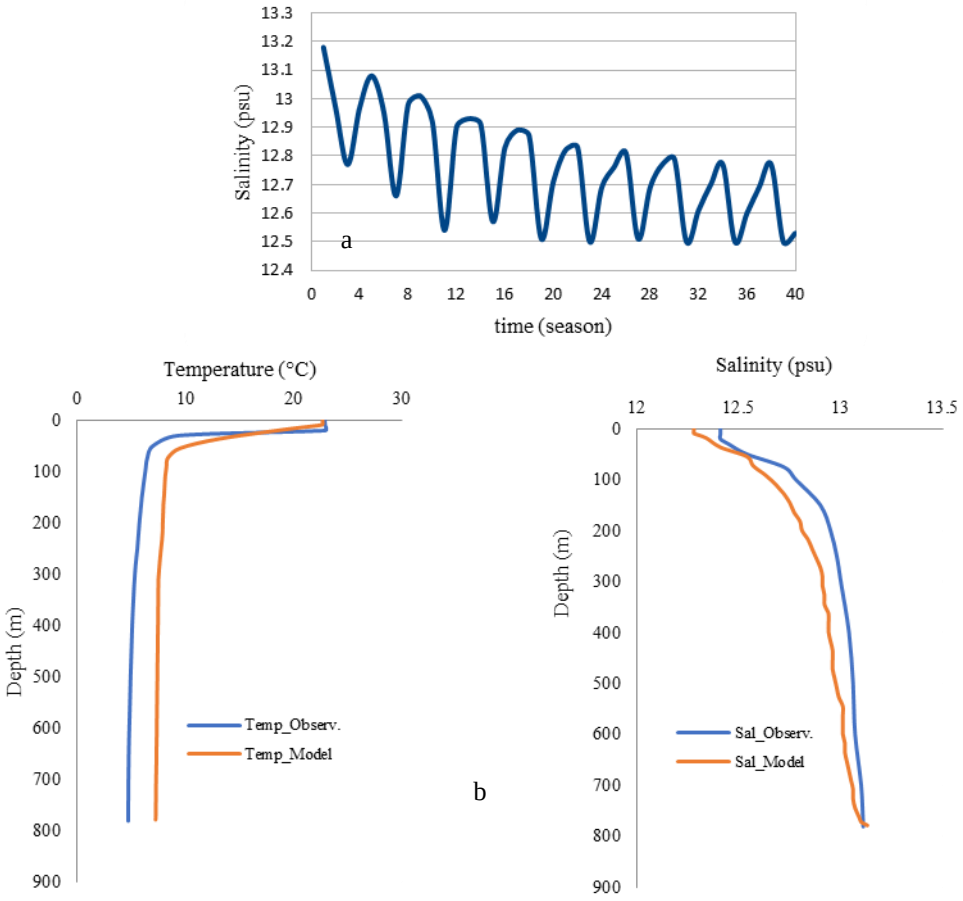

Figure 2. Stability (a) and validation (b) of the model

2.4. Electrical conductivity and Magnetic Field

To investigate the temporal and spatial distribution of electrical conductivity, using the salinity and temperature values extracted from the POM output, the electrical conductivity can be estimated using the method described by Apel (1987; Eqs. 2-5).

$$\sigma(T,s) = \sigma(25,s)\, exp(-\beta\Delta) \quad (2)$$

$$\Delta = 25 - T \quad (3)$$

$$\beta(\Delta,s) = 2.033\times10^{-2} - 1.266\times10^{-4}\Delta + 2.464\times10^{-6}\Delta^2 - s(1.849\times10^{-5} - 2.551\times0^{-7}\Delta + 2.551\times10^{-8}\Delta^2) \quad (4)$$

$$\sigma(25,s) = s(0.182521 - 1.46192\times10^{-3}s + 2.09324\times10^{-5}s^2 - 1.28205\times10^{-7}s^3) \quad (5)$$

Where σ is the conductivity of seawater.

The computation of electromagnetic induction is based on the equations of electromagnetic induction by Maxwell in 1865 for a moving medium.

a) Ampere's law $\nabla\times\vec{B} = \mu_0\vec{j}$ (6)

b) Maxwell- Faraday's law $\nabla\times\vec{E} = -\frac{\partial\vec{B}}{\partial t}$ (7)

c) Gauss's law $\nabla\cdot\vec{B} = 0$ (8)

Where $\vec{B}$ is the main magnetic field, $\vec{E}$ is the electric field, $\vec{j}$ is the electric current density, and μ_0 is the vacuum permeability coefficient. In addition, the generation of electric currents due to a moving conductor with the presence of electric and magnetic fields is described by Ohm's law.

$$\vec{j} = \sigma(\vec{E} + \vec{u}\times\vec{B}) \quad (9)$$

Where σ is the seawater electrical conductivity and $\vec{u}$ is the velocity of seawater. By applying the Ohm's law to the Maxwell-Faraday law, the equation (10) is obtained, and also, the general equation of electromagnetic induction (Eq. 11) is derived from the combination of the equations (6)-(10):

$$\nabla\times(\frac{\vec{j}}{\sigma} - \vec{u}\times\vec{B}) = -\frac{\partial\vec{B}}{\partial t} \quad (10)$$

$$\frac{1}{\mu_0}\nabla\times(\frac{1}{\sigma}\nabla\times\vec{B}) - \nabla\times(\vec{u}\times\vec{B}) = -\frac{\partial\vec{B}}{\partial t} \quad (11)$$

The maximum error for temperature for depths less than and more than 50 meters is about 5% and 12%, respectively, and also the maximum error for salinity is about 17% (at a depth of about 200 meters), but the average errors for temperature and salinity is less than 10%. As the comparison of the results show, there is a good agreement between the annual mean of the SST satellite image (Figure 3a) and the findings of the present study (Figure 3b).

2.5. Thin-Shell Approximation

The physical model which will be the basis of our calculations is that of a spherical shell whose outer radius is the surface of the oceans and whose inner radius corresponds to the maximum depth of the oceans.

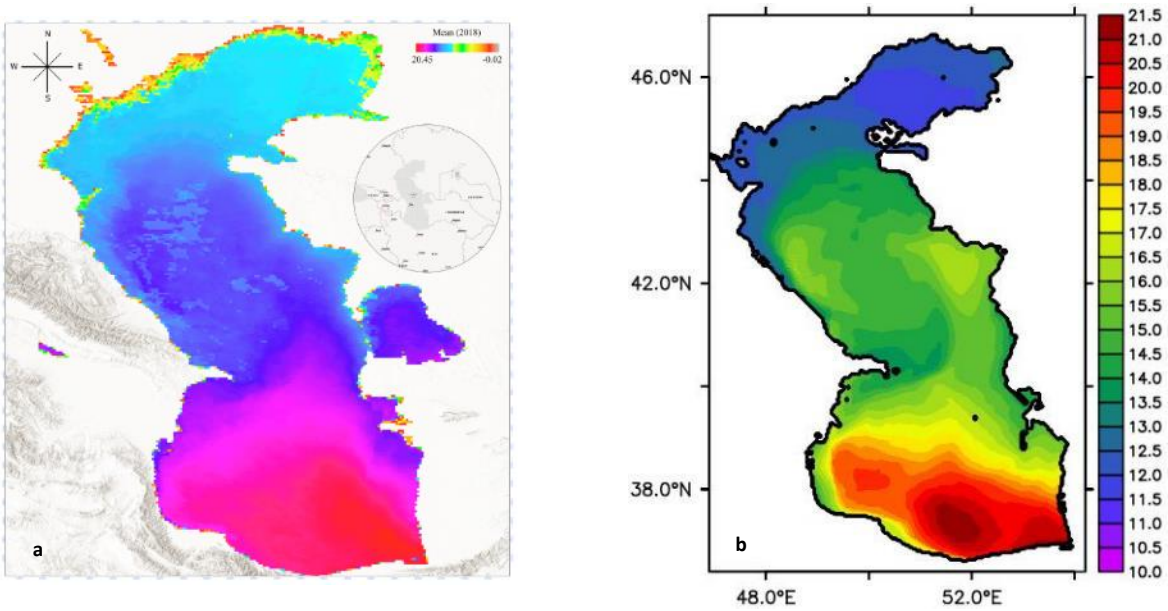

Figure 3. Annual mean climatic field of the SST (°C) a) Satellite image (https://oceancolor.gsfc.nasa.gov/) b) Model output in the Caspian Sea

Therefore, the atmosphere above the shell and the crust below the shell are perfect insulators, a good approximation known as a complete insulator [2]. The conductivity of seawater depends on both temperature and salinity and this may play a role in the variability of the oceanic magnetic and electric fields. The full magnetic field is divided into two parts (see Eq. 12), Earth's main magnetic field due to electric currents in the Earth's core ($\vec{F}$), of which only the radial component Fz is important, and the secondary magnetic field ($\vec{b}$) is the magnetic field induced by electric currents generated in the ocean's velocity [4, 29].

$$\vec{B} = \vec{F} + \vec{b} \tag{12}$$

It will not consider domains including the Earth's core so the source currents for $\vec{F}$ are zero in the region where (Eq. 11) is to be solved. Therefore:

$$\nabla \times \vec{F} = 0 \tag{13}$$

Assuming the environment is quasi-static, the electric field $\vec{E}$ can be written as a potential scalar gradient. The characteristic magnitude of the magnetic field at the sea surface is estimated as the equations (14, 15) [29]:

$$b = \mu_0 F_z S \tag{14}$$

$$S = \int_{-h}^{0} \sigma u_H dz \tag{15}$$

Where u_H is the horizontal velocity and S is the electric conductivity flux. In order to compute σ(z) and S we used vertical profiles of ocean current velocities observed at two locations and climatological data on ocean temperature and salinity.

2.6. IGRF Magnetic field model

The International Geomagnetic Reference Field (IGRF) is an established numerical model used to calculate the large scale, internal part of the Earth's magnetic field at times between 1900.0 A.D. and present, at locations on or above Earth's surface [54, 55, 56]. It is produced and maintained by a team of geomagnetic field modelers under the auspices of the International Association of Geomagnetism and Aeronomy (IAGA) Working Group V-MOD and is derived from observations collected by satellites, at magnetic observatories, and during magnetic surveys. It is used by scientists (e.g. in studies of space weather or in investigations of local magnetic anomalies) and also by commercial organizations and private individuals who often use the geomagnetic field as a source of orientation information. The IGRF model is reviewed every 5 years to be as accurate as possible [57]. To derive the radial component of the Earth's geomagnetic field, we used the IGRF magnetic field model. In this study, the IGRF model has been configured by a spatial resolution of 0.16˚ for 36.40-47.50 °N and 46.50-55.00 °E. The vertical geomagnetic component (F_z) data are extracted as the monthly mean for 2018.

3. Result and Discussion

3.1. Surface Electrical Conductivity

In this study, after spinning up of 10 years (2009-2019) and using the model outputs (temperature, salinity fields and currents), changes in magnetic field and electrical conductivity were studied in the Caspian Sea. The spatial and temporal distribution of electrical conductivity indicates that electrical conductivity has varied at different geographical locations.

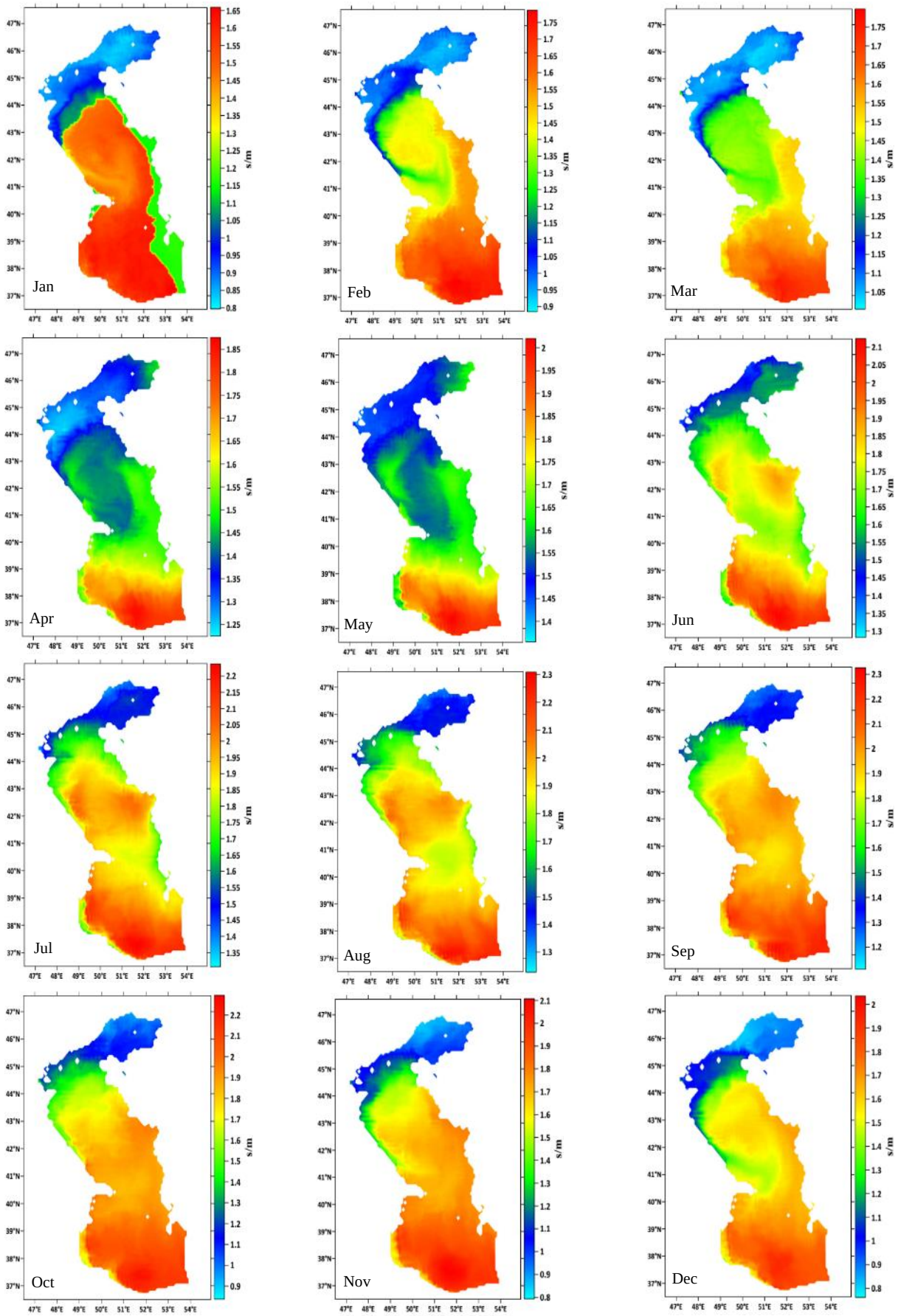

Figure 4. Monthly changes in electrical conductivity in the Caspian Sea

Figure 4 shows the monthly surface distribution of electrical conductivity in the Caspian Sea. In winter, the lowest electrical conductivity was observed in January with a value of 1.65 S/m and the highest electrical conductivity was observed in March with a value of more than 1.75 S/m. In

this season, the maximum electrical conductivity is in the SCB. In spring, the electrical conductivity increased compared to winter, with the electrical conductivity of 1.85 S/m and 1.2 S/m in April and June, respectively. The electrical conductivity changes in April and May were approximately similar in the middle and southern Caspian basins, but it increased in the MCB in June (Figure 4). In summer, due to increasing temperature, more electrical conduction changes are observed than in other seasons. In this season, the highest electrical conductivity (2.3 S/m) was observed in the SCB. In autumn, as shown in Figure 4, due to the decreasing temperature compared to summer, the electrical conductivity decreased in the NCB from 0.9 S/m in October to 0.8 S/m in November and December (Figure 4). Similarly, the electrical conductivity in the SCB also decreased according to the results, so that in December, the electrical conductivity reached 2 S/m.

3.2. Structure of vertical electric conductivity

For a more detailed study of the electrical conductivity, the vertical structure of the electrical conductivity from the sea surface to seabed was calculated for three positions B (45.79°*N*, 50.71°*E*; 7m depth), C (41.12°*N*, 50.71°*E*; 235m depth) and D (37.37°*N*, 50.71°*E*; 735m depth) (see Figure 1a) in February and July. The results of the analysis in the three basins show that in the SCB, there are relatively intense changes in electrical conductivity from the surface to a depth of 300 meters (Figure 5). In February, in this basin, the electrical conductivity and temperature decreased to a depth of about 70 meters (thermocline layer) and then it increased to a depth of 300 meters, due to the constant temperature and in proportion to the increasing changes in salinity, and from 300 m up to the seabed, similarities in temperature and salinity are almost unchanged. In July, the electrical conductivity and temperature decreased to a depth of about 100 meters (thermocline layer) and then is almost unchanged up to the seabed. As a result, electrical conductivity changes in the cold season are affected by changes in temperature and salinity, but in the hot season it is mainly affected by temperature changes.

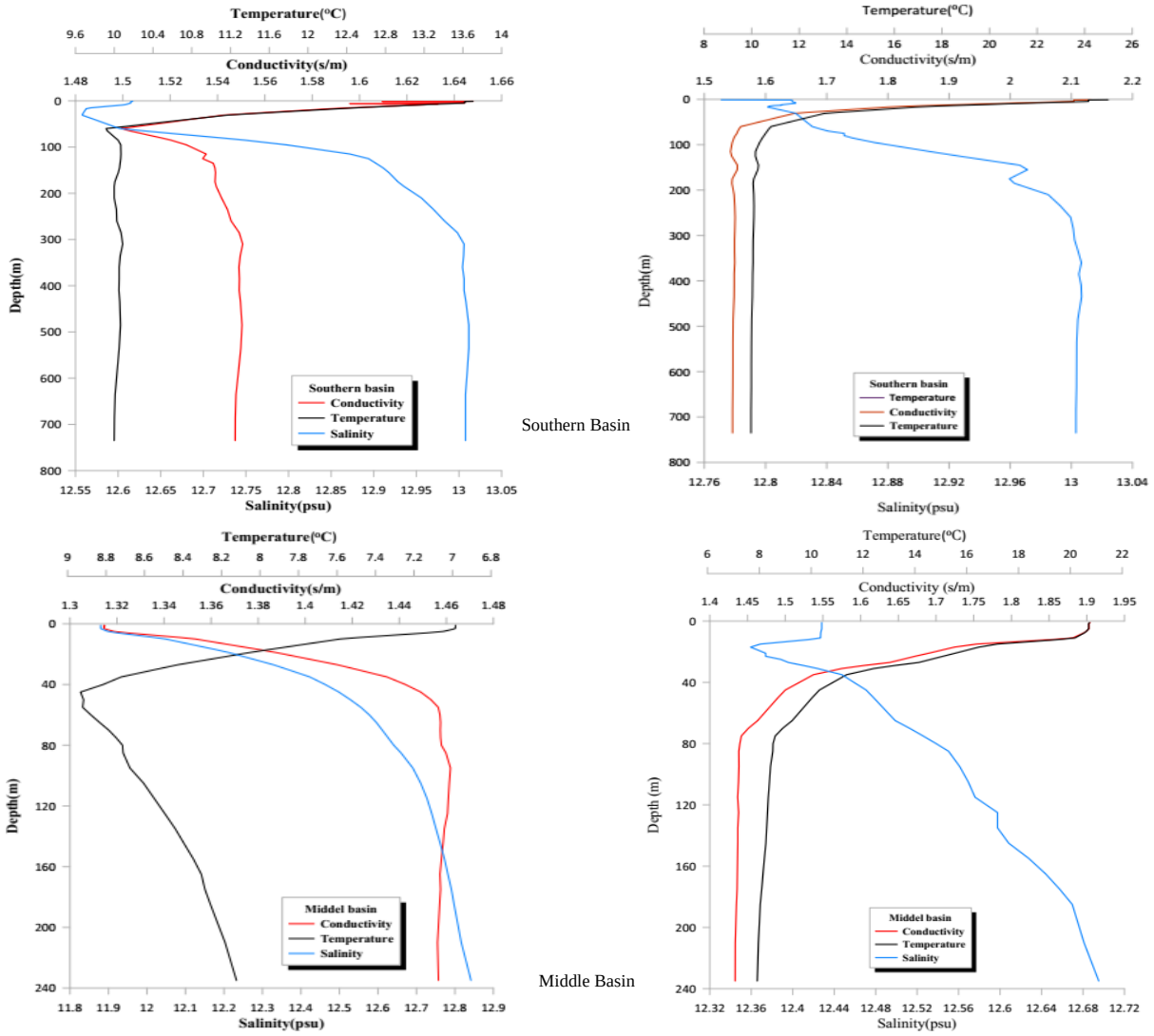

Figure 5. The electrical Conductivity, Temperature and Salinity Profiles in February (Left) and July (Right)

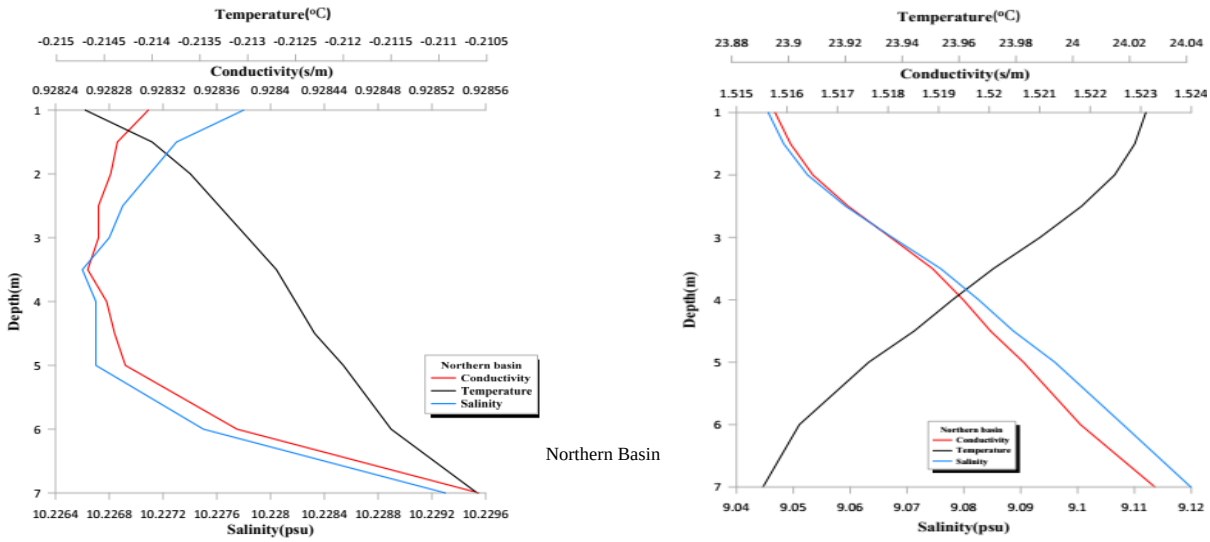

Figure 5. Continue

According to Figure 5. the electrical conductivity profiles in the MCB show that in February, electrical conductivity changes from the surface to the seabed are increasing due to small changes in temperature, according to the increasing changes in salinity. But in July, they are reduced due to large changes in temperature and according to the trend of temperature changes. Also, the dependence of electrical conductivity on salinity in the NCB is greater than temperature. In this basin, salinity changes are greater than temperature changes due to the Volga River and shallow water. As a result, the electrical conductivity has changed according to the trend of salinity changes. In February, electrical conductivity and salinity decreased to a depth of 3.5 meters and then increased with increasing depth to the seabed. In July, the electrical conductivity changes are increasing, according to the trend of salinity changes.

3.3. Monthly changes of magnetic field

According to equations (6)-(15), the monthly temporal and spatial changes of the magnetic field in the northern, central and southern Caspian basins for 2018 have been studied (Figure 6). The monthly changes of the magnetic field in most of the Caspian Sea are less than 1 nT (of the order of 0.1 nT). Its average value in some deep regions is about 3 and 6 nT in the middle and southern basins of the Caspian Sea, respectively. The highest magnetic field is in the SCB. The magnetic field anomaly in the Caspian Sea is more intense in the southern basin in winter. In spring, the magnetic field anomalies reduced compared to winter in the MCB and NCB. In the spring, magnetic field anomalies are reduced in the MCB and NCB compared to the winter. This decrease in magnetic field is more intense in MCB than in NCB. In summer, the magnitude of the magnetic field in the MCB was much lower than winter and spring, about 1 nT - 2 nT in August. In autumn, the magnetic field intensely increased in the MCB (about 5 nT. The results show that in all months the highest magnetic field anomaly occurred in the SCB, so that in March, a magnetic field of up to 16 nT was observed in the SCB.

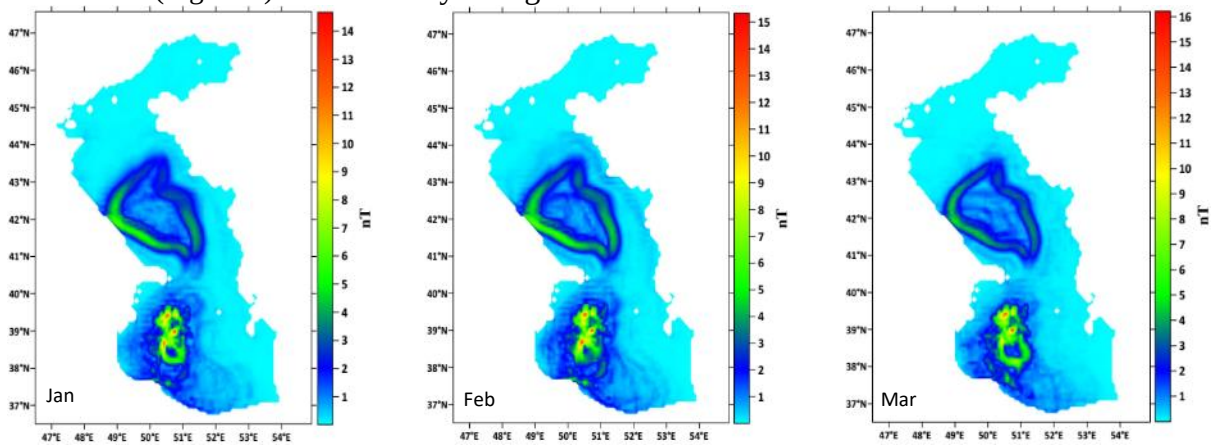

Figure 6. Monthly changes of Magnetic field in the Caspian Sea

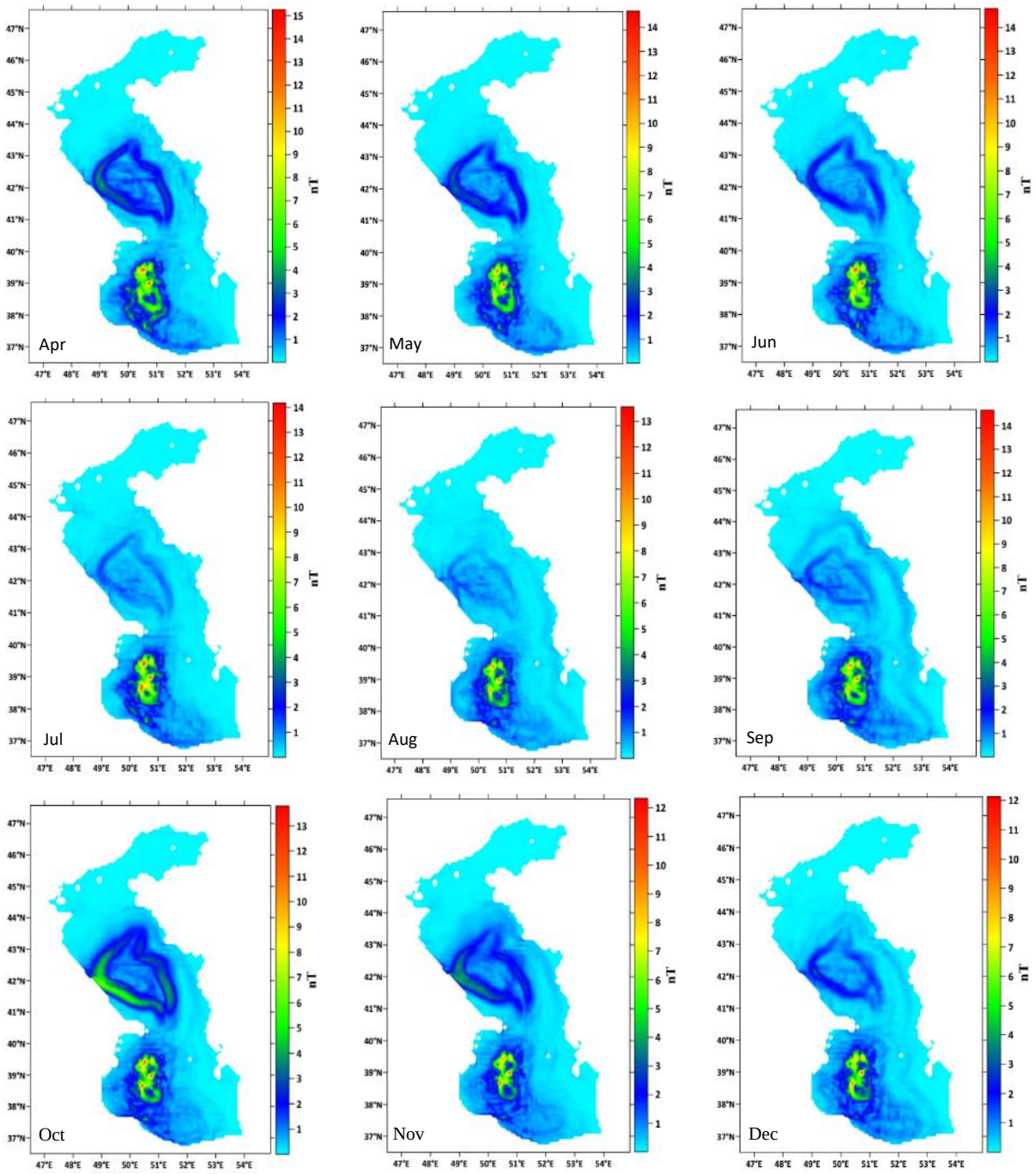

Figure 6. Continue

It shows the lowest magnitude of magnetic field anomalies in October and November with a value of approximately 12 nT in the SCB. But the highest magnetic field changes are observed in the MCB in all months. The magnetic field anomaly is a function of the electrical conductivity flux and current velocity. To calculate the magnetic field anomaly using the sum of layers of electrical conductivity flux $\int_{-h}^{0} \sigma u_H dz$ from surface $z = 0$ to depth $z = -h$, it can be concluded that the maximum magnetic field anomaly obtained in the Caspian Sea is a function of depth and sea current.

4. Conclusion

The Princeton Ocean Model was used to determine the parameters required to simulate magnetic fields in the Caspian Sea. This combination makes it unique to not only calculate the induced magnetic signals but also to evaluate the influence of oceanographic factors on the magnetic induction process. The electrical conductivity distribution of the SCB showed that the lowest and the highest of surface electrical conductivity were 1.65 S/m in January and 2.3 S/m in August and September, respectively. These findings were in good agreement with the values measured by Dordipour et al. (2004). In July and February, changes in electrical conductivity, in the SCB and MCB, are

proportional to temperature changes, while in the NCB, it is proportional to changes in salinity. The expected changes at sea level (or ocean bottom) are of the order of several 0.1 nT (Saynisch et al. 2016) which is in good agreement with the magnetic field changes in the NCB, due to the shallow depth. Also, the magnetic field anomalies in the southern and middle basins, due to the deep-water depth, are in relatively good agreement with the magnetic field changes in the Ocean (Glazman and Golubev, 2005; Tyler et al. 1997). The results show that the amount of magnetic field anomalies in the NCB was the lowest due to the shallow depth. The magnetic field anomalies are relatively intense in parts of the southern and middle basins. Spatial and temporal changes in the scattering of the magnetic field in the MCB compared to other basins show that the magnetic field anomaly has temporal and spatial variability and is affected by sea currents. In SCB, the highest and lowest magnetic field anomalies were observed in March 16 nT and November 12 nT, respectively. According to the results, the current velocity and depth are the most important factors in changing the magnetic field in the Caspian Sea, which has the most effect on the magnetic field in the western half of the Caspian Sea. The highest magnetic field anomalies in this study (16 nT) are in relatively good agreement with the magnetic field anomalies in South Australia (20 nT) as well as in parts of Antarctica (10 nT at 100 m depth) (Glazman and Golubev, 2005; Tyler et al. 1997). This discrepancy can be due to differences in the thermohaline structure, current velocity and also the vertical component of the Earth's magnetic field in each of the research areas.

5. Reference

[1] Larsen, J., 1992. Transport and heat flux of the Florida Current at 27 ̊N derived from cross-stream voltages and profiling data: Theory and observations, Philos. Trans. R. Soc. London, Ser. A, 338, 169– 236.

[2] Stephenson, D., Bryan, K., 1992. Large-scale electric and magnetic fields generated by the oceans. Journal of Geophysical Research, Vol, 97, no, C10, pp. 15467-15480.

[3] Chave, A.D., and Luther, D.S., 1990. Low-frequency, motionally induced electromagnetic fields in the ocean, J. Geophys. Res., 95, 7185– 7200.

[4] Tyler, R.H., Mysak, L.A., Oberhuber, J.M., 1997. Electromagnetic fields generated by a three-dimensional global ocean circulation. Journal of Geophysical Research: Oceans, Vol, 102, no, C3, pp. 5531-5551.

[5] Flosadottir, A.H., Larsen, J.C., and Smith, J.T., 1997a. Motional induction in North Atlantic circulation models, J. Geophys. Res., 102, 10,353 –10,372.

[6] Flosadottir, A.H., Larsen, J.C., and Smith, J.T., 1997b. The relation of seafloor voltages to ocean transports in North Atlantic circulation models: Model results and practical considerations for transport monitoring, J. Phys. Oceanogr., 27, 1547– 1565.

[7] Tyler, R.H., Maus, S., and Lu¨hr, H., 2003. Satellite observations of magnetic fields due to ocean tidal flow, Science, 299, 239– 240.

[8] Maus, S., and Kuvshinov, A., 2004. Ocean tidal signals in observatory and satellite magnetic measurements, Geophys. Res. Lett., 31, L15313, https://doi.org/10.1029/2004GL020090.

[9] Vivier, F., Maier-Reimer, E., and Tyler, R.H., 2004. Simulations of magnetic fields generated by the Antarctic Circumpolar Current at satellite altitude: Can geomagnetic measurements be used to monitor the flow? Geophys. Res. Lett., 31, L10306, https://doi.org/10.1029/2004GL019804.

[10] Manoj, C., Kuvshinov, A., Maus, S., and Lühr, H., 2006. Ocean circulation generated magnetic signals. Earth Planets Space, 58(4), 429-437.

[11] Khalilabadi, M.R., and Hassantabar, B.S.H., 2016. Investigation of magnetic field fluctuations due to sea waves in the Strait of Hormuz, Journal of Research on Applied Geophysics, 2(1), 23-34.

[12] Irrgang, C., Saynisch, J., and Thomas, M. 2017. Utilizing oceanic electromagnetic induction to constrain an ocean general circulation model: A data assimilation twin experiment. J. Adv. Model. Earth Syst., 9(3), 1703-1720. https://doi.org/10.1002/2017MS000951.

[13] Khalilabadi, M. R., and Shahmirzaee, H. 2017. Marine Magnetic Data Processing and Extracting Magnetic Anomaly. Hydrophysics, 3(1), 1-10.

[14] Irrgang, C., Saynisch-Wagner, J., Thomas, M, 2018. Depth of origin of ocean-circulation-induced magnetic signals. In Annales Geophysicae, Vol, 36, no, 1, pp. 167-180.

[15] Saynisch, J., Irrgang, C., and Thomas, M., 2018. On the Use of Satellite Altimetry to Detect Ocean Circulation's Magnetic Signals. J. Geophys. Res. Oceans, 123(3), 2305-2314. https://doi.org/10.1002/2017JC013742.

[16] Velímský, J., Šachl, L., Martinec, Z., 2019. The global toroidal magnetic field generated in the Earth's oceans. Earth and Planetary Science Letters, Vol, 509, pp. 47-54.

[17] Šachl, L., Martinec, Z., Velímský, J., Irrgang, C., Petereit, J., Saynisch, J., Schnepf, N.R., 2019. Modelling of electromagnetic signatures of global ocean circulation: physical approximations and numerical issues. Earth Planets Space, 71(1), 58. https://doi.org/10.1186/s40623-019-1033-7

[18] Khalilabadi, M.R. 2022. Underwater Terrain and Gravity aided inertial navigation based on

Kalman filter. International Journal of Coastal and Offshore Engineering, 5(3), 15-21.

[19] Kuvshinov, A. V., 2008. 3-D global induction in the oceans and solid Earth: recent progress in modeling magnetic and electric fields from sources of magnetospheric, ionospheric and oceanic origin. Surveys in Geophysics, Vol, 29, no, 2, pp. 139-186. https://doi.org/10.1007/s10712-008-9045-z

[20] Thébault, E., Finlay, C.C., Beggan, C.D., Alken, P., Aubert, J., Barrois, O., Bertrand, F., Bondar, T., Boness, A., Brocco, L., Canet, E., Chambodut, A., Chulliat, A., Coïsson, P., Civet, F., Du, A., Fournier, A., Fratter, I., Gillet, N., Hamilton, B., Hamoudi, M., Hulot, G., Jager, T., Korte, M., Kuang, W., Lalanne, X., Langlais, B., Léger, J.-M., Lesur, V., Lowes, F. J., Macmillan, S., Mandea, M., Manoj, C., Maus, S., Olsen, N., Petrov, V., Ridley, V., Rother, M., Sabaka, T. J., Saturnino, D., Schachtschneider, R., Sirol, O., Tangborn, A., Thomson, A., Tøffner-Clausen, L., Vigneron, P., Wardinski, I., and Zvereva, T., 2015. International Geomagnetic Reference Field: the 12th generation. Earth Planets Space, vol, 67, no, 1, pp. 79.

[21] Dostal, J., 2014. Modelling of the magnetic field induced by ocean circulation, Doctoral dissertation, Institut f¨ur Meteorologie Freie Universit¨at Berlin.

[22] Mandea, M., Thébault, E., 2007. The changing faces of the Earth's magnetic field: a glance at the magnetic lithospheric field, from local and regional scales to a planetary view. Published by Commission for the Geological Map of the World.

[23] Key, K., Constable, S., 2011. Coast effect distortion of marine magnetotelluric data: Insights from a pilot study offshore northeastern Japan. Physics of the Earth & Planetary Interiors, Vol, 184, no, 3-4, pp. 194-207.

[24] Fedorov, K., 2002. Formulas for converting the electrical conductivity of sea water into salinity with a digital temperature-salinity probe under average ocean conditions. Oceanology, 11(4), pp. 622-626.

[25] Apel, J. R., 1987. Principles of Ocean Physics, International Geophysics Series, Academic Press, San Diego, California, Vol. 38.

[26] Irrgang, C., Saynisch, J., Thomas, M., 2016. Impact of variable sea-water conductivity on motional induction simulated with an OGCM. Ocean Science Discussions, Vol, 12, no, 4, pp. 1869-1891.

[27] Thomas, M., Saynisch, J., Irrgang, C., 2016. Impact of variable sea-water conductivity on motional induction simulated with an OGCM. Ocean Science Discussions, Vol, 12, no, 4, pp. 1869-1891.

[28] Lilley, F.E., White, A., and Heinson, G.S., 2001. Earth's magnetic field: Ocean contributions to vertical profiles in deep oceans, Geophys. J. Int., 147, 163 – 175.

[29] Glazman, R. E., Golubev, Y. N, 2005. Variability of the ocean-induced magnetic field predicted at sea surface and at satellite altitudes. Journal of Geophysical Research: Oceans, Vol, 110, no, C12.

[30] Saynisch, J., Petereit, J., Irrgang, C., Kuvshinov, A., Tomas, M., 2016. Impact of climate variability on the tidal oceanic magnetic signal-A model based sensitivity study. Journal of Geophysical Research Oceans, Vol, 121, no, 8, pp. 5931-5941.

[31] Kuvshinov, A., Sabaka, T., and Olsen, N., 2006. 3-D electromagnetic induction studies using the Swarm constellation: Mapping conductivity anomalies in the Earth's mantle, Earth Planets Space, 58, 417– 427.

[32] Kuvshinov, A., and Utada, H., 2010. Anomaly of the geomagnetic Sq variation in Japan: effect from 3-D subterranean structure or the ocean effect? Geophys. J. Int. 183, 1239–1247.

[33] Schnepf, N. R., Kuvshinov, A., and Sabaka, T., 2015. Can we probe the conductivity of the lithosphere and upper mantle using satellite tidal magnetic signals? Geophys. Res. Lett., 42, 3233–3239, https://doi.org/10.1002/2015GL063540.

[34] Rabinovich, A.B., and Eblé, M.C., 2015. Deep-Ocean Measurements of Tsunami Waves. Pure Appl. Geophys. 172, 3281–3312 (2015). https://doi.org/10.1007/s00024-015-1058-1

[35] Dordipour, I., Ghadiri, H., Bybordi, M., Siadat, H., Malakouti, M. J., Hussein, J. 2004. The use of saline water from the Caspian Sea for irrigation and barley production in northern Iran. 13th International Soil Conservation Organisation Conference – Brisbane.

[36] Lebedev, S., 2018. Climatic variability of water circulation in the Caspian Sea based on satellite altimetry data. International journal of remote sensing, Vol, 39, no, 13, pp. 4343-4359.

[37] Ibrayev, R.A., Özsoy, E., Schrum, C., and Sur, H.I., 2010. Seasonal variability of the Caspian Sea three-dimensional circulation, sea level and air-sea interaction, Ocean Sci, *6*(1), 311-329. https://doi.org/10.5194/os-6-311-2010

[38] Zereshkian, S., and Mansoury, D., 2018. Evaluation of Offshore Wind Power to Supply the Electric Power Required for Offshore Oil and Gas Platforms in the Caspian Sea, Journal, of Hydrophysics, 4(1): 57-68.

[39] Zereshkian, S., and Mansoury, D., 2020. Evaluation of ocean thermal energy for supplying the electric power of offshore oil and gas platforms, Journal of the Earth and Space Physics,

Vol. 46, No. 2, 331-345. https://doi.org/10.22059/jesphys.2020.289441.1007161

[40] Baidin, S.S., Kosarev, A.N., 1986. The Caspian Sea. Hydrology and hydrochemistry, Moscow, Nauka, 261 pp (in Russian)

[41] Safari, M., Mansoury, D., & azarmsa, S. A. (2022). Grain-size characteristics of seafloor sediment and transport pattern in the Caspian Sea (Nowshahr and Babolsar coasts). International Journal of Coastal and Offshore Engineering, *7*(1), 34-42.

[42] Blumberg, A.F., and Mellor, G.L., 1987. A description of a three-dimensional coastal ocean circulation model. Three-Dimensional Coastal Ocean Models, Vol. 208, Heaps, N.S. (Ed.), American Geophysical Union, https://doi.org/10.1029/CO004p0001

[43] Mellor, G.L., Yamada, T., 1982. Development of a turbulence closure submodel for geophysical fluid problems. Rev. Geophys. Space Phys. 20, 851–875. https://doi.org/10.1029/RG020i004p00851

[44] Smagorinsky, J., 1993. In: Galperin, B., Orszag, S. (Eds.), 1993. Large Eddy Simulations of Complex Engineering and Geophysical Flows, Cambridge University Press.

[45] Korotenko, K., Mamedov, R., Kontar, A., and Korotenko, L., 2004. Particle tracking method in the approach for prediction of oil slick transport in the sea: modelling oil pollution resulting from river input, Journal of Marine Systems, vol. 48, p.159-170.

[46] Cherkesov, L.V., Shul'ga, T.Ya., 2018. Numerical Analysis of the Effect of Active Wind Speed and Direction on Circulation of Sea of Azov Water with and without Allowance for the Water Exchange through the Kerch Strait. Oceanology, 58, 19–27. DOI:10.1134/S0001437018010022

[47] Medvedev, I.P., Kulikov, E.A., and Fine, I.V., 2020. Numerical modelling of the Caspian Sea tides, Ocean Sci., 16, 209–219, https://doi.org/10.5194/os-16-209-2020.

[48] Oey, L., Chang, Y. L., Lin, Y. C., Chang, M. C., Xu, F., & Lu, H. F., 2013. ATOP-The Advanced Taiwan Ocean Prediction System Based on the mpiPOM. Part 1: Model Descriptions, Analyses and Results. *Terrestrial, Atmospheric & Oceanic Sciences*, *24*(1).

[49] Madala, R. V., and Piacsek, S. A., 1977. A semi-implicit numerical model for baroclinic oceans, J. Comput. Phys., 23, 167-178.

[50] Mellor, G. L., 1998. Users guide for a three-dimensional, primitive equation, numerical ocean model. Princeton, NJ: Program in Atmospheric and Oceanic Sciences, Princeton University.

[51] Kara A.B., Wallcraft A.J., Metzger E.J., Gunduz M., 2010. Impacts of freshwater on the seasonal variations of surface salinity and circulation in the Caspian Sea. Continental Self Research, 30(10):1211-25.

[52] UNESCO-IHP-IOC-IAEA, 1996. Workshop on sea level rise and multidisciplinary studies of environmental processes in the Caspian region 9-12 May. Paris, Farance IOC workshop No 108.

[53] Mansoury, M., Sadri Nasab, M., and Akbari Nasab, M., 2015. Modeling of salinity and temperature field structure in the Caspian Sea using POM model, Hydrophysics, 1(1), pp. 1-13. (Persian)

[54] Maus, S. Macmillan, S., Chernova, T., Choi, S., Dater, D., Golovkov, V., Lesur, V., Lowes, F., Lühr, H., Mai, W., Mclean, S., Oslen, N., Rother, M., Sabaka, T., Thomson, A., Zvereva, T., 2005. The 10th-Generation International Geomagnetic Reference Field, Geophys. J. Int., 161, 561–565. https://doi.org/10.1111/j.1365-246X.2005.02641.x

[55] Maus, S., Manoj, C., Rauberg, J., Michaelis, I., and Lühr, H, 2010. NOAA/NGDC candidate models for the 11th generation International Geomagnetic Reference Field and the concurrent release of the 6th generation Pomme magnetic model, Earth Planets Space, 62 (2). https://doi.org/10.5047/eps.2010.07.006

[56] Macmillan, S., and Finlay, C., 2010. The International Geomagnetic Reference Field. In: Mandea, M., Korte, M., (eds) Geomagnetic Observations and Model. IAGA Special Sopron Book Series, vol 5. Springer, Dordrecht. https://doi.org/10.1007/978-90-481-9858-0_10

[57] Finlay, C.C., Maus, S., Beggan, C.D., Bondar, T.N., Chambodut, A., Chernova, T.A., Chulliat, A., Golovkov, V.P., Hamilton, B., Hamoudi, M., Holme, R., Hulot, G., Kuang, W., Langlais, B., Lesur, V., Lowes, F. J., Luhr, H., Macmillan, S., Mandea, M., Michaelis, I., Olsen, N., Rauberg, J., Rother, M., Sabaka, T. J., Tangborn, A., Tøffner-Clausen, L., Thebault, E., Thomson, A. W. P., Wardinski, I., Zvereva, T. I, 2010. International geomagnetic reference field: the eleventh generation. Geophysical Journal International, Vol, 183, no, 3, pp. 1216-1230. https://doi.org/10.1111/j.1365-246X.2010.04804.x

INTERNATIONAL JOURNAL OF
OFFSHORE & ENVIRONMENTAL ENGINEERING IJCOE Vol.7/No. 3/Summer 2022 (43-49)

Available online at: www. Ijcoe.org

Modeling of groundwater salinity on the Persian Gulf coastal plain By using linear moments and ANFIS-PSO

Amir Jalalkamali[1], Ali Sheykhbahaei[2*]

[1] Department of water engineering, Kerman Branch, Islamic Azad University, Kerman, Iran, ajalalkamali@yahoo.com*
2 Department of Nonliving Resources of Atmosphere and Ocean, Faculty of Marine Science and Technology, University of Hormozgan, Bandar Abbas, Iran Abbas, Iran, Ali.sheikhbahaei@gmail.com

ARTICLE INFO

Article History:
Received: 21 Aug. 2021
Accepted: 31 Jul. 2021

Keywords:
Salinity
ANFIS-PSO
Regional Analysis
At-Site Analysis

ABSTRACT

The main source of water in Minab is the shallow aquifer which is part of the coastal aquifer. The quality of the groundwater is extremely deteriorated in terms of salinity. Salinization of groundwater may be caused and influenced by many variables. Studying the relation of between these variables and salinity is often a complex and nonlinear process, making it suitable for artificial intelligence application. The present paper presents a comparison of the hybrid of Adaptive Neuro Fuzzy Inference System (ANFIS) with Partial Swarm Optimization (PSO) model and L-moments regarding their power and efficiency in regional and at-site anticipation of salinity of groundwater at Minab coastal plain. In doing so, electrical conductivity is considered the dependent variable, while, through regression analysis, total cations, magnesium ion, sodium percentage, and level of groundwater are assumed to be independent parameters. Results showed that, in regions with lower heterogeneity criterion, ANFIS-PSO regional forecast were moderately more accurate than at-site anticipations.

1. Introduction

In many areas, especially in arid and semi-arid regions such as Minab coastal plain, groundwater is one of the main water resources for drinking water, agriculture, and industry uses. Aquifers and the contained groundwater are inherently sensitive to pollution from many sources. These days, Groundwater simulation has been used vastly for a better management of groundwater resources. Therefore, many researchers have tried to find more accurate models, considering the actual conditions. These models require plenty of information which is difficult and sometimes impossible to gather. Salinization may be caused by a number and/or combination of different processes, including: seawater intrusion; migration of brines from the deeper parts of the aquifer; dissolution of soluble salts in the aquifer (water-rock interaction); and contribution from discharges from older formations surrounding the coastal aquifer. In addition, potential man-induced (anthropogenic) sources include agricultural return flows, wastewater seepage, and disposal of industrial wastes. In addition, water quality (e.g. salinization) is influenced by many factors such as flow rate, contaminant load, medium of transport, water levels, initial conditions and other site-specific parameters [1]. And also, considering some execution conditions, reaching a conclusion takes more time if possible at all. On the other hand, there are numerous factors in hydrologic parameters which complicate applying data to the models. Making physical and conceptual models have been poorly noticed for difficulty of gathering more information and the required time for calibration. In addition, nonlinearity of variables makes the problem more challenging. Recently, Artificial Intelligence (AI) models, as new powerful tools, have been used for forecasting hydrologic parameters. These methods act as a black box and do not require lots of physical data and are capable of estimating non-static water quality. Due to short processing time and low input data, AI models can supersede numerical ground water models. These new methods act as powerful estimators without the need for governing equations. For error reduction in regional forecasting, all selected wells must choose from one homogeny cluster. So, it is necessary to define cluster homogeny by some examinations. But one must make sure that these places are available. Because choosing some clusters with some wells inside is not sufficient for homogeny. The L-moments as the new types of statistical methods act for solving such

problems. A quick search shows that regional forecasting with ANFIS-PSO is a new method for modeling. Nero-fuzzy networks for flood regional analysis were used [2]. Investigation shows that nero-fuzzy model versus artificial neural networks and non-linear correlation, has better ability in modeling of flood estimation in watersheds without hydrometer At-Sites. L-moments was investigated the great supply of four aquifers in Australia [3]. They found that regional analysis increase the accuracy of forecasting. Adaptive neuro fuzzy inference system (ANFIS) have been used to predict water supply in terms of quality and quantity trends in sophisticated systems with acceptable accuracy. [4, 5, 6, 7 and 8]. Methods of AI are nonlinear tools of modeling which do not need any explicit of the physical relationship of the problem. Through recent years, those successful applications for Soft Computing Techniques in the field of water engineering have been published in a great scale. [9, 10 and 11]. This paper attempts forecasting regional salinity of groundwater of Minab coastal plain by ANFIS-PSO with L-moments and comparison of between regional and At-Site results.

2. Study area

The Minab coastal plain is located in 56 º 48′ - 57 º 15′ E and 26 º 1′ - 27 º 27′ N. It covers a total area of 1378.8 square kilometers and its plain has an area of 788 square kilometers along the Persian Gulf. The maximum height of this plain is 50 meters and its minimum is zero. The main river is the Minab River (Fig. 1).

Figure1. Location of Minab coastal plain.

3. Materials and methods

3.1. L-moments

(Hosking, 1990) has a new definition of L-moments. Based on his studies, L-moments are analogous to traditional moments which are expressible as linear combinations of order statistics. Basically L-moments have linear functions as probability-weighted moments (PWMs) [12]. Alike conventional moments, the primary objective of PWMs and L-moments is to summarize previously-observed samples and theoretical distribution. The theory of PWM was summarized and defined by (Greenwood et al., 1979) as the following [13]:

$$\beta_r = E\{X[F_X(x)]^r\} \quad (1)$$

Where βr is the rth order PWM and FX(x) is the cumulative distribution function of X. Unbiased sample estimators (bi) of the first four PWMs are given as [14].

$$\begin{aligned}
\beta_0 &= m = \frac{1}{n}\sum_{j=1}^{n} X_j \\
\beta_1 &= \sum_{j=1}^{n-1}[\frac{n-j}{n(n-1)}]X_{(j)} \\
\beta_2 &= \sum_{j=1}^{n-2}[\frac{(n-j)(n-j-2)}{n(n-1)(n-2)}]X_{(j)} \\
\beta_3 &= \sum_{j=1}^{n-3}[\frac{(n-j)(n-j-1)(n-j-2)}{n(n-1)(n-2)(n-3)}]X_{(j)}
\end{aligned} \quad (2)$$

Where x(j) represents the ranked AMS with x(1) being the highest value and x(n) the lowest value, respectively. The first four L-moment are given as follow

$$\begin{aligned}
\lambda_1 &= \beta_0 \\
\lambda_2 &= 2\beta_1 - \beta_0 \\
\lambda_3 &= 6\beta_2 - 6\beta_1 + \beta_0 \\
\lambda_4 &= 20\beta_3 - 30\beta_2 + 12\beta_1 - \beta_0
\end{aligned} \quad (3)$$

Non-biased sample estimators in the first four L-moments are resulted by the substitution of the PWM sample estimators from Eq. (2) and Eq. (3). The first L-moment λ_0 and the mean value of X are equal. At the end, the L-moment ratios are calculated as:

$$\begin{aligned}
L-C_V &= \tau_2 = \frac{\lambda_2}{\lambda_1} \\
L-\gamma &= \tau_3 = \frac{\lambda_3}{\lambda_2} \\
L-k &= \tau_4 = \frac{\lambda_4}{\lambda_2}
\end{aligned} \quad (4)$$

Sample estimates of L-moment ratios are obtained by substituting the L-moments in Eq. (4) with sample L-moments.

3.2. Heterogeneity Measure

Heterogeneity measure is used for identification of homogeneous regions based on observed and simulated dispersion of L-moments for a group of sites under consideration. This can be computed from [15]:

$$H = \frac{(V_1 - \mu_{V1})}{\delta_{V1}} \quad (5)$$

Where V = weighted standard deviation of values, , = the mean and standard deviation of Nsim values of , and Nsim = number of simulations.

A region is declared ‘acceptably homogeneous’ if H<1; ‘possibly heterogeneous’ if 1<H<2; and ‘definitely heterogeneous’ if H≥ 2. To avoid committing to a

particular 2 or 3 parameter distribution, simulation is undertaken using a 4 parameter Kappa distribution and the number of simulation is kept at least at 500 to arrive at reliable estimates of and. In addition to the above, two additional measures H1 and H2 based on LCV/LCS and LCS/LCK distances respectively are also considered. The measure H1 indicates whether at-site and regional estimates will be close to each other, while H2 indicates whether the at-site and regional estimates will be in agreement. A large value of H1 usually indicates a large deviation between regional and at-site estimates, whereas a large value of H2 indicates a large deviation between at-site estimates and observed data.

3.3. Discordance Measure

Discordance measure, ZDIST, is used to screen out the data from unusual sites, i.e. sites whose at-site sample l-moments are markedly different from other sites and is defined as [16]:

$$D_i = \frac{1}{3}(u_i - \bar{u})^T \cdot S^{-1} \cdot (u_i - \bar{u}) \quad (6)$$

Where Ui = vector of LCV, LCS and LCK for a site i; S = covariance matrix of V; $\bar{u}$ = mean of vector Ui.
A given site is declared discordant if Di≤3. Critical value of ZDIST defines as [14]:

$$D_i \le (n-1)/3 \quad (7)$$

Where n is number of At-Sites in studied region.

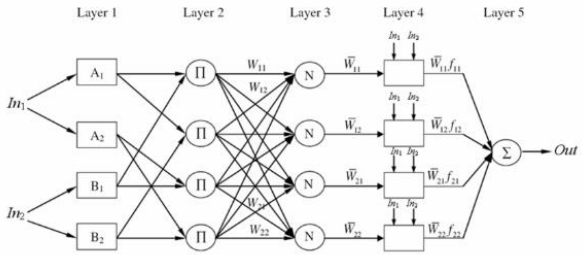

Figure 2. A typical ANFIS architecture for a two-input Sugeno model with four

3.4. The neuro-fuzzy structure

The ANFIS, the multilayer feed-forward network, maps inputs into an output using neural network learning algorithms and fuzzy reasoning. It is certain that a fuzzy interference system (FIS) is implemented in the framework of adaptive neural networks. Fig.1 illustrates the architecture of a typical ANFIS with five layers:

For simplicity, a typical ANFIS architecture with only two inputs leading to four rules and one output for the first order Sugeno fuzzy model is expressed [17,18]. It is also assumed that each input has two associated membership functions (MFs). It is clear that this architecture can be easily generalized to our preferred dimensions. The detailed algorithm and mathematical background of the hybrid learning algorithm can be found in the Reference [18].

3.5. ANFIS-PSO method

There is a hybrid of canonical real-coded PSO, subtractive clustering and ANFIS, designed and finalized for the purpose of producing suitable approximate fuzzy models for the sake of accuracy and parsimony. The primary procedure of modeling is an optimization task executed by PSO where both the accuracy and compactness of fuzzy models are the subjects of simultaneous optimization. The whole process of optimization by PSO is based all particles that fly over the *D*-dimensional solution space are subject to updated rules for new positions, until the global optimal position is found. Velocity and position of a particle are updated by the following stochastic and deterministic update rules [19]:

$$v_i(t) = \omega v_i(t-1) + \rho_1 \left(x_{Pbest_i} - x_i(t)\right) + \rho_2 \left(x_{Gbest} - x_i(t)\right) \quad (8)$$

$$x_{i(t)=} x_i(t-1) + v_i(t) \quad (9)$$

where ω is an inertia weight and are random variables. The random variables are defined as and with r1, r2, U(0, 1), and C1 and C2 are positive acceleration constants. Acceleration constants C1 and C2 represent the weights of the stochastic acceleration terms that push a particle toward Pbest and Gbest, respectively. The flow chart of modeling procedure is illustrated in Fig.3.

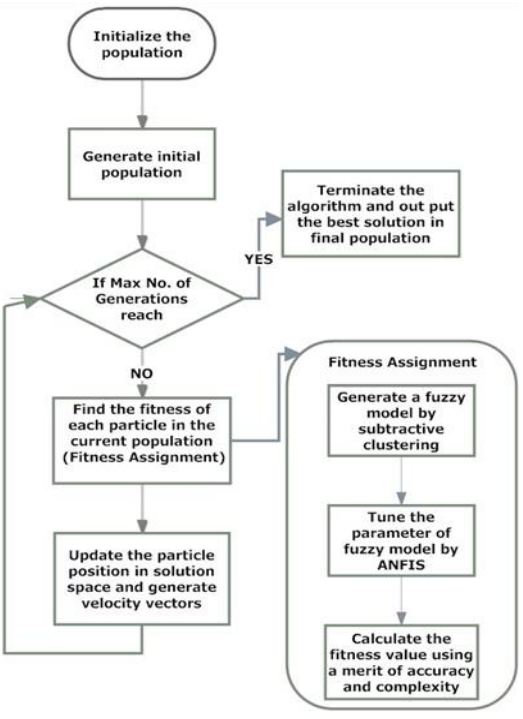

Figure 3. Steps of ANFIS-PSO model procedure

Subtractive clustering method can be used to generate a fuzzy model of TSK in which the number certain rules (i.e. the number of clusters) is determined through radii parameters dedicated into dimensions. These radii are mainly used for the purpose of cluster generation. Each cluster is meant to represent a rule and according to the fact that clustering is completed in multidimensional space, and fuzzy sets for each rule must be achieved. By projecting the center of each cluster in the corresponding dimension, the centers of MFs are obtained. The widths of MFs for a single dimension are obtained on the basis of radius ra which is particularly considered for that dimension. Therefore, each chromosome in this study acts as radii values encoder for all dimensions inputs and outputs of a fuzzy model. These radii of fuzzy model are then used by subtractive clustering to generate a TSK FIS.

3.6. Simulation setup

The PSO algorithm parameters chosen for the tuning purpose are: ps = 100, c_1 and c_2 =2, w_{max} = 0.9, w_{min} =0.3. Number of epochs and learning rate are set to 100 and 0.2 for ANFIS. Ranges of radii are considered to be in interval [0.1, 2]. In the following subsections case studies are described in more detail.

4. Results and discussions

First step to define a homogenous region is choosing the most important clustering parameters. Choosing all important parameters to define a homogeny cluster for a phenomena,increase calculating time and errors, so, choosing the most important parameters would make the calculation simpler, without resulting in any major differences. In this paper, out of effective parameters (time series parameters recorded) more important parameters were selected through regression analysis. Results showed that all of the cations, magnesium ions, sodium percentage, and groundwater level have more effect on salinity. Therefore, these parameters are used for electrical conductivity in clustering and also input parameters for forecasting. In this paper, with K-Means method and Ward hierarchical, the region was divided into 2, 3, and 4 sectors, respectively. And then, the incompatibility and non-homogeny criteria for the region were defined. For choosing the best clustering mode and optimum number of regions, incompatibility summation of At-Sites, defining the number of incompatible At-Sites with more degree of 1.5, 2 and 3, and also non-homogeny criteria were conducted for each and every region. Results are shown in Table.1

Considering Table.1, when all the At-Sites are considered as one region, only the H1 criteria are homogeny while H2 and H3 are non-homogeny. In general, K-mean method includes 4 regions as the priority and Ward, with 4 regions in the next place. Considering 4 homogeny regions for research area, some wells were scattered in the other areas.

Table 1. Non- homogeny criteria for different scenarios

Criteria H_3	Criteria H_2	Criteria H_1	Region	Method
6.77	2.5	1.5	Total	Total wells of a region
1.22	1.01	0.6	A	K-Means 2 region
2.5	-0.91	-0.45	B	
1.3	0.65	0.4	A	K-Means 3 region
2.28	-0.53	-0.25	B	
3.29	-0.99	-0.45	C	
0.88	0.15	0.1	A	K-Means 4 region
1.01	-0.35	-0.25	B	
0.9	-0.22	-0.11	C	
1.8	0.45	0.12	D	
1.22	1.01	0.6	A	Ward 2 region
2.5	-0.91	-0.45	B	
1.21	0.59	0.32	A	Ward 3 region
2.33	-0.43	-0.31	B	
1.09	-0.71	-0.33	C	
0.92	0.23	0.14	A	Ward 4 region
1.17	-0.25	-0.41	B	
1.29	-0.31	-0.14	C	
1.96	0.69	0.45	D	

To solve this problem, all the following, well No3 in region A, well No15 in region B, and well No27 in region D were combined together and then the non-homogeny criteria were computed. Relocation of the wells increased the non-homogeny of region A and B and decreased that of region C. To define the increase of non-homogeny, incompatibility of the wells was investigated and it was observed that well No14 was incompatible. The well was moved to region B and computation was restarted. The results showed decreased incompatibility for well No14. And finally, with moving to region B and re-computation, better results were achieved. Figures below show the final homogeny regions.

4.1. Regional forecasting

First and foremost, for regional forecasting, dimensionless data was computed in each one of the three regions including both selection input data and electrical conductivity. After choosing the best scenario for forecasting, by multiplying average off each well by regional dimensionless data, the dimensionless forecasting data is obtained for each well. Desired periodical statistics are considered on a monthly basis from 2001 to 2013. For analysis, 156 regional dimensionless data were used. In this research, 70 percent of the data was used for teaching, 10 percent for validation, and the remaining 20 percent was used

for the testing. Furthermore, for regional forecasting, models constructed with the relation equation are studied. In all models, the momentum training and ANFIS-PSO method were used.

Table 2. The best topology of ANFIS-PSO model for the study areas

Region	Model	NO. OF INPUT VARIABLE	NO. OF RULES	No. of MF	R^2
A	ANFIS-PSO	4	6	24	0.9765
B	ANFIS-PSO	4	5	20	0.9956
C	ANFIS-PSO	4	3	12	0.9949

Having observed the results of correlation coefficient and non-homogeny criteria, it is obvious that non-homogeny decreased, the correlation coefficient of the observed data and regional forecasted data decreased as well. The reason is that low non-homogeny means incompatibility of the wells with the other wells in the same region. So, this would be able to reduce forecasting error. After implementing the proposed method (ANFIS-PSO) for each region, with multiplying the coefficient of each At-Site for the desired year, by regional forecasting data, electrical conductivity was calculated for each At-Site, and, finally, between the observed and calculated data, the correlation coefficient was calculated. Tables 4 to 6 show the correlation coefficient for each well.

Table 3. The correlation coefficient between observed and predicted data for each well in the area A

R^2	Well number	R^2	Well number
0.97	8	0.86	1
0.90	9	0.91	2
0.92	10	0.77	3
0.94	11	0.93	4
0.99	12	0.95	5
0.89	13	0.97	6
		0.90	7

Table 4. The correlation coefficient between observed and predicted data for each well in the area B

R^2	Well number	R^2	Well number
0.90	19	0.98	14
0.92	20	0.79	15
0.91	21	0.99	16
0.96	22	0.99	17
		0.86	18

Table 5. The correlation coefficient between observed and predicted data for each well in the area C

R^2	Well number	R^2	Well number
0.91	29	0.85	23
0.98	30	0.86	24
0.95	31	0.93	25
0.98	32	0.93	26
0.84	33	0.73	27
0.99	34	0.90	28

Considering the results shown in tables 3, 4, and 5 the wells No3, No15 and No27 which were moved before, have the least correlation coefficient. Better correlation coefficients are associated with the wells with salinity levels close to that of the regional average. Thus, it follows that regional analysis can forecast with high precision, in case of selection of wells and internal At-Sites. Figures 4 and 5 show forecasting and regional salinity. According to figures, it would be useful to reduce the abstraction rate and increase the recharge quantities (the groundwater level) to the aquifer as a strong remedial action for solving the groundwater deterioration problem in the aquifer of Minab coastal plain (salinity).

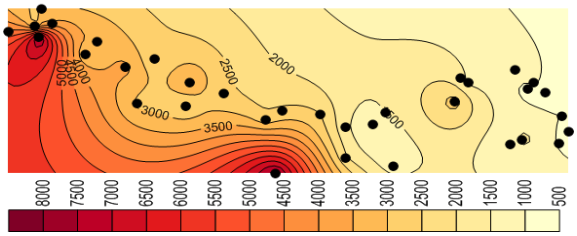

Figure 4. Observed salinity for September 2013

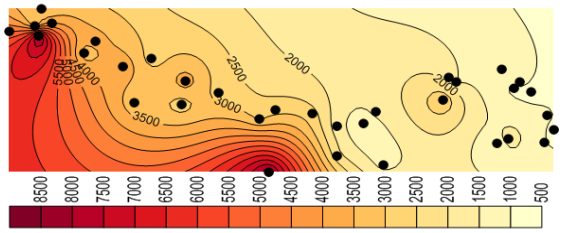

Figure 5. Predicted salinity for September 2013

4.2. At-Site forecasting

For forecasting the salinity of our 34 wells, similar to the regional method, the proposed method ANFIS-PSO is applied to each well. For this purpose, the correlation coefficient between the observed data and forecasted data was obtained. After choosing the appropriate model, the forecasting started. Review of the results suggests that the salinity of groundwater for the study area increased during the past years. And also it's clear that ANFIS-PSO is capable of forecasting acceptable groundwater salinity.

4.3. Comparison of At-Site and regional forecasting

Priority of regional or At-Site analysis for each studied well of Minab plain was revealed through the method of correlation of coefficient, and then inserted into Table 6.

Table 6. Correlation coefficient for best structures at different Wells

Priority	Correlation Coefficient		Well No
	Regional	At-Site	
At-Site	0.86	0.95	1
At-Site	0.91	0.98	2
At-Site	0.78	0.83	3
At-Site	0.93	0.95	4
At-Site	0.95	0.96	5
Regional	0.98	0.91	6
Regional	0.90	0.82	7
Regional	0.97	0.89	8
At-Site	0.91	0.95	9
Regional	0.92	0.91	10
Regional	0.94	0.89	11
Regional	0.98	0.92	12
Regional	0.89	0.81	13
Regional	0.98	0.83	14
At-Site	0.79	0.87	15
Regional	0.98	0.9	16
Regional	0.99	0.94	17
Regional	0.86	0.85	18
At-Site	0.90	0.96	19
Regional	0.82	0.88	20
Regional	0.91	0.93	21
At-Site	0.93	0.93	22
At-Site	0.85	0.81	23
Regional	0.87	0.93	24
Regional	0.93	0.94	25
Regional	0.93	0.89	26
At-Site	0.73	0.8	27
At-Site	0.90	0.87	28
Regional	0.91	0.91	29
Regional	0.95	0.95	30
Regional	0.94	0.94	31
Regional	0.98	0.95	32
At-Site	0.83	0.95	33
Regional	0.98	0.97	34

According to the results mentioned above, 21 wells with regional analysis and 13 wells with At-Site analysis method maintain good accuracy. The investigation shows that for wells, for which regional analysis shows lower accuracy in comparison to At-Site analysis, the average is above regional average (wells No_1, No_5, No_9, No_{15}, No_{19} and No_{22}) or below regional average (wells No_{23}, No_{28} and No_{33}). The rate of incompatibility for these wells is higher than the other regional homogenous wells. Region A has the most priority in At-Site analysis followed by C and D. As a result, the most important regions for analysis are the non-homogenous regions. As a result, in case of proper selection of the at-sites in a homogeneous region and low at-sites incompatibility as well as non-homogeneity criterion, regional analysis is preferable to at-site analysis.

5.Conclusion

The current research showed that hybrid models can be used in groundwater quality management and outcome is comparable to other used approaches such as groundwater numerical modelling. According to regression analysis, sum of cations, magnesium ions, percentage of sodium, and groundwater table are the most effective on salinity. Moreover, for defining the number of homogeny clusters, generally, K-Means method, with 4 regions is the first and Ward with 4 regions is the second suitable selection. As the non-homogeny criteria decreased, correlation coefficient between the observed data and regional forecasted data reduced as well. The largest correlation coefficient was associated to the wells with close salinity to the regional average. In case of precise selection of the wells and At-Sites inside the region, the regional analysis can forecast with high accuracy. The most important regions for analysis are the non-homogenous regions. Forasmuch as, the PSO, which is a global random optimization algorithm, can simultaneously identify system structure and parameters. Therefore, the ANFIS-PSO model analysis showed an increase in the compactness and accuracy of the mentioned model during the testing stage. Our proposed method aiming to provide us with the best and effective composition of structure in the ANFIS model exchange rise and fall between the precision and the simplicity. The maintained results are to show a new hybrid algorithm providing both accuracy and complexity for a Neuro-Fuzzy model.

References

[1] Govindaraju R. S., (2000). "Artificial neural network in hydrology". Journal of Hydrologic Engineering, 5(2), 124-137.

[2] Shu, C., Ouarda, T.B.M.J. (2008). Regional flood frequency analysis at engaged sites using the adaptive neuro-fuzzy inference system. Journal of Hydrology., V.349, PP.31-43.

[3] Furst, j., Bichler, A. and Konecny, F. (2014). Regional Frequency Analysis of Extreme Groundwater Level. Journal of Grounwater, Jonwielly.

[4] Jalalkamali, Amir.,Sedghi, Hossein., Manshouri, Mohammad .(2011)., Monthly groundwater level prediction using ANN and neuro-fuzzy models: a case study on Kerman plain, Iran, Journal of hydroinformatics (13.4) 867-876.

[5] Adamowski, Jan., Fung Chan, Hiu. (2011)., A wavelet neural network conjunction model for groundwater level forecasting, Journal of Hydrology (407) 28–40.

[6] Lohani, AK., Krishan, G. (2015) Application of artificial neural network for groundwater level simulation in Amritsar and Gurdaspur districts of Punjab, India. Journal of Earth Science and Climate Change 6:274.

[7] Samson,M., Swaminathan, G., Venkat Kumar, N.(2010)., Assessing groundwater quality for portability using a Fuzzy logic and GIS – a case study of Tiruchirappalli city – India, Computer Modeling and New Technologies., Vol.14, No.2, 58–68.
[8] Jalalkamali, Amir. (2015)., Using of hybrid fuzzy models to predict spatiotemporal groundwater quality parameters, Earth Science Informatics, DOI 10.1007/s12145-015-0222-6.
[9] Jalalkamali, Amir. Moradi, Mehdi., Moradi, Nasrin. (2015)., Application of several artificial intelligence models and ARIMAX model for forecasting drought using the Standardized Precipitation Index, International Journal of Environmental Science and Technology, Volume 12, Issue 4, pp 1201-1210.
[10] Lohani, AK., Krishan, G. (2015)., Groundwater Level Simulation Using Artificial Neural Network in Southeast, Punjab, India, Journal of Geology & Geophysics 4: 206.
[11] Seyam, Mohammed.,Mogheir, Yunes. (2011). A NEW APPROACH FOR GROUNDWATER QUALITY MANAGEMENT, the Islamic University Journal (Series of Natural Studies and Engineering), Vol.19, No.1, pp 157-177.
[12] Hosking, J.R.M. (1990). L-moments: Analysis and estimation of distributions using linear combinations of order statistics: J.R. Stat. Soc., Ser. B, 52, 105-124.
[13] Greenwood, J.A., Landwehr, J.M., Matalas, N.C., and Wallis, J.R. (1979). Probability weighted moments: Definition and relation to parameters of several distributions expressable in inverse form. Water Resources Research, 15(5), 1049-1054.
[14] Hosking, J. R. M., & Wallis, J. R. (1997). Regional Frequency Analysis: An Approach Based on L-Moments. Cambridge Univ. Press, New York.
[15] Kjeldsen, T. R., Jones, D. A. (2006). Prediction uncertainty in a median-based index flood method using L- moments. Water Resources Research, V. 42.
[16] Rostami, R., & Rahnama, M. B. (2007). Halil-river Basin regional flood frequency analysis based on l-moment approach. International journal of agriculture researches, USA, Newyork.
[17] Sugeno, M. (1985)Industrial applications of fuzzy control. Elsevier Science Pub.Co.
[18] Wang,YM.,Elhag, T. (2008) An adaptive neuro-fuzzy inference system for bridge risk assessment. Expert Systems with Applications 34(4): 3099-3106.
[19] Jang JSR. (1993) ANFIS: Adaptive-network-based fuzzy inference systems, IEEE Transactions on Systems Man and Cybernetics, 23 (3), pp 665–685.
[20] Kennedy J, Eberhart R (1995) Particle swarm optimization. In: Proceedings of the IEEE international conference on neural networks, Perth, pp 1942–1948 Z.

INTERNATIONAL JOURNAL OF
COASTAL, OFFSHORE & ENVIRONMENTAL ENGINEERING IJCOE Vol.7/No. 3/Summer 2022 (50-57)

Available online at: www.Ijcoe.org

Experimental analysis of the impact of communication strategies on secure shipping communications

Vahid Rahmati[1], Ali Mohammad Mazidi Sharafabadi[2*], Seyed Alireza Afshani[3]

[1] *Ph.D. Student of Social Communication Sciences, Maybod Branch, Islamic Azad University, Maybod , Iran*

[2*] *Assistant Professor of Communication Sciences, Department of Human Sciences, Maybod Branch, Islamic Azad University, Maybod, Iran, mazidi6@yahoo.com*

[3] *Professor of Sociology, Department of Social Sciences, Yazd University, Yazd, Iran*

ARTICLE INFO

Article History:
Received: 07 Aug. 2021
Accepted: 15 Dec. 2022

Keywords:
Public Relations
Marine Culture
Communications
Shipping

ABSTRACT

Given the importance of Iran as a country with 11 ports and a wide range of commercial, military and passenger shipping, appropriate measures should be taken for shipping safety. This study seeks an empirical analysis of the impact of public relations strategies on secure shipping communications. The research method is both qualitative and quantitative. In the quality phase, semi-structured interview tools are used to interview professionals who have at least 10 years of experience working on the ship and are familiar with technical issues and reported cases; Until we achieved theoretical saturation and the obtained components were coded using Max QDA software. therefore, Dimensions of seafarers' problems, shareholder liability, maritime accident management, maritime accident crisis management, protection of interests, demand for seafaring, marine culture, reducing seafarers' concerns, maritime culture and improving the quality of seafarers' education were identified and evaluated by public relations strategies.

In the quantitative phase, the research hypotheses were evaluated using a questionnaire tool and the hypotheses were analyzed using SPSS software and linear regression test and all research hypotheses were approved.

1. Statement of the problem

Public relation is a systematic process about which there are different theories [1]; Many see this process as a tool for pursuing private interests [2], and others argue that public relations is reassuring through the constant flow of information in The political arena and civil society contribute to the democratization of communication [3]. But our discussion in this study goes beyond what has been discussed so far about public relations. our vision toward public relations goes beyond a systematic view and is actually based on the role of the organization's relationship with the people. According to the researcher, public relations is an organizational knowledge and developer of organizational standards that takes public relations out of the form of media for communication inside and outside the organization, and use its information to advance internal standards.

Public relations is a comprehensive institution in the organization that has the capacity to concentrate a lot of information. This valuable institution can exist in any organization as a decision maker in the management of the organization.

The notion that many organizations consider public relations as the language of the organization and its managers, has taken away the aim and planning from this institution and has diminished its strategic role.

The development of public relations as a science and the addition of scientific strategies to the matter, has expanded the views in this field day by day and improved its definition. Therefore, public relations is the art of recreating information and communication, in order to expand understanding and achieve long-term trust between the organization and the audience in order to achieve organizational goals. The basis of this research has emerged from the mentioned perspective and seeks to explain public relations

strategies in secure shipping communications. Therefore, it must be acknowledged that planning and formulating a vision to achieve organizational goals requires the processing of environmental information based on the needs of the organization. Also, understanding the audience through situation analysis is an important element to achieve success in the organization. In light of these two basic principles, public relations management strategies have an evidence-based strategic approach and in fact emphasize the understanding of competitive change and capital potential through research in order to achieve success through quantitative evaluation methods. With this description, public relations is an institution that needs logical communication strategies based on accurate and extensive data processing to be able to utilize all the capacities within the organization and outside the organization, including the community, customers, suppliers and elites in line with organizational goals and interests.

The shipping industry is perhaps the first and one of the most critical industries, especially as shipping plays a vital role for national security, economy and transportation. In 2004, the US Coast Guard had a budget of $ 330 million, and overall financial and figures reflect the importance of the industry, for example, there are about 50,000 ships in the world's merchant fleet carry goods around the world. In Iran, 90% of trade is done by sea. The shipping industry has a good record of safe shipping; however maritime accidents can potentially be catastrophic. There is a combination of factors such as fatigue, stress, lack of proper communication, environmental factors, long time away from home in the maritime industry that can potentially contribute to accidents [4].

One of the basic skills in implementing, safe producing and working in all high-risk industries is proper public relations and communication strategies; this skill also affects other criteria such as the awareness of the situation, teamwork and decision making. The CTSB, short for Cape Town Association of the Blind, studied and reviewed 273 incidents that occurred to ships in Canadian waters between 1978 and 1992. (Local waters are areas near the coast of any country where a local pilot goes and boards the ship that arrives at the port and due to being familiar with the waterway and the area, guides the ship in or out of the port). In the CTSB sampling of accidents, 42% of cases were due to misunderstandings between the pilot and the captain or lack of communication. If the deck officer is stunned and speechless when his commander run the ship aground or collides with another ship, it seems that a lack of non-technical skills (such as the example we used regarding communication) can sometimes lead to accidents.

In fact, in our point of view, public relations is an information center that should be able to institutionalize safety in the organization. On the other hand, in risk communication management analysis and presentation of awareness and knowledge, in positive aspects, it creates trust, honesty and support, and in negative aspects, it causes distrust and fear. Therefore, in communication science, the development of knowledge to reduce risk and increase safety is one of the basic tasks of public relations as a decision-making body. Transportation, and in particular maritime transport, in the communication evolution era, is involved in a close and intense competition that requires purposeful evaluation based on extensive data in order to achieve its desired goals in the light of safety and speed. Meanwhile, good organizational performance is formed only by processing data and making decisions in the light of useful and purposeful communication; Communications based on ethics, transparency and comprehensive information. Some consider the organizational model of public relations strategies as the involvement of the management of the public relations institution and believe that in this regard, all elements of the organization (internal and external beneficiaries) will significantly and imperceptibly be involved in decision-making process. Accordingly, considering the importance of Iran as a country with 11 ports and a wide range of commercial, military and passenger shipping activities, the country must take appropriate measures for shipping safety. In this study, we seek empirical analysis of the impact of public relations strategies on secure shipping communications.

2. Research Significance

Strengthening public relations strategies is a very practical issue, the results of which can help empower the entire organization, especially human and financial resources; as fixing and optimizing strategies will lead to administrative focus and executive processes, which will result in work and administrative discipline throughout the organization. Communication plays an essential role in organizational management and all-round development. Good management is formed when proper and optimal communication is established in the organization. Today, with the complexity of the social system, the importance, role and necessity of public relations as a communication technique and art that facilitates the cycle of internal and external communication in government executive agencies and organizations has been highlighted more than ever. Few organizations can be found in the current age that do not need a public relations unit as a center for information gathering and circulation. An efficient and strong public relations facilitates the flow of information from the organization to different groups of people and audience and plays an effective role in guiding and directing the public opinion of the society [5].

On the one hand, scientifically, the mission of public relations is sustainable development and success in the

organization, which is realized through maintaining the interests of the organization and its audience. One of the important goals of the Ports and Maritime Organization of Iran is to provide safe shipping conditions and the most important strategy in this regard is to establish secure communications. Among the causes of accidents in the maritime transport industry, non-human errors, including equipment failure, mechanical and structural failure, together account for 23% of all errors. In contrast, 78% of marine accidents are reported to be related to human error. This research identifies the factors that affect the safety of the deck officers' performance, and indicates that better planning can be done to improve their performance and the public relations of the related organization. When the entire voyage of a ship is carried out safely and set off safely from the port of origin to the destination, it will create a good reputation for the shipping company. The less maritime accidents caused by the poor performance of deck officers, the better the company's reputation in international markets. Today, the human factor and the quality of manpower performance have in fact become a very important and strategic competitive advantage among various shipping and oil tanker companies worldwide. Communication allows the exchange of useful information and data between the parties. In dynamic organizations, the best place to achieve this aim is the public relations institution. Therefore, the realization of secure communication platform through public relations strategies and using empirical analysis and available data is essential and leads to process optimization and sustainable success in secure shipping communications.

3. Research Purpose

Experimental analysis of the impact of public relations strategies on secure shipping communications

Research Questions

1-Does informing aspect of public relations awareness strategies have an impact on secure shipping communications?

2-Does Organizational motivation aspect of public relations awareness strategies have an impact on secure shipping communications?

3-Does issue prediction aspect of public relations awareness strategies have an impact on secure shipping communications?

4-Does opportunity aspect of public relations awareness strategies have an impact on secure shipping communications?

5-Does Crisis Management aspect of public relations awareness strategies have an impact on secure shipping communications?

6- Does Crisis Management aspect of public relations awareness strategies have an impact on secure shipping communications?

7- Does social responsibility aspect of public relations awareness strategies have an impact on secure shipping communications?

4. Theoretical Foundations

4.1 Public relations' role in the organization

Considering the role they play in the organization's contact with social groups, Public relations administrators, in terms of providing information from the environment to management, and in particular the relationship between the organization and key groups within the audience, may be expected to have the potential to influence the strategic decision-making process of the organization. However, this potential may not be realized by individuals within the organization, depending on how it is perceived and understood. As (Catlin et al.) Stated in 1984, by adopting different roles in the organization and using behavioral patterns, public relations practitioners and experts deal with different events and adjust the expectations of others and form a logical form.

4.2. The most important safety and accident approaches

The organizational impact on individual behavior is an important issue in risky industries; Because human errors occur in the organizational context. In high-risk industries, even a small human error can lead to devastating accidents. According to the International Atomic Energy Agency, a weak culture of safety was one of the reasons for the Chernobyl nuclear accident [6].

Human error is more prevalent in industries such as construction, aviation, nuclear energy, and oil production [7]. The biggest factor in all air accidents is human error. For several reasons, individuals are often blamed for air accidents rather than organizations: It is easier to assign legal responsibilities to individuals. It is easier to relate personal error to an accident because this relationship is tangible. There are limited studies that show the relationship between organizational errors and events because the nature of the relationship between organizational variables and events is not tangible. Blaming individuals is more financially beneficial than organizations [8].

In recent years, however, researchers have realized the organizational effects on the complex nature of human error events. Domino theory, proposed by Baird [9], is the first and most well-known model of organizational effects on human adverse events. This theory states that every unfortunate event is the result of a series of events, each of which follows the other in a logical order. For example, human error occurs when the management of interaction and monitoring the action of an individual fails [9].

The second approach was proposed by Degani and Wiener. This approach was to identify the relationship

between management philosophy, organizational policies, operational processes and the way people work during flight operations. Ambiguity in these factors or the occurrence of conflict between these factors endangers immunity [10]. Inactive and invisible factors may be triggered by any accident-causing event into unforeseen disasters. According to Turner's model, it is necessary to separate the possible causes of accidents from a series of events that may lead to the accident [11].

Perrow(1999) highlights the essential role of organizational management in complex organizations. Organizational complexity is due to modern technologies in tools and development of management systems. Complex organizations have more accidents than non-complex organizations. The root of failures in complex organizations can be managed by strong managers. One of the best patterns of human error is the Swiss cheese pattern of Reason (1990). Reason focuses on active and latent errors. While active errors are detected almost directly, latent errors are inactive. Until they suddenly cause an accident. The importance of errors in human accidents is in emphasizing the relationship between the three hierarchical layers, which are: preconditions for unsafe activities, unsafe supervisor and organizational effects, respectively. Any failure in the interaction of these factors causes a hole in the system. With the contribution of each of these factors, each incident that occurs is the end result of a number of failures, the last of which is the unsafe activity of individuals[7]. presented a four-tier version of the Reason model: unsafe behavior, preconditions for unsafe activities, unsafe supervisor, and organizational impacts are categorized into organizational processes in the subgroups of resource management. Organizational atmosphere refers to a series of organizational characteristics including organizational structure, policy design and organizational culture. Organizational atmosphere and culture are known as root factors that affect personal safety behavior in the workplace. Zohar (1920) One of the leading organizational scientists has defined organizational culture as the common understanding of individuals about the organization in which they work. According to Lundberg (1922), organizational culture is the determinant of individual safety behavior. Organizational culture mainly affects the value system, attitudes and behaviors.

In general, it can be said that theories of accidents' causes have been developed in four stages:

The first stage, the technical period: In this period, most accidents were attributed to mechanical performance, design errors and tool defects.

The second stage, the human period: with the advancement of technology, accidents were attributed to the lack of proper use of these tools by humans.

Third stage, socio-technical period: In this period, the lack of proper interaction between individuals and mechanical systems is the cause of accidents.

The fourth stage, the cultural period: This period is a combination of the previous three stages. The cultural course emphasizes the importance of the environment and other factors in the organizational context.

5. Research Methods

In conducting this research, both qualitative and quantitative methods have been used. In the qualitative phase, semi-structured interviews were used and interviews were conducted with specialists who have at least 10 years of experience in working on ships and are familiar with technical matters and pay special attention to the reported cases. After the interview and gaining access to the research components, a questionnaire was prepared in a small part and for more people according to the statistical community of ports (from managers and experts of public relations and senior managers in the Ports and maritime Organization headquarters (11 ports), based on the method The whole census was distributed among all members of the statistical population (118 people).

5.1. Statistical population, study population and sampling method

10 people were selected as the statistical population of this study and they were interviewed. quantitatively, the statistical population is the number of public relations of 11 ports in Iran, which is about 118 people. The sampling method is due to the small number of statistical population. In the data extraction stage, 18 questionnaires were removed due to incomplete answers and only the data of 100 questionnaires were analyzed.

5.2. Data collection tools

Gathering the information of the qualitative phase in this research will be the interview and the tool of the quantitative phase will be the questionnaire. Therefore, to collect information, we will be extremely cautious to have a specialized analysis based on objective experience. Accordingly, we will use observation, interviews, databases and questionnaires to provide more objective information for data processing. In the qualitative phase, the method of interviewing educated experts with communication expertise was used and a quantitative questionnaire was obtained based on the identified variables. In the theoretical phase, the library method and related sites are used. Observations, interviews and databases will be used to extract qualitative data on the experience of using public relations strategies in the Ports and Maritime Organization and a questionnaire will be used to weigh and collect quantitative data.

5.3. data analysis method

To evaluate the qualitative data, Max QD software has been used to evaluate and identify the research components as well as to present a qualitative model. The regression method has been used to test the hypotheses and to evaluate the effect of the dimensions of the research variables.

5.4. Validity

Validity is a term that refers to the purpose for which the test was designed to be performed. Researchers use different types of this test to measure their instruments. This concept answers the question that measurement tools measure the desired feature to some extent. Without knowing the validity of the measurement tool, the accuracy of the data obtained cannot be guaranteed [12]. Validity tests can be grouped under three general headings: content validity, standard validity and construct validity [13]. Content validity basically means to what extent an empirical tool covers the content domain of a concept. This narrative uses tools and questions that deal with the main concepts of the research subject. And checks if he answers to the questions are relevant and clear. Form validity is one of the types of content validity. form validity considers the extent to which test questions are similar in appearance to the subject being prepared for measurement and if the questions are useful for measuring variables. In fact, form validity cannot be a kind of validity, but only a feature of the test that is useful in some cases. In some tests, especially recruitment tests, if the test lacks form validity, the test taker may not be interested in answering the questions, as it may be thought that the test is based on employment decisions and has nothing to do with the volunteer qualifications [14].

There are two ways to check the content validity of the test:

Content validity ratio index (CVR)

This index is designed by Lavshe. In order to calculate this index, the opinions of experts in the field of test content are used and by explaining the objectives of the test to them and providing them with operational definitions related to the content of the questions, they are asked to categorize each question based on Likert three-part Classification of the "item is necessary", "item is useful but not necessary" and "item is not necessary". Then, the content validity ratio is calculated based on the on the number of experts who evaluated the questions, the minimum acceptable CVR value should be based on the table below. Questions with CVR calculated value of less than the desired amount according to the number of experts evaluating the question, they should be excluded from the test because they do not meet the acceptable content validity based on the content validity index. At this stage, the opinion of 15 experts has been used.

$$CVR=\frac{\text{The number of experts who have selected the option: necessary}-\frac{\text{total number of experts}}{2}}{\frac{\text{total number of experts}}{2}}$$

Content validity index (CVI)

The Waltz and Basel method is used to examine the content validity index. Experts define each item as "relevant," "clear," and "simple" based on a four-part Likert scale.

Experts rate each item as 1 "not relevant", 2 "relatively relevant", 3 "relevant" and 4 "completely relevant". The simplicity of the item is 1 "not simple", 2 "relatively simple", 3 "simple", to 4 "simple and relevant", respectively, and the clarity of the item from 1 "not clear", 2 "relatively clear", 3 “clear", 4" is clear and relevant".

$$CVI=\frac{\text{Number of experts who gave the item a score of 3 and 4}}{\text{total number of experts}}$$

The minimum acceptable value for the CVI index is 0.79, and if the CVI index is less than 0.79, that item should be removed. In this research, each method has been used for the content validity of the questionnaire. The researcher has involved 15 persons including shipping managers, professors and consultants. For CVR items, the options are "necessary item", "item is useful but not necessary" and "item is not necessary", and for CVI items the options are "not relevant”, “relatively relevant”, “relevant”, "quite relevant", "not simple", "relatively simple", "simple", "simple and relevant", "not clear", "relatively clear", "Clearly", "Clearly and relevant". The minimum CVR for 15 specialists should be at least 0.75. After collecting CVR data, all items with value of more than 0.79 were calculated. The minimum CVI value must be at least 0.49. After collecting CVI data, all items were calculated equal to or greater than 0.79. Therefore, all the statements were considered appropriate by experts and approved.

5.5. Reliability

The reliability or reliability of a measure, shows the stability and logical coordination of the answers in the measurement tool and helps to evaluate the "correctness or appropriateness" of a measure. In other words, the reliability of the questionnaire means whether the measurement tools used in the research will achieve the same results under the same conditions or.

Table 1. Minimum acceptable CVR based on the number of evaluating experts

Number of experts	CVR	Number of experts	CVR	Number of experts	CVR
5	0.99	11	0.59	25	0.37
6	0.99	12	0.56	30	0.33
7	0.99	13	0.54	35	0.31
8	0.75	14	0.51	40	0.29
9	0.78	15	0.49		
10	0.62	20	0.42		

One of the technical features of the measurement tool is reliability. Reliability refers to the extent to which measuring instruments produce the same results under the same conditions. The purpose of the reliability of a measuring instrument is that if we measure the characteristic with the same instrument under similar conditions, how similar, accurate and reliable the results are. A valid instrument has the feature of reproducibility and recreation [12]. There are several methods for measuring the reliability of the questionnaire, which will be used according to the characteristics of the tests, including repeating method, parallel method, halving method and Cronbach's alpha coefficient. In this study, because of the different characteristics, Cronbach's alpha method is used to determine the reliability. This method is used to calculate the internal consistency of measuring instruments such as questionnaires or tests that measure different characteristics. In such tools, the higher the alpha, the greater the validity of the scale. To calculate the Cronbach's alpha coefficient, we must first calculate the variance of the scores of each subset of the questionnaire questions and the total variance. Then, using the following formula, calculate the value of the alpha coefficient

$$r_{\alpha} = \frac{J}{J-1}\left(1-\frac{\sum S_j^2}{S^2}\right)$$

in this formula:
J = number of questionnaire or test subset questions

S_j^2 = Variance under J test

S^2 = The variance of the total test.

The value of the alpha depends on the individual items. To increase the alpha value and thus increase the scale reliability, all unstable items must be removed. For this purpose, it is necessary to check the alpha value by deleting each specific ite. After entering the data into the software and estimating the reliability of the questionnaire, the Cronbach's alpha coefficient for each of the indicators and its total amount are calculated.

6. Research findings

Statistical result of the first hypothesis
Regression test was used to test this hypothesis. Since the significance level (sig) of the test is less than 0.05, the first hypothesis of the research has been confirmed. In other words, the dimensions of public relations affect the problems of seafarers and also the correlation rate is equal to 0.198, which indicates that this level of impact is below average.

Statistical result of the second hypothesis
Regression test was used to test this hypothesis. Since the value of significance level (sig) of the test is less than 0.05, the second hypothesis of the research has been confirmed. In other words, the dimensions of public relations affect the liability to shareholders and also the correlation rate is equal to 0.293, which indicates that this level of impact is below average.

Statistical result of the third hypothesis
Regression test was used to test this hypothesis. Since the value of the significance level (sig) of the test is less than 0.05, the third hypothesis of the research has been confirmed. In other words, the dimensions of public relations have an impact on maritime accident management and also the correlation rate is equal to 0.319, which indicates that this level of impact is below average.

Statistical result of the fourth hypothesis
Regression test was used to test this hypothesis. Since the value of the significance level (sig) of the test is less than 0.05, the fourth hypothesis of the research has been confirmed. In other words, the dimensions of public relations have an impact on maritime accident crisis management and also the correlation rate is equal to 0.401, which indicates that this level of impact is at a moderate level.
Statistical result of the fifth hypothesis

Regression test was used to test this hypothesis. Since the value of the significance level (sig) of the test is less than 0.05, the fifth hypothesis of the research has been confirmed. In other words, the dimensions of public relations have an effect on the protection of interests and also the correlation rate is equal to 0.456, which indicates that this level of impact is at a moderate level.

Statistical result of the sixth hypothesis
Regression test was used to test this hypothesis. Since the value of the significance level (sig) of the test is less than 0.05, the sixth hypothesis of the research has been confirmed. In other words, the dimensions of public relations affect the demand for seafaring and also the correlation rate is equal to 0.327, which indicates that this level of impact is below average.

Statistical result of the seventh hypothesis
Regression test was used to test this hypothesis. Since the value of the significance level (sig) of the test is less than 0.05, the seventh hypothesis of the research has been confirmed. In other words, the dimensions of public relations affect marine culture and also the correlation rate is equal to 0.456, which indicates that this level of impact is at a moderate level.

Statistical result of the eighth hypothesis
Regression test was used to test this hypothesis. Since the value of the significance level (sig) of the test is less than 0.05, the eighth hypothesis of the research has been confirmed. In other words, the dimensions of public relations have an effect on reducing sailors' concerns and also the correlation rate is equal to 0.319, which indicates that this level of impact is below average.

Statistical result of the ninth hypothesis
Regression test was used to test this hypothesis. Since the value of the significance level (sig) of the test is less than 0.05, the ninth hypothesis of the research has been confirmed. In other words, the dimensions of public relations affect the maritime culture and also the correlation rate is equal to 0.548, which indicates that this level of impact is at a moderate level.

Statistical result of the tenth hypothesis
Regression test was used to test this hypothesis. Since the value of the significance level (sig) of the test is less than 0.05, the tenth hypothesis of the research has been confirmed. In other words, the dimensions of public relations have an effect on improving the quality of seafarers' training and also the correlation rate is equal to 0.459, which indicates that this level of impact is at a moderate level.

7. Discussion and Conclusion

Since communication in the organization is a tool to achieve the desired goal, the tasks within the public relations of the organization include understanding and empathy with the employee in ways to gain their trust. The more people are trusted, the better the response will be. One of the tasks of public relations is to communicate effectively. One of the most important tasks of public relations is to build trust, culture, and the most important task of public relations is to influence public opinion in order to gain positive public opinion towards the organization. Communication in public relations includes the pattern of informing, policy-making, gathering and summarizing the views of the people, which can finally be evaluated by monitoring the performance of public relations through various medias. Establishing proper communication with the press, radio, television, and news agencies and using them optimally to "inform" the people is one of the duties of public relations. On the other hand, cultural activities of public relations including participation in holding seminars, gatherings and advertising coverage, and evaluating public opinion is a highly important in public relations. Accordingly, the development of telecommunications and international communication and the emergence of the globalization phenomenon have increased the importance and priority of communication and information processing and has made public relations play a decisive role in the competition, conflict and international solidarity and the development of convergence and understanding among the nations. In this regard, the maritime transport industry is considered one of the largest international industries and at the same time the most critical of them. meanwhile, maritime jobs and related activities are considered as sensitive and difficult jobs. Therefore, the World Maritime Organization, which is the main authority of the maritime transport sector, has considered paying attention to maritime safety issues as one of its most important tasks, and with the formation of the Maritime Safety Committee, which is the senior technical committee of the World Maritime Organization, Deals with maritime safety. over the past decades the committee has enacted laws and regulations and instructions related to safety such as setting standards, qualifications and protection of seafarers, safeguarding the lives of people at sea and marine reconnaissance and rescue, which are implemented by The member states of the World Maritime Organization that have played an effective and undeniable role in improving and strengthening maritime safety. A review of the resolutions of the said organization shows the fact that in all regulations, the human factor is taken into account and since the human factor can affect or be affected by safety, security and the marine environment, maritime safety regulations covers a wide range of human activities, from ship crew activities to port and coast

management. In this study, due to the importance of the research topic, in the first phase, after evaluating the research literature, the qualitative method and interview tools were used to identify the relevant dimensions and then by evaluating the research hypotheses, it was determined that public relations strategies have its own impact and the impact was approved by the results. So what is being argued is that the maritime industry is different from other industries not only in appearance but also in internal dimensions, and this industry, despite the existing efforts to deregulate and move towards globalization, also pursues its own policies. This industry is directly related to natural and environmental resources and lead to the recognition of the sensitivity of the role of public relations, which should accurately present the role of information inside and outside the organization and the educational development role for the personnel. Today, the economic value of the port and maritime industry is measured by safety and environmental protection criteria, and public relations as a key intermediary between the organization and the external environment plays a vital role and can facilitate communicate at organizational, inter-organizational, national and international level.

7.1. Research suggestions

- It is suggested that the role of organizational culture in relation to the performance of port public relations in different cities be evaluated comparatively.
- It is suggested that the type of intra-organizational communication between employees and managers and the different aspects affecting the promotion of this communication be examined with the approach of public relations activities.
- It is suggested that the social resources of the organization be examined in relation to public relations activities.
- It is suggested that knowledge management in public relations be examined qualitatively among employees and managers of public relations in the Ports and maritime Organization offices in different cities.
- It is suggested that the role of social media compared to other forms of media in public relations activities be examined and linked dimensions to public relations activities be identified.
- It is suggested that the degree of employee participation in order to develop the public relations activities of the Ports and maritime Organization be examined form the employees and the managers' points of views comparatively.

8. references

[1] Greenberg, Josh, Knight, Graham, Westersund, Elizabeth, (2011), Spinning climate change: Corporate and NGO public relations strategies inCanada and the United States, Published by sage

[2] Weaver, CK, Motion, J, Roper, J, (2007), An Analysis of the Strengths and Weaknesses of Applying James' Framework for Intentional Positioning in Public Relations, Published by sage.

[3] Davis, (2000), A Theoretical Extension of the Technology Acceptance Model: Four Longitudinal Field Studies, Published by sage.

[4] Haws, Nathan W, (2004), The Effect of Vertically Decreasing Macropore Fractions on Simulations of Non-Equilibrium Solute Transport, vadose zone journal

[5] Habibzadeh, Ashab, (2011), A Study of Factors Affecting Organizational Social Capital with Emphasis on the Role of Public Relations and Presenting an Appropriate Model, Doctoral dissertation, under the guidance of Dr. Ezatollah Sam Aram, Tehran, Faculty of Social Communication Sciences, Allameh Tabatabai University

[6] Cox, S, & Flin, R. (1992). Safety culture: Philosophers stone or man of straw? Work & Stress, Published by sage

[7] Wigman, D. A., & Shappell, S. A. (2003). A human error approach to aviation accident analysis: The human factors analysis and classification system. Burlington,T: Ashgate Publishing Company.

[8] Maurino, D. E., Reason, J., Johnston, N., & Lee, R. B. (1992). Beyond aviation human factors - safety in high technology systems. Aldershot, UK: Avebury Aviation.

[9] Bird, frank, (1974), Management Guide to Loss Control, publisher: Intl Loss Control Inst.

[10] Degani, Asaf, Wiener, EL ,(1994) on the design of flight –Deck Procedures,Nasa Ames research center.

[11] Turner, B. A. (1923). The use of grounded theory for the qualitative analysis of organizational behavior. Journal of Management Studies, 2. (3), 333-348

[12] Sarmad, Zohreh Bazargan, Abbas; Hejazi, Elaheh (2007). Research Methods in Behavioral Sciences. Tehran: Agah.

[13] Danaeifard, Hassan; Meysam Latifi; Asghar Naghipourfar and Asghar Moshbaki (2010), Rewriting the Concept of Staff Discipline with Quranic Approach ", Volume 14, Number 3

[14] Biabangard, Esmaeil, (2005), Research Methods in Psychology and Educational Sciences, Tehran:Doran